Tracing fluid saturation during pegmatite differentiation by studying the fluid inclusion evolution and multiphase cassiterite mineralisation of the Gatumba pegmatite dyke system (NW Rwanda).

Niels HULSBOSCH[a*] and Philippe MUCHEZ[a]

[a]*KU Leuven, Department of Earth and Environmental Sciences, Division of Geology, Celestijnenlaan 200E - box 2410, 3001 Leuven, Belgium.*

**niels.hulsbosch@kuleuven.be*

Highlights

- Multiphase SnO_2 mineralisation reflects increasingly magmatic-hydrothermal conditions
- Saline, NaCl-KCl-rich fluid present during saturation of SnO_2 in wall zone
- Saline, NaCl-LiCl-rich fluid present during saturation of SnO_2 in quartz-phosphate core
- Saline, NaCl-rich fluid formed greisens causing saturation of SnO_2 by fluid-rock reactions
- Disequilibrium mineral growth caused local water-saturated melt conditions

Abstract

Aqueous fluid saturation during the internal evolution of phosphorus- and boron-rich pegmatites in NW Rwanda has been investigated using petrography, fluid inclusion microthermometry, and microanalysis of minerals and fluid inclusions (Raman microspectroscopy and LA-ICP-MS). The Gatumba dyke system (GDS) in Rwanda has been selected for this study because it hosts a

multiphase cassiterite mineralisation, in wall, core and internal replacement zones, suggesting an advancing influence of magmatic-hydrothermal conditions during dyke solidification. As such, multiphase cassiterite precipitation is applied as a tracer for magmatic to hydrothermal crystallisation processes in granitic pegmatites. The GDS consists of a group of six major LCT (lithium-caesium-tantalum) family dykes, which all belong to the most differentiated rare-element pegmatites in the Gatumba-Gitarama field. Petrography identified a well-developed internal anatomy consisting of a border, wall, intermediate and a quartz core zone. In addition, replacement zones developed as cleavelandite after perthitic microcline units in the intermediate zone and as muscovite-quartz pockets in the intermediate and wall zones. The latter replacement zone display muscovitisation reactions with the formation of greisens. Texturally, the greisen pockets replace the secondary cleavelandite units. During internal differentiation, multiphase cassiterite mineralisation formed in 1) large microcline crystals of the wall zone (Cst1), 2) assemblage with quartz, F-poor montebrasite, and carbonate- and boron-enriched Mn-fluorapatite in the core zone (Cst2), and 3) the greisen replacement units in the wall and intermediate zones (Cst3). Fluid inclusion micro-analyses demonstrate that a saline aqueous H_2O-NaCl-KCl-(CO_2,N_2) L1-type fluid (~20 wt.% NaCl and ~3 wt.% KCl) was saturated during onset of crystallisation of the wall and intermediate zones and precipitation of the disseminated, magmatic-hydrothermal Cst1 mineralisation in and around large perthitic K-feldspars. Isochore reconstructions of this L1 fluid indicate crystallisation conditions of 535-560 °C and 5.1-5.6 kbar for the GDS. Extensive microcline fractionation and subsequent replacement reactions of cleavelandite after microcline in the intermediate zone were induced by a Li-enriched and more Na-depleted H_2O-NaCl-LiCl-(CO_2,N_2) L2-type fluid, which was present during consolidation of the core zone and present during precipitation of Cst2 phase mineralisation (6-12 wt.% NaCl,1-10 wt.% LiCl). Late-stage, hydrothermal Cst3 mineralisation in the greisen pockets precipitated from a Cs-enriched H_2O-NaCl-(KCl, CO_2,N_2) L3-type fluid (~15 wt.% NaCl) distinctly after the formation of the cleavelandite replacement units. Subsolidus Cst3 precipitation is dominantly

driven by metasomatic, hydrolytic fluid-rock reactions. Combining textural, microthermometric and fluid compositional data with reported Sn melt-fluid partitioning and solubility data demonstrate that primary cassiterite (i.e. Cst1 and Cst2) in the wall and core zone of the GDS precipitated from the exsolved saline aqueous L1- and L2-fluid present at the interface of the highly-fractionated melt phase. Fast disequilibrium growth of (near)-anhydrous mineral assemblages likely caused the formation of flux-rich and, at least locally, water-saturated melt compositions at the crystallisation front of the large crystals. This study emphasises the importance of local magmatic-hydrothermal conditions and the presence of an immiscible aqueous fluid phase during the internal crystallisation and cassiterite mineralisation of rare-element pegmatites.

Keywords

Pegmatite, fluid inclusions, cassiterite, apatite, montebrasite, differentiation, Raman spectroscopy, LA-ICP-MS, microprobe

1. Introduction

Cassiterite (SnO_2) can saturate in a wide range of pressure, temperature and compositional conditions by a continuum of magmatic to hydrothermal processes (Heinrich, 1990; Linnen et al., 2014). In general, Sn deposits form in peraluminous granites and pegmatites but also in associated veins, breccias and replacement units (Heinrich, 1990). As such, cassiterite precipitation can act as a tracer for magmatic to hydrothermal crystallisation processes in granitic pegmatites. Cassiterite occurs in evolved felsic igneous rocks as a common accessory mineral and as the principal Sn mineral. Sn(II) is the prevalent state in these reduced parental magmas wherein Sn acts as an incompatible element during fractional crystallisation (Lehmann, 1990). In associated hydrothermal fluids, Sn(II)chloride complexes are generally regarded as

important species over a wide range of conditions (Migdisov and Williams-Jones, 2005), although, the stability of Sn(IV)chloride complexes is recently demonstrated (Schmidt, 2018). Magmatic cassiterite is unlikely to saturate at or near liquidus temperatures (Lehmann, 1990; London, 2018; Štemprok, 1990) due to the high solubility of Sn in peraluminous melts (i.e. ~0.3-1.0 wt.%; Bhalla et al., 2005; Linnen et al., 1996) in comparison to the relatively moderate Sn content of ore-bearing, evolved granites and pegmatites (i.e. tens to hundred ppm). Magmatic (super)saturation of cassiterite may only occur in extremely fractionated granitic and pegmatitic subsystems and requires substantial lowering of the crystallisation temperature (Linnen et al., 2014; London, 2018; Štemprok, 1990). These conditions could be achieved in pegmatites 1) via extensive enrichment of incompatible melt structure-modifiers including H_2O, B, P, F and rare alkalis (Li, Rb, and Cs), which all act as fluxes (cf. Fiege et al., 2018; Hulsbosch et al., 2014; London, 2008) and 2) via undercooling by heat flow out of the magmatic system (i.e. liquidus undercooling) together with rapid crystal growth conditions (i.e. disequilibrium crystallisation). The presence, role and timing of fluid exsolution during pegmatite differentiation and cassiterite mineralisation is strongly debated. London (2018) stated on the basis of experimental research that cassiterite crystallises directly from a water-undersaturated peraluminous silicate melt. However, Webster et al. (1997) and Thomas and Webster (2000) conclude on the basis of melt inclusion research in the Ehrenfriedersdorf pegmatite that magmatic cassiterite (Erzgebirge, Germany) saturated from a low density, low viscosity, strongly peraluminous silicate liquid which is coexisting with a fluid phase. The silicate liquid demonstrates extreme enrichment in H_2O, F, Li, Rb, Cs, P_2O_5 and Sn (1000-2000 ppm; up to 7000 ppm).

Hydrothermal Sn deposits, dominantly hosted in quartz veins in and around granites, univocally involve the saturation and exsolution of an aqueous fluid from residual granitic magma and the partitioning of Sn in favour of the mobile fluid phase (Heinrich, 1990). The formation of hydrothermal Sn deposits requires, as such, 1) magmatic Sn enrichment by extensive solidification and differentiation through fractional crystallisation of the parental

granitic magma, 2) Sn fluid-transport, 3) funnelling of these magmatic fluids into structural traps, and 4) precipitation of dissolved Sn by fluid-rock interaction, cooling, boiling or dilution by fluid mixing (Audétat et al., 2000; Heinrich, 1990; 2017; Korges et al., 2018; Schmidt, 2018). Moreover, many granites associated with hydrothermal tin ore systems show extended fractional crystallisation trends with, however, extremely low tin contents (mean Sn concentrations: 2-4 ppm; Lehmann, 1990). This demonstrates the role of subsolidus redissolution and redistribution of tin from these evolved granites by late-stage hydrothermal and meteoric fluids (Lehmann, 1990; and references therein). Cassiterite formation in granite-related, hydrothermal veins is de facto evidence of exsolution of magmatic aqueous fluids and emphasises the importance of the aqueous fluid phase as a petro- and metallogenetic formation medium for these Sn deposits.

Granitic pegmatites are generally regarded as products of igneous differentiation of evolved leucogranites. Pegmatites could, as such, potentially hold a record of the transition from magmatic to hydrothermal conditions (e.g. Siegel et al., 2016) as they can be viewed on a petrological systemic level as intermediates between a magmatic, (leuco)granitic end-member and a hydrothermal quartz vein endmember (Černý et al., 2005; Hulsbosch et al., 2017; Jahns and Burnham, 1969; Varlamoff, 1972). The origin of granitic pegmatites and their distinctive petrological features, including but not limited to giant crystal sizes or typical crystal textures (e.g. unidirectional solidification, graphic or replacement textures), is related to strong liquidus undercooling and fast disequilibrium crystal growth (London, 2014; London and Morgan, 2017; Maneta and Anderson, 2018; Sirbescu et al., 2017). However, controversy still exists 1) whether these exceptional crystallisation kinetics cause the formation of a boundary layer melt at the interface between the fast growing crystals and the viscous surrounding bulk melt (~10^5 to ~10^8 Pa·S) or the formation of melt-melt-fluid immiscibility in combination with a low-viscosity melt (~10^2 Pa·S), and 2) consequently whether exsolved aqueous fluids play a role in the development of pegmatites (Hulsbosch et al., 2019; London, 2014; Maneta and Anderson,

2018; Nabelek et al., 2009; Sirbescu et al., 2017; Veksler et al., 2002). Reviews on pegmatite formation by London (2008, 2014), which are largely based on his extensive experimental program, conclude that the pegmatite-forming silicate melt has to remain water-undersaturated until the end of crystallisation and that an exsolved aqueous fluid is not considered to play an petrogenetic role in the accumulation of incompatible elements, like Sn, and the textural internal evolution. Recently, Maneta and Anderson (2018) demonstrated, conversely, that intrinsic pegmatite features, such as, substantial nucleation delays, low nucleation densities, rapid crystal growth rates and the formation of megacrysts, can also be reproduced experimentally by disequilibrium crystallisation through liquidus undercooling of a low-viscous silicate melt in the presence of a coexisting aqueous phase (cf. Jahns and Burnham, 1969). The presence of exsolved aqueous fluids during pegmatite formation is also often invoked to explain abundant field and experimental observations of non-pseudomorphic replacement textures in pegmatites, such as quartz-muscovite-cassiterite pockets, massive irregular cleavelanditic albite after K-feldspar zones or replacive quartz–K-feldspar intergrowths (Dewaele et al., 2011; Jahns and Burnham, 1969; Kontak, 2006; Maneta and Anderson, 2018; Sirbescu et al., 2017). The origin of these replacement units is, as such, difficult to reconcile with a complete water-undersaturated igneous evolution of pegmatites (e.g. London, 2008).

This study aims to trace the fluid evolution in Sn-Nb-Ta-mineralised, lithium-caesium-tantalum (LCT) family pegmatites of the Gatumba dyke system (GDS, NW Rwanda) and its associated multiphase cassiterite mineralisation as proxies for the role of the magmatic-hydrothermal transition in pegmatite formation. This system consists of six major rare-element pegmatite dykes exhibiting internal mineralogical zonation sequences characteristic for LCT pegmatites (cf. London, 2014). The GDS is specifically selected for this study on the role of aqueous fluids in pegmatite formation because it hosts multiphase cassiterite mineralisation which indicates an increasingly, temporospatial influence in magmatic-hydrothermal conditions: cassiterite in 1) large microcline crystals of the intermediate zone, 2) assemblage with primary

phosphates in the quartz core zone, and 3) quartz-muscovite replacement units in the wall and intermediate zones. Detailed petrography, fluid inclusion microthermometry, and fluid and mineral microanalyses with Laser Ablation Inductively Coupled Plasma Mass Spectrometry (LA-ICP-MS) and Raman microspectroscopy are applied to monitor the internal crystallisation systematics of the GDS and to evaluate the role of aqueous fluid saturation in pegmatite formation.

2. Geological background

The Early-Neoproterozoic GDS pegmatites of NW Rwanda belong to the Mesoproterozoic Karagwe–Ankole belt, which extends from SW Uganda, Rwanda, Burundi and both Kivu provinces of the Democratic Republic of the Congo (Fig. 1A; Tack et al., 2010). The Karagwe-Ankole Belt hosts, together with the associated Kibara Belt, the Early-Neoproterozoic Kibara Metallogenic Province (Hulsbosch, 2019; Pohl et al., 2013). This granite-related ore province consists of the Early- Neoproterozoic “Kibara tin granites” (i.e. so-called G4-generation in Rwanda) with spatiotemporal and genetically related pegmatites and hydrothermal quartz veins (Fig. 1A; Cahen and Ledent, 1979; Hulsbosch, 2019; Hulsbosch et al., 2014). This province of more than 250.000 km^2 constitutes one of the world's largest Ta–Nb–Sn–W regions (Melcher et al., 2015). Sn-Nb-Ta mineralisation is hosted by LCT pegmatites with Sn mineralisation substantially more abundant in greisenised pegmatite units and in peribatholitic, hydrothermal quartz veins (Dewaele et al., 2011).

The GDS pegmatites are part of the boron- and phosphorous-rich Gitarama-Gatumba pegmatite field (>150 km^2) which is a well-developed example of a regionally zoned leucogranite-pegmatite system (Hulsbosch et al., 2014). The Early-Neoproterozoic pegmatites intruded Mesoproterozoic metasediments and metagabbros/dolerites (Dewaele et al., 2011; Hulsbosch et al., 2014; Lehmann et al., 2014). The pegmatites are genetically related to post-compressional leucogranites, which were regionally emplaced at 986 ± 10 Ma (U-Pb SHRIMP

zircon; Tack et al. 2010) and intruded dominantly metasediments and older Mesoproterozoic peraluminous granites (Hulsbosch et al., 2014). The metagabbros/dolerites partly hosting the GDS are interpreted as belonging to a bimodal suite together with the older granite generations (~1375 Ma; Tack et al., 2010). Tantalum-niobium oxide U-Pb ages from the Gitarama-Gatumba pegmatite field show maxima around 990–960 Ma (Melcher et al., 2015). The regional pegmatite zonation comprises four successive zones of increasingly more differentiated LCT pegmatite bodies. The most distal and evolved pegmatite zone hosts mineralisation and belongs to the rare-element class. This zone comprises two subgroups of dykes: 1) zoned Sn-Nb-Ta pegmatites showing moderate albitisation and greisenisation, containing typically large beryl and spodumene crystals and developing distinct quartz cores hosting amblygonite-montebrasite and other primary to secondary phosphates (apatite, triphylite, alluaudite group, purperite-heterosite etc.; e.g. Fransolet and Abraham, 1983) and, 2) heavily to completely albitised and greisenised Sn-Nb-Ta pegmatites containing remnant spodumene and abundant secondary muscovite and being richer mineralised in Sn (Varlamoff, 1972; and references therein). Some dykes of subgroup 1 can locally develop irregular quartz-elbaite-lepidolite cores (e.g. Nyaligamba dyke). Subgroup 1 and 2 dykes have been interpreted as belonging to the same intrusion suite of which subgroup 1 dykes are the more igneous pristine and less metasomatically altered members (Dewaele et al., 2011; Varlamoff, 1972; and references therein). The GDS and the nearby located Buranga dyke (Fig. 1B), i.a. illustrious for its extremely diverse (phosphate) mineralogy (e.g. Fransolet and Abraham, 1983), are members of subgroup 1. The hydrothermal overprint directly related to the pegmatite formation has introduced Li, B, As and Bi into hydrothermally altered country rocks with the formation of e.g. tourmaline–muscovite schists (Lehmann et al., 2014). The large-scale differentiation and development of regional zonation in the Gitarama-Gatumba field has been characterised in terms of continuous fractional crystallisation of the parental ‘Kibara tin” granitic source magma. The GDS pegmatites represent the final stage, residual melts formed by at least 98%

fractionation of the parental granitic magma (Hulsbosch et al., 2014). Historic production (1930s-1985) of the GDS amounted 20,000 t of cassiterite and 4000 t of columbite-tantalite. Currently, the GDS is artisanally mined and open pit reserves of 26 MT at a grade of 153 ppm Sn, 70 ppm Ta and 82 ppm Nb have been reported (Pohl et al., 2013).

3. Methodology

3.1. Field work, sample collection and petrography

Field petrography was performed during campaigns in 2014, 2016, 2017 and 2018 in order to map in detail the GDS internal mineralogical zonation sequence and sample all observed internal zones. An additional decimetre-sized sample with museum code RG 9642 (i.e. sample 1702 in this study) has been selected from the rock collection archived at the Royal Museum for Central Africa (RMCA). The morphological extent of the GDS and exact location of the collection sample were derived from the cartographic archives of the former mining companies Minétain and Somirwa (i.e. Société Minière du Rwanda) stored at the RMCA. Thin sections and polished sections of each internal zone were studied by polarisation microscopy. The composition of feldspars was determined by the Michel Lévy method and Raman spectroscopy.

3.2. Fluid inclusion petrography and microthermometry

Doubly-polished wafers with a thickness of ~350 µm were prepared and studied by optical microscopy to determine fluid inclusion typologies and assemblages. Each fluid inclusion was also documented by microphotographs taken pre- and post-microthermometric analysis in order to evaluate induced leakage, which can be proxied by variations in vapour volumes or fill rates. Only inclusions showing no observable signs of post-entrapment or post-microthermometric modifications were incorporated in the inclusion dataset. Microthermometry was conducted on a Linkam MDS600 heating and freezing stage mounted on an Olympus BX51 microscope.

Accuracy of the measurements is within ±0.2 °C for temperatures measured between -74.8 °C and +31.1 °C and within ±1 °C for temperatures above +31.1 °C. Calibration was done using synthetic fluid inclusions (Syn Flinc, USA) of the systems H_2O–CO_2, H_2O–NaCl, H_2O–KCl and H_2O. In addition, the melting point of indium (156.6 °C) was applied as a standard at higher temperature. The samples were first cooled to avoid stretching, leakage and decrepitation of the fluid inclusions due to enhanced internal pressures. Reported phase transition temperatures (T_{fm}, $T_{m,ice}$, $T_{m,hh}$, $T_{m,CO2}$, $T_{m,clath}$, $T_{h,CO2}$ and $T_{h,tot}$) were determined by slow-rate cooling to -190°C and applying upon heating a cyclic heating-cooling method. Both methods were applied to obtain precise measurements (especially for $T_{m,ice}$ and $T_{m,hh}$) and to avoid metastability and incomplete liquid solidification effects (cf. CO_2 or Li-containing fluid inclusions; Diamond, 2001; Dubois et al., 2010). Phase transition temperatures were measured with a heating rate of 0.5 °C min^{-1} except for total homogenisation temperatures. The latter phase transition was determined by stepwise heating at 25 °C min^{-1} for the interval room temperature to 200°C and at 10 °C min^{-1} for the interval 200°C to total homogenisation temperature. Important to note is that when the inclusions were initially only cooled to approximately -110°C, no first melting around -70°C could be observed but only a sudden change in the appearance of the aqueous phase around −35°C. The latter transition could erroneously be identified as first melting.

Salinity of the aqueous phase in fluid inclusions was estimated from microthermometric data. Fluid inclusions showing first melting temperatures around -26 °C and up to -31°C (i.e. L1 and L3a fluids; see section 4.3) are classified as containing NaCl and KCl as dominant components; first melting temperatures around -22 °C indicate a dominant NaCl composition with the important presence of other monovalent cations such as K (i.e. L3b fluids; see section 4.3). The lowering of the observed first melting temperature, for the L1 and L3a fluids, compared to the theoretical eutectic temperature of the H_2O-NaCl-KCl system (-23.5 °C) is interpreted to be attributed to the presence of alkali (earth) metals in the aqueous fluid phase. Inclusions showing very low first melting temperatures (−79°C to −56°C; mode 69°C) (i.e. L2 fluids; see

section 4.3) are classified as containing NaCl and LiCl as dominant components (Dubois et al., 2010). In case of aqueous inclusions of the H_2O-NaCl-KCl system, NaCl wt.% and KCl wt.% concentrations were calculated based on hydrohalite and ice melting temperatures applying the model of Bodnar et al. (1989). For aqueous-gaseous fluid inclusions of the H_2O-NaCl-LiCl-CO_2-N_2 system (i.e. L2 fluids; see section 4.3), firstly the bulk salinity and the Na/Li ratio of the fluid was estimated from the hydrohalite and ice melting temperatures by applying the model of Dubois et al. (2010) for the H_2O-NaCl-LiCl system. However, the inclusions (i.e. L2b; see section 4.3) can show the presence of two carbonic phases (i.e. liquid and vapour CO_2 containing some N_2) and the formation of clathrates (i.e. observable $T_{m,CO2}$, $T_{m,clath}$ and $T_{h,CO2}$). The overestimation of the salinity of the residual aqueous liquid due to the presence of clathrate (Q2 behaviour; Diamond, 2001) was corrected by a three-step approach. Salinities of these Li-rich, aqueous-gaseous inclusions were calculated by 1) converting the obtained bulk salinity in the H_2O-NaCl-LiCl system to a $NaCl_{eq}$ Wt.% content, 2) modelling the $NaCl_{eq}$ wt.% content based on the $T_{m,clath}$ with the Q2 program of Bakker (1997) which takes into account the effect of clathrate melting in the presence of and aqueous solution and two carbonic phases containing N_2, and 3) recalculating the salinity in the H_2O-NaCl-LiCl-CO_2-N_2 system by quantifying the overestimation of the salinity due to the presence of clathrate from steps 1 and 2 and by knowing the Na/Li ratio of the fluid in the H_2O-NaCl-LiCl system. Salinities of the aqueous-gaseous fluids (i.e. L3a fluids; see section 4.3) belonging to the H_2O-NaCl-KCl-CO_2-(N_2) system were similarly modelled but the bulk salinity and the Na/K ratio of the aqueous fluid was derived from the hydrohalite and ice melting temperatures and calculated with the model of Bodnar et al. (1989). Salinities of dominantly aqueous fluid inclusions in the system H_2O-NaCl-(CO_2,N_2) (i.e. L3b fluids; see section 4.3) were also calculated with the Bodnar et al. (1989) program. Isochores of the L1b fluid system have been calculated using the BULK and ISOC programs of the computer package FLUIDS (Bakker, 2003) applying the equation of state of Anderko and Pitzer (1993).

3.3. Raman spectroscopy

Raman scattering of minerals was measured with a Bruker Senterra dispersive laser Raman spectrometer mounted on an Olympus BX50 microscope at the Royal Belgian Institute of Natural Sciences (Brussels, Belgium). The samples were excited by a green Nd:YAG laser (532 nm, 20 mW rated power at the exit of the laser box) or by a red diode laser (785 nm, 100 mW) in case of signs of fluorescence or laser photosensitivity. An Olympus long working distance, confocal objective with 100x magnification (0.9 NA) was used in combination with a confocal pinhole of 25 µm. Raman spectra were acquired in 1–3 cm^{-1} resolution mode using the high-precision diffractor. Each spectrum results from the accumulation of five to seven acquisitions of 20–35 s each. All spectra were collected with a 1024 × 512 pixel, Peltier-cooled CCD detector operating at -65 °C. The positions of the Raman bands were calibrated by using a laser neon spectra. Spectra treatment was performed with the Horiba LabSpec5 and SYSTAT Inc. PeakFit V4.12 software and consisted of linear baseline correction, spike elimination, and Gauss-Lorentzian peak searching/fitting. Minerals, occurring as rock-forming phases or which can be sometimes present within the fluid inclusions, were identified by comparison of their spectral fingerprints with reference spectra using the RRUFF project CrystalSleuth software. The quantitative analysis of the relative molar composition of the vapour phase within fluid inclusions was determined using a response function calibration of the Raman intensity with NIST SRM 2241.

3.4. LA-ICP-MS analysis

Individual fluid inclusions and their specific host minerals (i.e. cassiterite and amblygonite-montebrasite) were ablated with an ESI New Wave Research UC 193 nm excimer laser at 5 Hz laser frequency, with an energy density of 3 J cm^{-2} and a pulse duration of less than 4 ns. The laser system contains a 100mm x 100mm ablation cell which results in <700 ms wash-out times

by the incorporation of a smaller roving cup with an internal volume <1 cm^3. The aerosols were analysed with an Agilent 8900 Triple Quadrupole ICP-MS, equipped with a collision–reaction cell at the GeoRessources Laboratory (Nancy, France). In order to reduce elemental fractionation, the ablated material was carried in helium gas (0.5 l min^{-1}) which was mixed with argon (0.9 l min^{-1}) via a cyclone mixer (volume of 9.5 cm^3) prior to entering the ICP torch. A straight ablation technique with spot sizes of 30 and 40 µm was applied to obtain overall higher signal-to-background intensity ratios and lower limits of detection (LOD). The ablation quality was visually evaluated during laser drilling. Only analyses demonstrating controlled openings without spallation were incorporated in the final dataset. Each analytical series was limited to 15 isotopes (^{7}Li, ^{23}Na, ^{24}Mg, ^{31}P, ^{39}K, ^{55}Mn, ^{57}Fe, ^{85}Rb, ^{88}Sr, ^{93}Nb, ^{118}Sn, ^{133}Cs, ^{137}Ba, ^{181}Ta and ^{182}W) in order to optimise LOD and precision. Counting time per sweep did not exceed 350 ms and dwell times of 50 ms for Sn, 30 ms for Li, P, Nb, Ta and W, 20 ms for Rb, Sr, Cs, and Ba and 10 ms for Na, Mg, K, Mn and Fe were selected to enhance the number of counts. Obtained intensity ratios to Na were converted to concentration ratios by external calibration against a NIST 610 standard reference glass following a bracketing standardisation procedure. In addition, NIST 612 glass was used as a control standard. All spectra have been processed using the SILLS software package of Guillong et al. (2008). For the fluid inclusion analyses, ^{23}Na was used as internal standard to calculate absolute concentrations and was obtained via microthermometry. The charge-balanced method of Allan et al. (2005) has been applied in further data reduction steps. Limits of detection for a given element have been calculated according to Longerich et al. (1996). The spectra of fluid inclusions hosted in cassiterite and montebrasite-amblygonite have been matrix-corrected based on the stoichiometric Sn or Li content of the host, respectively, and ^{7}Li or ^{39}K as second internal standard obtained via microthermometry (depending on the fluid type, see section 4.3).

For the host analyses, the elemental concentrations were calculated using ^{7}Li (montebrasite-amblygonite) or ^{118}Sn (cassiterite) as internal standard. The concentration of the

host samples was calculated from the known mineral stoichiometry (cf. Longerich et al., 1996). Specifically for cassiterite, only light coloured, optically transparent zones have been analysed by LA-ICP-MS as these zones host observable fluid inclusions.

3.5. FEG-EPMA analysis

The major element composition of montebrasite, blue apatite and cassiterite was analysed using a JEOL JXA-8530F field emission electron probe micro-analyser (FEG-EPMA), equipped with five wavelength dispersive spectrometers (WDS) at the Department of Material Engineering (MTM), KU Leuven.

Montebrasite measurements (Na, K, Ca, P, F, Cl, Si and Al) were performed under 10 kV accelerating voltage, 10 nA beam current and 10 µm beam diameter. Fluorine, Cl, Na and P were measured for 15 s in peak position, while Si, Al, K and Ca were measured during 20 s. Background signal was measured at upper and lower positions during 5 s each. Apatite measurements (Na, K, Ca, B, N, F, Cl, Mg, Al, Si, P, Fe and Mn) were performed with 10 kV accelerating voltage, 5 nA beam current and 10 µm beam diameter. The peak position of each element was measured during 30 s, the upper and lower background positions each during 5 s. The quantification of carbon, substituted as carbonate, in apatite by microprobe was not possible due to carbon coating of samples and standards. Cassiterite measurements (Sn, Mg, Al, Ti, Si, Fe, Cr, Mn, Nb, Ta and W) were performed with 25 kV accelerating voltage, 40 nA beam current and 1 µm beam diameter. The peak position of each element was measured during 20 s, except for Nb, Ta and W, which peak position was measured for 40 s. Upper and lower background positions were each measured during 10 s. Specifically for cassiterite, both light coloured, optically transparent zones as well as dark coloured, optically opaque zones have been analysed by FEG-EPMA.

The standards albite (Na), boron nitride (B, N), tugtupite (Cl), apatite (Ca, P, F), almandine (Al, Si, Mg, Fe, Mn), orthoclase (K), cassiterite (Sn), rutile (Ti), magnetite (Fe in

cassiterite), crocoite (Cr), Nb metal and Ta metal were used for the calibration. The ZAF correction method was applied for matrix effects. Elements, which are for all analyses per mineral species below detection limits, are not reported.

4. Results

4.1 Anatomy of the GDS

Field observations in combination with a macro- and microscopic study and Raman spectroscopic analyses of 64 specimens enabled characterisation of the morphology and internal anatomy of the GDS. The GDS consists of six major dykes and numerous smaller offshoot dyklets. The outcrop of dyke 6 in the Serege valley (Figs. 1B & 2A) has been selected as a representative cross-section through the GDS on the basis of archived mining data of Somirwa. Currently, this outcrop zone is artisanally mined by ground sluicing and provides good exposures of the internal anatomy of the GDS.

The GDS dominantly intruded metagabbros/dolerites (Figs. 2A & B). These mafic country rocks formed as bedding-parallel sills in muscovite-garnet-andalusite-chlorite-(biotite) phyllites to schists and minor quartzites (bedding S0 260/50). The pegmatite dykes emplaced along axial planar cleavage planes (S1) which are parallel to bedding in the metasediments (S1 260/50) but can develop at lower angles in the mafic sills (S1 270/30). The maximum length of the GDS is approximately 2600 m and individual dyke thicknesses range between ~5-40 m in the metadolerites and between ~3-10m in the metasediments (Somirwa unpublished data). Small pegmatitic stringers (m- to dm-wide) occur along the cleavage planes in the metasediments.

Internally, the GDS dykes consist of five zones: border, wall, intermediate, quartz core and replacement zones. An overview of the dyke internal anatomy is provided in Figure 3. Contact metasomatism by pegmatite emplacement caused a profuse tourmaline-(muscovite) aureole (Fig. 2J) in the country rocks, which can be tracked for up to several hundreds of meters away from

384 the intrusion. Locally, dm-scale irregular holmquistite-bearing assemblages and cm-scale dark-
385 green apatite rims developed in the metagabbros at the contact with the GDS intrusions.
386
387 *4.1.1 Border and wall zone*
388 The border zone of the GDS developed as a sharp 0.5-10 cm thin layer and consists of a very
389 fine-grained quartz and sacharoidal albite matrix with blue-green apatite, minor pinkish microcline
390 and inwardly flaring black tourmaline crystals (Figs. 2B-D). The wall zone ranges in thickness up
391 to 1.5 m. It can develop an aplitic banding (~1 cm thick bands) which consists of medium-grained
392 hypidiomorphic quartz, medium-grained albite, fine-grained, blue-green apatite and muscovite
393 (Figs. 2C). The aplite fabric (max 30 cm thick) evolves dyke-inwards to a more coarse-grained
394 (cm to dm) anisotropic fabric of hypidiomorphic granular quartz, pinkish microcline, green-yellow
395 micas and white plagioclase forming rare spherical radial masses. More internally in the wall zone,
396 inwardly elongate and flaring crystals of quartz, yellowish Li-micas, pinkish perthitic microcline,
397 apatite and fine-grained albite developed. The latter albite-rich fabric contains mm-scale tantalite-
398 columbite crystals. More dyke inward, the wall zone shows larger crystals of primarily pinkish
399 perthitic microcline. Primary crystals of cassiterite are accessory phases in quartz-microcline units
400 of the wall zone and are generally very small (<mm). Larger crystals (up to 2.5 cm) are rare.
401 Macroscopically, this cassiterite phase occurs as sub- to euhedral crystals which are intergrown
402 with quartz, pink perthitic microcline, plagioclase and minor white mica (Fig. 2D). On the
403 microscopic level, the contacts between disseminated cassiterite and quartz, albite-oligoclase or
404 mica are generally defined by crystal faces, however, locally cassiterite seems to have been
405 resorbed, and is embayed or enclosed by feldspar, quartz or mica (Fig. 2E). Cassiterite also
406 developed distinct colour banding and zones with fluid inclusions occuring along these growth
407 zones (see also Fig. 8C).
408
409

410 *4.1.2 Intermediate zone and replacive units*

411 The intermediate zone demonstrates increased crystal sizes (m-scale) and has thicknesses
412 varying from ~3 to ~10 m. This zone is dominated by asymmetrical and dominantly discontinuous
413 bi- to tri-mineral assemblages consisting of perthitic microcline-quartz and Li-muscovite–
414 spodumene–quartz (Figs. 2F & G). Both quartz and spodumene form as dm- to m-long elongated,
415 euhedral crystals demonstrating unidirectional solidification textures (UST) (Figs. 2F & G).
416 Primary, accessory phases consist of white beryl, zircon, green elbaite, apatite, amblygonite-
417 montebrasite and niobium-tantalum oxides. Disseminated niobium-tantalum oxides (cm- to mm-
418 scale) are dominantly associated with the intermediate zone (Fig. 2H). In addition, this zone is
419 partly to near-completely affected by replacement of cleavelandite after microcline (up to 70 vol.%;
420 Figs. 2F-H) and the subsequent development of isolated quartz-muscovite-cassiterite greisen
421 pockets (0.5-5 dm wide; cf. Figs. 2J & K). The greisens replace the primary fabric of the
422 intermediate zone as well as the cleavelandite replacement zones. Both replacement zones, i.e.
423 cleavelandite after microcline zones and greisen pocket zones, can extend towards the wall zone
424 (Fig. 2J). Cassiterite in the greisen pockets occurs macroscopically as eu- to subhedral crystals
425 together with the quartz and muscovite (Fig. 2K). Microscopically, this cassiterite phase forms
426 prismatic colour zonations with the presence of many Nb-Ta-oxide minerals and fluid inclusions
427 along these growth bands (see Figs. 5B, 8K). Spodumene units in the intermediate zone can at
428 its rims and along cleavages be heavily altered to fine-grained intergrowths of secondary
429 muscovite and orange-brown eucryptite, which are embedded in cleavelanditic albite (cf. Fig. 2F).
430 The transition from wall zone to core zone is rather gradual and the border between both zones
431 is broad, irregular and dominantly composed of cleavelandite, green-blue apatite and uncommon
432 whitish apatite. Rarely, euhedral prismatic grains of cassiterite can be observed in this transition
433 zone (Fig. 2I).

434

435

436 *4.1.3 Core zone*

437 The core zone can develop as a coarse monomineralic quartz unit in thinner dyke parts. However,
438 it often formed as a cogenetic assemblage of mutually overgrowing amblygonite-montebrasite
439 and blue apatite with minor dark-blue varulite, coarse quartz, euhedral prismatic cassiterite and
440 accessory intercrystal albite (Fig. 2I). Cassiterite is on a macroscopic level preferentially
441 associated with quartz (red arrows in Fig. 2I). On a microscopic level, the cassiterite crystals show
442 a uniform, red-brown colour without the presence of distinct growth bands but with the presence
443 of a heterogeneous distribution of optically transparent and opaque crystal zones. The core zone
444 comprises a fracture mesh with the development of globular crystal textures of quartz and
445 phosphates. Alteration reactions are observed as blue apatite reacting to dark coloured heterosite
446 and rockbridgeite, amblygonite-montebrasite rimmed by blue apatite to kaolinite, and albite to
447 pyrophyllite (Fig. 2I).

448

449 *4.1.4 Classification and mineralisation*

450 In summary, the GDS can be classified as an LCT-family, rare-element class pegmatite based on
451 the mineralogical classification of Černý and Ercit (2005). The primary mineralogy indicates a
452 complex type, spodumene to amblygonite subtype pegmatite, while the cleavelandite
453 replacements subdivide the GDS as an albite-spodumene to spodumene type pegmatite. Three
454 stages of cassiterite saturation can be petrographically defined in the GDS (Figs. 2D, I and K). In
455 the first stage, cassiterite occurs as a rare, primary and dissiminated, sub- to euhedral phase in
456 magmatic-stage microcline-quartz units of the wall zone (i.e. Cst1). In a second stage, cassiterite
457 occurs more dyke-inward as primary, sub- to euhedral phases in an assemblage with coarse
458 quartz, primary phosphates and minor albite in the core zone (i.e. Cst2). Rarely, this second stage
459 extends to the cleavelandite-rich border between the core zone and intermediate zone. In the
460 third stage, secondary cassiterite occurs abundantly in replacive-metasomatic greisen pockets
461 together with quartz and muscovite (i.e. Cst3).

4.2 Mineral analysis

Raman analyses, supported with FEG-EPMA and LA-ICP-MS analyses, were performed to 1) determine the compositional variation in the exotic mineral assemblage of the core zone and 2) evaluate if the three cassiterite phases can be spectroscopically distinguished. Amblygonite-montebrasite, blue apatite, white apatite and the three generations of cassiterite were examined (Figs. 4-6; Appendix A).

4.2.1 Montebrasite-amblygonite

The position and width of some Raman bands of amblygonite-montebrasite (n=14) are related to its fluorine content and enable as such characterisation (Rondeau et al., 2006). Montebrasite-amblygonite in the core zone shows bands at 601.5±0.5 cm^{-1} (PO_4^{3-} bending and AlO_6^{9-} stretching vibrations), at 1058.5±0.5 cm^{-1} (PO_4^{3-}stretching vibration) and at 3369.9±0.7 cm^{-1} (OH^- stretching vibration). The latter band with a full width at half maximum (FWHM) of 33.3±1.4 cm^{-1} (Figs. 4A & B). These observations indicate a dominant montebrasite composition with fluorine contents below 4.5 wt.% (Rondeau et al., 2006). Especially, the FWMH of the OH^- stretching vibration around 3360 cm^{-1} is an accurate proxy for the fluorine content and correlates to 2.3±0.7 wt.% fluorine or 82±5 % montebrasite by applying the calibration of Rondeau et al. (2006). These spectroscopically-derived fluorine contents are within error in agreement with the concentration range of 2.63±0.18 wt.% (i.e. 79±1 % montebrasite; n = 10) as determined by FEG-EPMA (see Appendix A). Based on the calibrated F-OH exchange reaction between montebrasite and pegmatitic melt of London et al. (2001), these montebrasite fluorine contents relate to a generally low, i.e. <0.5 wt.%, fluorine content in the melt system during montebrasite saturation in the core.

488 4.*2.2 Apatite*

489 The Raman spectra of blue apatite (n=17) in the core zone show PO_4^{3-} vibrations at 965 cm^{-1}
490 (v_1), 446 cm^{-1} (v_2), 1060 cm^{-1} (v_3) and 581 cm^{-1} (v_4) and white apatite (n=5) in the transition zone
491 between the core zone and intermediate zone shows modes at 965-966 cm^{-1}, 432 cm^{-1}, 1057
492 cm^{-1}, 582-592 cm^{-1} (Fig. 4C). These peak positions are characteristic for fluorapatite. FEG-
493 EPMA analysis confirmed a dominant fluorapatite composition with 2.83±0.12 wt.% F (n=10),
494 0.02±0.01 wt.% Cl and 0.40 ±0.06 wt.% H_2O, corresponding to a 77±2% fluorapatite with 23±2%
495 hydroxylapatite solid solution (Appendix A; Fig. 4C & 6A). In general, halogen-site variability in
496 apatite from granitic pegmatites is low with predominant fluorapatite compositions due to the
497 similarity in radius for F^- and OH^- as compared to Cl^- (Fig. 6A; Picccoli and Candela, 2002).
498 White apatite develops strong and broad fluorescence signals in the region 1200-2400 cm^{-1}
499 which hamper further spectra description beyond 1200 cm^{-1}. The Raman spectra of blue apatite
500 in the core zone are substantially complicated by the presence of sets of (very) strong vibrations
501 at 1222 and 1258 cm^{-1} (>$v_{1,PO4}$), 1322 cm^{-1}, 1422 cm^{-1} (>$v_{1,PO4}$), and a set at 1510 cm^{-1}, 1582 cm^{-1}
502 and 1710 cm^{-1} (Fig. 4C). The presence of ~1420 cm^{-1} vibrations in fluorapatite is linked to
503 carbonate substitution for phosphate (i.e. $v_{3a,CO3}$ mode of $V_{3,CO3}$ doublet) and requires a paired
504 substitution or vacancies to maintain charge balance (Tacker, 2008). The paired ~1500 cm^{-1}
505 and ~1580 cm^{-1} peaks are bands assigned to carbonate substituting for fluorine, partially charge
506 balanced by carbonate substituting phosphate (i.e. $v_{3b,CO3}$ mode of $V_{3,CO3}$ doublet) (Tacker,
507 2008). Moreover, the total oxide sum of the FEG-EPMA analysis of blue apatite averages
508 98.70±1.29 wt.% although a near-total analysis except for carbon is performed (i.e. Ca, Mn, B,
509 P, F and Cl with Na, K, Mg, Fe, Al, Si and N below detection limits). Microprobe analysis of C is
510 particularly difficult because 1) the X-ray emission of carbon is low, 2) the absorption of carbon
511 K α radiation is high in different matrices, and 3) carbon surface contamination (e.g. organic
512 greases and oil vapours of vacuum pumps) and 4) carbon coating of samples and standards.
513 Igneous carbonate-fluorapatite can contain CO_2 contents ranging from ~0.5 to 3.4 wt.% (Tacker,

2008; Anthony et al. 2000) and can explain the less-than-100% total oxide sum. In addition, these blue apatite crystals have biaxial negative optical properties with a 2V angle of around 20° and a maximum birefringence of 0.006, which are all characteristic for carbonated apatite. The spectroscopic, compositional and optical properties of the fluorapatite crystals strongly point towards a substantial substitution of phosphate by carbonate groups at weight percent level.

The strong peaks at 1222 cm^{-1}, 1258 cm^{-1} and ~1700 cm^{-1} in blue apatite cannot be assigned to carbonate substitutions and indicate the presence of an additional oxyanionic group. Sulphate in apatite is generally not assigned to these positions. Based on FEG-EPMA data, blue apatite contains 1.90±0.58 wt.% MnO and 0.17±0.28 wt.% B_2O_3, which can substitute for PO_4^{3-} as MnO_4^{3-} or as BO_4^{5-} and BO_3^{3-}, respectively. Both groups can contribute to the presence of these peaks and especially in synthetic boron-doped apatite, these additional bands were attributed to borate group vibrations (Ternane et al., 2002). Moreover, the blue colour of apatite is characteristic for manganese enrichment with dominantly Mn^{2+} substituting for Ca^{2+}. The colour, however, originates from MnO_4^{3+} substituting for PO_4^{3+} (Hughes et al., 2004). In conclusion, spectroscopic and compositional analyses characterise blue apatite in the core zone as carbonated Mn-fluorapatite with a significant boron enrichment.

4.2.3 Cassiterite

Raman spectra of the three cassiterite phases (cf. Cst1, Cst2 and Cst3; n=29) all show the characteristic A_{1G} band at 633 to 634 cm^{-1} and a substantially less-intense and broad B_{2G} band around 730 cm^{-1} (Fig. 5) which corresponds to the symmetric and asymmetric stretching of the Sn–O bonds, respectively (Wang et al., 1993). In addition, Cst1 and Cst2 phases contain a characteristic sharp, strong band group at 445-447 cm^{-1} and 474-479 cm^{-1}, and a medium-intense band at ~834 cm^{-1} (Fig. 5A). Cst3 shows substantial spectroscopic variations and can contain strong bands at ~777 cm^{-1}, ~804 cm^{-1} (i.e. infrequent), ~833 cm^{-1} and ~876 cm^{-1} (Fig. 5B). These additional bands (e.g. A_N) are associated with substitutions (Wille et al., 2018). More

specifically, the rarely observed ~804 cm^{-1} and abundantly-observed ~830 cm^{-1} bands are assigned to broad A_n peaks caused by heterovalent substitution of W^{5+} and Nb^{5+}+Ta^{5+}, respectively (Wang et al.,1993). In addition, Ti can substitute isomorphically in cassiterite but spectroscopic identification is not straightforward. However, the intensity of the B_{2G} band is low compared to the A_N band when Nb and Ta contents are low and Ti is high (Wille et al., 2018; Fig. 5). The ~876 cm^{-1} bands are assigned to the A_g peak of microscopic columbite-(Mn) inclusions. Moreover, Cst3 shows abundant 100-450 µm large columbite-(Mn) lamellae along its growth zones with A_g peaks around 870 cm^{-1} (Fig. 5B).

FEG-EPMA analyses have been performed on optically transparent, light coloured and optically opaque, dark coloured zones within all three cassiterite generations (e.g. Fig. 8C). Backscattered-electron imaging, however, did reveal this colour zonation. FEG-EPMA measurements are plotted in Ti-(Fe,Mn)-(Nb,Ta) and W-(Fe,Mn)-(Nb,Ta) coupled substitution ternary diagrams (Figs. 6B & 6C.; Appendix A), which support and specify the substitutions mechanism as observed by Raman spectroscopy (Fig. 5). More specifically, dark coloured zones are generally, and independently of the generation, demonstrating lower SnO_2 contents of 97.02±1.31 wt.%, higher $(Nb,Ta)_2O_5$ contents of 1.86±0.94 wt.% and are characterised by $Fe^{2+}(Nb,Ta)_2{}^{5+}$ substitution mechanisms. On the other hand, light coloured zones have higher SnO_2 contents of 99.30±0.54 wt.%, lower $(Nb,Ta)_2O_5$ contents of 0.94±0.12 wt.% and show Ti^{4+}, W^{4+} and $Fe^{2+}W^{6+}$ substitution mechanism. Consequently, the observed spectroscopic and compositional variations in cassiterite is not directly related to different generations but to micro-textures and zoning within the crystal. The only significant compositional difference between the three cassiterite generations is that Cst3 in the greisens is more enriched in Nb and Ta and shows minor Ti and W substitutions compared to Cst1 and Cst2.

4.3 Fluid inclusion microthermometry

Detailed inclusion petrography and microthermometric measurements were performed on 231 inclusions in quartz, montebrasite and cassiterite from 24 wafer sections representing all internal mineralogical zones and phases. Only the thin border zone and the completely altered cleavelandite replacement zone could not be studied for inclusions due to the fine-grained and translucent nature of the host minerals. On the basis of petrography, six (sub-)types of fluid inclusions could be identified (L1a - L1b, L2a - L2b, and L3a - L3b) for which all typological and microthermometric parameters are provided in Figure 7, Table 1 and in Appendix B.

4.3.1 Type L1 fluids

Type L1 are aqueous inclusions and occur in quartz and Cst1 of the wall zone and intermediate zone (7A-E). Primary inclusions occur in growth zones in euhedral prismatic quartz-microcline units (Fig. 2G) while pseudosecondary inclusions in quartz occur as intragranular and interphase assemblages spatially related to partial microcline replacements in the cleavelandite replacement zone. Two subtypes L1a and L1b are defined. Both L1a and L1b subtypes are microthermometric similar (see below) except for 1) the presence of (Ca^{2+},Mn^{2+},Fe^{2+})-carbonates and paragonite as accidentally trapped solids in the L1a subtype inclusions (Fig. 8A), which is the predominant type in the wall zone while L1b subtype inclusions are more abundant in the intermediate zone, 2) the $T_{h,tot}$ which averages 265°C for L1a and 355°C for L1b and 3) the exclusive occurrence of L1b inclusions in Cst1 (Fig. 8C & D). The microthermometric parameters of both subtypes are shown in Figure 7. They are characterised by a T_{fm} of -26 °C on average and can form clathrate directly from the vapour phase on cooling. The vapour phase is composed of 87 mol% CO_2 and 13 mol% N_2. These observations demonstrate a H_2O-NaCl-KCl-(CO_2, N_2) composition. The last solids that melt on heating can be hydrohalite or ice with melting temperatures ranging from -22.9 °C to -2.3 °C and from -22.9 °C to -13.8 °C,

respectively (Fig. 8B). Calculated salinities are ~20 wt.% NaCl and ~3 wt.% KCl. The fluid chloride molality of L1a fluids is 4.2 ± 0.4 (1σ) mol kg^{-1} and of L1b fluids 4.0 ± 0.4 mol kg^{-1}.

Isochores were calculated for the L1b fluids with an H_2O-NaCl-KCl composition in quartz (n=31) in order to constrain the intrusion temperature and pressure of the GDS (Fig. 9). Isochores were only constructed for these L1b fluids because they are primary inclusions representing a pristine fluid composition (i.e. they do not contain accidentally trapped daughter minerals, cf. L1a). In addition, these L1b inclusions are already present at the onset of dyke solidification at the wall zone and their relatively simple composition permits accurate representation by an equation of state equation (cf. Anderko and Pitzer, 1993). Correlation of the isochores with solidi of volatile-rich (H_2O, Li, B, P) leucogranitic melts (Pichavant, 1984; Pichavant et al., 1987) and regional metamorphic temperatures of the country rocks near the GDS based on garnet-biotite geothermometry of biotite-garnet-muscovite-chlorite metapelites (534±6°C to 543±2°; n=9; Van Daele et al., 2018) enables estimation of the temperature and pressure conditions of crystallisation of the GDS between 535-560 °C and 5.1-5.6 kbar.

4.3.2 Type L2 fluids

Type L2 inclusions can be aqueous (L2a) or aqueous-carbonic (L2b) and occur in primary assemblages in the core zone minerals (Figs. 8F-I). Their microthermometric parameters are shown in Figure 7. All inclusions show very low first melting temperatures (<-60 °C and typically <-68°C) indicating LiCl enrichment (Dubois et al., 2010). Occasionally, L2 inclusions show accidentally trapped Li-mica crystals (Fig. 8F). Ice is always the final solid which melts in the aqueous phase on heating with an average melting temperature of -17.7 °C. Hydrohalite melts on average at -31.9 °C (L2a) and at -22.2 °C (L2b). L2a subtype inclusions occur in montebrasite and Cst2 (Fig. 8F & G) and demonstrate an H_2O-NaCl-LiCl composition with ~6 wt.% NaCl and ~10 wt.% LiCl, and a $T_{h,tot}$ of ~300°C. L2b subtype inclusions occur in quartz (Fig. 8H & I) and show distinct melting of the carbonic phase at ~57.6 °C demonstrating an H_2O-

NaCl-LiCl-CO_2-N_2 composition with ~93 mol CO_2 and 7 mol% N_2 in the vapour phase (Table 1; Appendix B). The aqueous solution has a salinity of ~12 wt.% NaCl and ~1 wt.% LiCl. The fluid chloride molality of L2a fluids is 3.0 ± 0.3 (1σ) mol kg^{-1} and of L2b fluids 2.2 ± 0.5 mol kg^{-1}.Total homogenisation of L2b inclusions is around 290°C. Although, L2a and L2b subtype inclusions occur in the core with cogenetic montebrasite, blue apatite, quartz and cassiterite assemblage, the fluid composition shows a complementary evolution from montebrasite-Cst2 (L2a subtype) to quartz (L2b subtype).

4.3.3 Type L3 fluids

Type L3 inclusions are aqueous-carbonic and hosted as intergranular trails and large three-dimensional assemblages by quartz and Cst3 in the greisen replacement zone (Figs. 8J-L). Two subtypes can be defined based on the occurrence of liquid carbonic phase during cooling (L3a) or not (L3b).Their microthermometric parameters are shown in Figure 7. L3 inclusions contain dominantly Na as cation based on the first melting temperatures (Table 1). Melting of hydrohalite was not observed or occurred at the eutectic. Ice is always the final solid which melts on heating with an average melting temperature of -17.7 °C (L3a) and -10.3 °C (L3b). The vapour phase has a composition of 82-89 mol CO_2 and 18-11 mol% N_2 at room temperature. L3a subtype inclusions are hosted in quartz (Fig. 8J) and show an H_2O-NaCl-(KCl)-CO_2-N_2 composition with ~15 wt.% NaCl, <0.02 wt.% KCl and a $T_{h,tot}$ of ~285°C. L3b inclusions are hosted in Cst3 (Figs. 8K-L) and show H_2O-NaCl-(KCl)-(CO_2,N_2) composition with ~14 wt.% NaCl, <0.02 wt.% KCl and a $T_{h,tot}$ of ~290°C. The fluid chloride molality of L3a fluids is 2.5 ± 0.1 (1σ) mol kg^{-1} and of L3b fluids 2.4 ± 0.1 mol kg^{-1}.

4.4 Fluid inclusion LA-ICP-MS analysis

4.4.1 General characteristics and host mineral signal

Representative LA-ICP-MS spectra of fluid inclusions hosted in quartz, montebrasite and cassiterite are shown in Figure 10. The spectra are generally demonstrating fast wash-out times (<20s) with high signal intensities above background for the elements measured, especially in quartz and cassiterite host minerals. Numerical results of the LA-ICP-MS analyses of the individual fluid inclusions are given in Appendix C. Summary statistics and elemental evolutions are shown in Figures 11 and 12. The fluid geochemistry will be discussed from the wall, intermediate, greisen replacement to the core zone representing a sequence from outer to inner units.

4.4.2 Fluid composition

The alkali metal content (Figs. 11A-H) is characterised by generally high concentrations. Lithium shows similar concentration ranges in the wall zone, intermediate zone and greisen replacement zone (870-2810 ppm) but the Li content increases to concentrations of 4200 ppm, 11960 ppm and 15860 ppm in quartz, montebrasite and cassiterite, respectively, in the core zone. In contrast, Na demonstrates a general decline along the internal zones from 65000 ppm to 22000 ppm from wall zone to core zone. The K concentration is variable and the interquartile ranges (IQR) per zone varies from 7700-33350 ppm, 20730-36900 ppm, 22090-45560 and 1037-59827 ppm in the wall zone, intermediate zone, greisen replacement zone and core zone, respectively. This Li-Na-K evolution is in line with the microthermometrically derived data (Figs. 7A & B). Rubidium and Cs concentrations are also variable and do not show an evolution which is related to the internal zonation or host mineral evolution. Rubidium and Cs have IQR between 395-115 ppm and 120-615 ppm.

The earth alkali metal evolution is provided in Figures 11I-K. Magnesium contents are characterised by a general decline from wall zone to core zone with IQR per zone of 530-15220 ppm, 3440-4820 ppm, 1020-9240 and 110-2140 ppm in the wall zone, intermediate zone, greisen replacement zone and core zone, respectively. Barium IQR overlap between the zones

(5-390ppm) and this is similar for Sr (20-300 ppm). The transition metal evolution in Figures 11L & M shows that the Fe IQR overlap between zones (560-12790 ppm) while Mn declines from wall zone to core zone with average values from 2440 to 15 ppm.

The concentration evolution of the ore elements Nb, Sn, Ta and W together with the flux element P are shown in Figures 11N-R. In general, all ore elements except for W occur in concentration above 100 ppm. Phosphorus concentrations are high in the wall zone, intermediate zone and greisen replacement zone with average values evolving from 12500 ppm in the wall zone to 4000-5000 ppm in the intermediate zone and replacement zones. The phosphate-mineral rich core zone has low phosphorus contents around 90 ppm with substantial number of analyses below detection limit. Niobium and Ta contents are high in the wall zone with IQR of 3.8-26 ppm Nb and 1.4-47 ppm Ta but lower in the intermediate zone with IQR of 5.6-7.1 ppm Nb and 5.4-5.6 Ta. However, the greisen replacement zone in the intermediate zone has very high contents with IQR of 106-351 ppm Nb and 142-404 ppm Ta. The core zone is also enriched with IQR of 88-116 ppm Nb and 90-256 ppm Ta. Also the Sn content is already high in the wall zone with IQR of 34-195 ppm and increases in the intermediate zone with IQR of 57-1475 ppm. The greisen replacement zone in the intermediate zone has the highest Sn content with IQR of 316-5100 ppm. The core zone is also enriched with IQR of 1246-1986 ppm. Tungsten contents are generally lower than the other ore elements and have IQR of 1.5-38 ppm, 10-18 ppm, 2.4-6.2 ppm and 0.4-14 ppm in the wall zone, intermediate zone, greisen replacement zone and core zone, respectively.

In Figures 12A-F the concentration (in ppm) of Li, Na, K, Rb, Cs and Sn are plotted as a function of the molality of Cl (mol kg^{-1}) in the fluid phase, as derived from microthermometric data. These elements dissolve primarily as chlorine complexes in the fluid phase (cf. Zajacz et al., 2008). LiCl, NaCl and KCl can be regarded as the most abundant chloride components in pegmatitic fluid, and together with RbCl and CsCl, they represent the prevalent chlorides of monovalent cations. For chlorine-complexing cations the fluid-melt partition coefficient should be

693 linearly proportional to the molality of Cl to the power of the charge of the specific cation in the
694 fluid phase (i.e. 1 for Li, Na, K, Rb, Cs and 2 and 4 for Sn; cf. Schmidt, 2018) if one assumes
695 dissolution as neutral complexes and constant activity coefficients (Zajacz et al., 2008). The
696 fluid concentrations do not show a linear trend for the monovalent alkali metals or a power-law
697 trend for Sn as a function of the fluid molality of Cl, indicating that parameters other than melt-
698 fluid partitioning also played a role in the distribution of these elements. In Figure 12G & H, the
699 concentration (in ppm) of Sn and Nb+Ta are log-log plotted as a function of the P concentration
700 (ppm) in the fluid phase, which shows a near linear correlation. It is tempting to attribute the
701 near exponential correlation of the Sn and Nb+Ta ratios to a causal 'power-law'-type of process
702 such as melt-fluid partitioning. However, one may not a priori rule out the possibility that other
703 processes, such as fluid-mineral reactions or the role of phosphorous as a flux cause this
704 correlation. This will be evaluated in the discussion section 5.4. Consequently, in order to be
705 able to evaluate the role of fluid-mineral reactions on element distribution, the molar
706 concentration (mmol kg^{-1}) of Na versus K was plotted in Figure 12I. Based on petrography, the
707 predominant fluid-mineral reactions involve microcline albitisation and feldspar muscovitisation
708 for which the reaction vectors are provided in Figure 12I. The plot indicates that especially for
709 the wall zone and intermediate zone (cf. L1 fluids), i.e. zones where cleavelanditic albitisation
710 reactions are petrographically prevalent and for which the associated fluid types are
711 characterised by variable Na and K contents (cf. Fig. 11), that the observed variability in Na and
712 K content can be dominantly attributed to intense albitisation of microcline.
713

714 ## 5. Discussion

715 ### 5.1. Paragenetic and compositional evolution of the Gatumba fluid system

716 Based on the petrography of the internal mineralogical anatomy, the GDS demonstrates a
717 paragenetic sequence of solidification from the border zone inwardly to the core zone and the

superimposed formation of first cleavelandite after microcline and later greisen replacement zone in the intermediate and wall zone. Associated with this mineralogical paragenesis, fluid inclusions studied from the different internal zones illustrate a first major evolution from L1 to L2 fluids from the wall zone to the core zone. Within this paragenetic framework, it is important to evaluate also the relative timing of cleavelandite after microcline and greisen formation. More specifically, the formation of these replacement zones is intrinsically related to the solidification history of the intermediate zone. The replacement zone originated before the core zone solidified, or alternatively, the replacement zone is the product of a final stage process acting after complete solidification of the GDS. This forms part of the discussion in the following sections.

5.1.1 Alkali element evolution

Inclusion petrography, microthermometry and micro-analyses demonstrate that saline L1 fluids, with ~20 wt.% NaCl, ~3 wt% KCl and a H_2O-NaCl-KCl-(CO_2,N_2) composition, were already present as primary inclusions during initial crystallisation of the GDS and the formation of wall zone and intermediate zone. The high Na/K mass ratio of the L1 fluid (i.e. 4.8-6.7) is typical for magmatic-hydrothermal fluids which equilibrated with an evolved peraluminous melt (e.g. Yardley and Bodnar, 2014). Moreover, the evolution and variability of the Na and K molar concentrations in the L1 fluids indicate that the composition of this fluid is modified by intense albitisation of microcline. The latter reaction altered the primary feldspar mineralogy of the intermediate zone and wall zone to cleavelandite-dominated assemblages. During further internal mineralogical differentiation and solidification, the GDS fluid system evolved to a Li-enriched composition in the core zone as demonstrated by the presence of the primary and saline L2 inclusions with 5-12 wt.% NaCl, 1-10 wt.% LiCl and a H_2O-NaCl-LiCl-(CO_2,N_2) composition. The transition from L1 to L2 fluid is expressed by Na and K decrease and Li increase which is associated with the transition from the wall zone and intermediate zone

744 towards the core zone (cf. Figs. 7A & B, 11A-C). A decrease in Na and K can be ascribed to the
745 widespread feldspar fraction, i.e. massive magmatic microcline and metasomatic albitic
746 cleavelandite crystallisation in the wall zone and intermediate zone. As the only Li-compatible
747 mineral phases in the wall zone and intermediate zone are trioctahedral micas and spodumene
748 and as the primary mineralogy in these zones is volumetrically dominated by Li-incompatible
749 phases (i.e. microcline, plagioclase and quartz, cf. Fig. 3; London, 2008), it can be expected that
750 the bulk distribution of Li is incompatible during mineral fractionation from the wall zone towards
751 the core zone. In L1 fluids with a chloride molality of ~4.0 mol kg^{-1}, Li can be expected to be
752 weakly soluble with a bulk fluid/melt distribution coefficient around 1.3 (Iveson et al., 2019). As
753 such, combined crystal/melt incompatible and fluid/melt soluble partitioning behaviour of Li
754 during fractional crystallisation in a coexisting crystals-melt-fluid system produces an overall
755 increase of the bulk Li content in the melt and fluid phase with advancing fractionation. This can
756 explain the change in composition from a Li-poor L1 fluid towards a Li-rich L2 fluid. However, if
757 alkali metal partitioning would be solely governed in the GDS by equilibrium fractionation in a
758 coexisting crystals-melt-fluid system, also a general power-law increase in the fluid Rb and Cs
759 content would be expected from wall zone to core zone. However, this is not observed (cf. Figs.
760 11D-H). In addition, the alkali metal fluid concentrations as a function of the fluid molality of Cl
761 do not show a linear correlation (Fig. 12A-E) which indicates that parameters other than melt-
762 fluid fractionation also played a role in the distribution of these elements. As K-feldspars are
763 important reservoirs for Rb and Cs in pegmatites (e.g. Hulsbosch et al., 2014) and especially in
764 terms of their abundance in the intermediate zone of the GDS (Hulsbosch et al., 2014),
765 albitisation of primary microcline is a significant process to redistribute rare alkali metals
766 between fluid and mineral phases. Consequently, albitisation of K-feldspars can explain the
767 observed variable fluid Rb and Cs contents and the deviation from their expected increasing
768 fractionation trend.

The L2 fluid is restricted to the core zone. The core zone consists dominantly of a cogenetic assemblage of mutually overgrowing F-poor montebrasite with blue carbonated Mn-fluorapatite, coarse quartz, euhedral prismatic cassiterite Cst2 and accessory intercrystal albite. L2a subtype fluid is observed in montebrasite and Cst2 while the L2b subtype occurs in quartz. Petrography indicates that montebrasite and fluorapatite crystallised first, followed by Cst2 and quartz. The observed lowering in the Li content and increase in the Na and CO_2 contents from L2a to L2b are interpreted to be caused by montebrasite crystallisation in the closed core system.

In summary, a change from a L1 to L2 fluid composition is observed during internal differentiation and solidification of the GDS. This evolution demonstrates 1) that a saline aqueous, magmatic-hydrothermal fluid was generally present during the complete crystallisation, 2) its chemistry evolved from L1 to L2 composition from wall zone to core zone, 3) the compositional evolution is caused by magmatic feldspar fractionation but also fluid-feldspar reactivity, 4) that the cleavandite after microcline in the replacement zone is an intrinsic part of the crystallisation history of the intermediate zone and must have formed before the core zone with its typical L2 fluid composition and 5) that small-scale compositional variations within one fluid type (e.g. L2a versus L2b) are produced by sequential crystallisation of mineral phases and the subsequent elemental fractionation between fluid and mineral.

5.1.2 Crystallisation conditions and fluid-rock interaction

The L1 inclusions represent the most primary aliquots of the magmatic-hydrothermal fluid present during initial solidification of the GDS and the formation of the marginal internal zones. Although the microthermometric and compositional data indicate that the L1a and L1b inclusions are mostly similar (cf. Fig. 7), two parameters differ between the two subtypes. Namely, L1a subtype inclusions have generally lower $T_{h,tot}$ (265°C) compared to L1b inclusions (355 °C; Fig. 7F; Table 1) and they also contain Mn^{2+} and Fe^{2+} carbonates as trapped solids

795 (Fig. 8A; Table 1). In addition, L1a subtype inclusions prevail in marginal dyke zones, i.e. wall
796 zone, while L1b inclusions are more present dyke-inward in the intermediate zone. These
797 observations in combination with the presence of flaring-inwards black dravite-schorl series
798 tourmaline crystals, based on Raman analysis, both in the border zone and country rocks and
799 holmquistite replacement units in the mafic country rock indicate interaction of the water-
800 saturated pegmatitic melt with the country rock. The formation of $(Fe\text{-}Mg)^{2+}$ tourmaline and
801 holmquistite at the pegmatite-country rock contact together with the observation of trapped
802 (Mn^{2+},Fe^{2+}) carbonates in the L1a fluids, demonstrate Li-B metasomatic reactions and mineral-
803 fluid exchange reactions between the country rock and pegmatite-derived aqueous fluids (cf.
804 Shearer and Papike, 1988; and references therein).
805 Calculated isochores for the most pristine L1b fluid-subtype (n=31; in quartz) constrain
806 the temperature and pressure conditions of the GDS to a range from 535-560 °C and 5.1-5.6
807 kbar (Fig. 9). Based on a summary of published estimates of the pressure-temperature regimes
808 for pegmatites (350-780 °C and 2-6 kbar; London, 2018), the GDS falls within the medium-high
809 temperature and relatively high intrusion pressure domain, similar to the simple Vlastějovice
810 pegmatites, Czech Republic (600–640 °C and 4.2–5.8 Kbar, , Ackerman et al., 2006), the
811 simple muscovite-cassiterite-rich East Kemptville tin pegmatites, Canada (550-600 °C, Kontak
812 et al., 2001) and the highly fractionated LCT-type rare-element Varuträsk pegmatite, Sweden
813 (450-600 °C Siegel et al., 2016).These conclusions on crystallisation conditions and associated
814 fluid-driven country rock reactions provide additional confirmation that the GDS melt system was
815 water-saturated already at the onset of solidification.
816
817 ## 5.2. Greisen fluid system
818 The formation of metasomatic muscovite-quartz-(cassiterite) greisen replacement zone pockets
819 is spatially restricted to the wall zone and intermediate zone of the GDS. Primary magmatic
820 assemblages in the wall zone and intermediate zone host L1 inclusions for which the

composition is affected by feldspar crystallisation. Both quartz and cassiterite in the greisen pockets (Cst3) host L3 inclusions, i.e.L3a and L3b, respectively. As L3a and L3b subtype inclusions show a similar H_2O-NaCl-(KCl)-(CO_2,N2) composition, similar salinity range (14-15 wt.% NaCl) and final homogenisation temperature range (~285 °C). The only difference in microthermometric properties is the slightly higher CO_2 partial pressure in the L3a inclusions in quartz.

A comparison of the LA-ICP-MS results (Fig. 11) indicates that only Cs is more enriched in the L3 fluids while the other alkali (earth) and transition metals have overlapping concentration ranges. Also the molar concentration range of Na versus K of the L3 fluids, as plotted in Figure 12I, shows a similar spread towards lower Na and higher K as for the L1 fluids. This concentration spread in the L1 fluids is dominantly related to albitisation of microcline in the intermediate zone (see section 5.1.1). However, the compositional transition of L1 to L3 fluid cannot be caused by pure muscovitisation of albite or microcline because these reactions do not change or even increase the Na content of the L3 fluid (cf. Fig. 12I). Hulsbosch et al. (2014) and Hulsbosch (2016) analysed the composition of the micas in the greisen pockets of the GDS and reported that they contain between 1.53 and 4.82 wt.% Li_2O (0.81-2.42 apfu) and Cs levels of 101-499 ppm. These micas have been classified as belonging to the Li-muscovite-trilithionite trend (Hulsbosch, 2016). Paragenetically, the timing of greisen formation can only be constrained to occur after crystallisation of the wall zone and intermediate zone and after formation of the cleavelandite replacement zone. The lower $T_{h,tot}$ of the L3 fluids in comparison to the L1b fluids, indicates that greisen formation occurred as a subsolidus metasomatic alteration phase substantially disconnected from the magmatic crystallisation of the wall zone and intermediate zone and formation of the cleavelandite replacement zone. Moreover, during pegmatite fractionation Cs is incompatible with respect to most minerals (Hulsbosch et al., 2014), and also as a very soluble element in aqueous fluids (e.g. Zajacz et al., 2008) which causes Cs to become enriched in late-stage fluids. The observed enrichment of Cs in L3 fluids

847 compared to L1 fluids and also the high Cs levels in the greisen micas both point towards an
848 origin and timing of the greisen replacement zone as a late-stage metasomatic replacement of
849 the primary wall zone and intermediate zone and cleavelandite replacement zone by a
850 compositionally different L3 fluid system. Fluid-rock reactions like muscovitisation consume
851 hydrogen which in turn increase the pH and cause the precipitation of cassiterite from L3 fluid
852 (i.e. hydrolysis). Primary microcline and secondary cleavelandite in the wall zone and
853 intermediate zone react with the L3 fluid resulting in the formation of a muscovite-quartz
854 assemblage (Hulsbosch, 2019).
855

856 ## 5.3. Water saturation during disequilibrium crystallisation

857 Based on the presence of primary inclusions in wall and core zone quartz, phosphates and
858 cassiterite, and the presence of replacive units in wall and intermediate zones of the GDS, it is
859 inferred that a magmatic-hydrothermal volatile phase was distinctly present throughout the
860 entire crystallisation sequence of the GDS from wall to core zone and subsequently during
861 subsolidus alteration. However, for haplogranitic melts crystallising at equilibrium conditions,
862 water solubility is approximately 10 wt.% at ~5 kbar and ~600 °C (e.g. Holtz et al., 2001). The
863 accumulation of B through fractional crystallisation further enhances the solubility of H_2O in such
864 melts. The effect of P on the H_2O solubility is found to be negligible in natural melt compositions
865 (Holtz et al., 1993). Therefore, if we assume the maximum melt H_2O solubility at the inferred P-T
866 conditions and melt composition of the GDS was a minimum of ~10 to ~15 wt.%, the total H_2O
867 content of the system should have exceeded, under equilibrium conditions, this very high
868 solubility. Granitic pegmatites, nonetheless, are accepted to crystallise by extreme liquidus-
869 undercooling giving rise to disequilibrium crystallisation conditions. Recently, experimental
870 findings by London and Morgan (2017) and Sirbescu et al. (2016) indicated that during these
871 disequilibrium crystallisation conditions of giant crystals (feldspar, petalite etc.) in pegmatites,

872 fluid saturation was observed to be localised and taking place in the front of fast growing
873 minerals. Also in natural pegmatite systems, Hulsbosch et al. (2019) observed that fast and
874 disequilibrium growth of tourmaline played a major role in the formation of locally water-
875 saturated, heterogeneous melt pools at the crystallisation front of the large crystals. Tourmaline
876 growth under these conditions caused the formation of local, water-saturated boro-
877 aluminosilicate melt compositions due to the pile-up of incompatible and excess components,
878 like H_2O or SiO_2, in the mineral crystallisation front. Based on these findings, we interpret that
879 disequilibrium growth of (near)-anhydrous mineral assemblages, such as massive primary
880 perthitic microcline in the wall and intermediate zone, likely caused the formation of, at least
881 locally, water-saturated melt compositions at the crystallisation front of these giant crystals.
882 Although water saturation is likely spatially localised, it occurred already paragenetically early in
883 the crystallisation sequence of the internal zones of the GDS and intensified during core
884 formation with the development of fracture mesh textures and globular crystal textures of quartz
885 and phosphates.
886

887 ## 5.4. Multiphase Sn crystallisation from a disequilibrium pegmatite melt-fluid system

888 The stabilisation of spodumene, montebrasite, tourmaline and apatite in the GDS evidence the
889 presence of elevated concentrations of the fluxes Li, P, B. However, the fluorine content of the
890 GDS can indirectly be expected to be low because 1) even the most evolved and fractionated
891 internal zone, i.e. core zone, contains montebrasite with low fluorine contents representing
892 fluorine concentrations in the melt of <0.5 wt.%, and 3) the general absence of the dominant
893 fluorine bearing minerals topaz, fluorite, lepidolite or triplite. Associated with the internal
894 differentiation of the GDS, three phases of cassiterite mineralisation have been documented: 1)
895 Cst1: cassiterite occurring as a rare, primary sub- to euhedral phase in magmatic microcline-
896 quartz units of the wall zone, 2) Cst2: cassiterite occurring as primary, sub- to euhedral phase in

897 an assemblage with coarse quartz, F-poor montebrasite, carbonate- Mn-fluorapatite, varulite
898 and minor albite in the core zone, and 3) Cst3: secondary cassiterite occurring in intermediate
899 zone and wall zone in metasomatic, replacive greisen pockets together with quartz and Li-rich
900 micas.

901 The planar textural relationships between the contacts of Cst1 with magmatic-stage
902 quartz, albite-oligoclase and microcline (cf. Figs. 2D & E) in the wall zone suggests
903 contemporaneous growth relationships which in turn indicate that disseminated Cst1 crystallised
904 is magmatic-hydrothermal in the wall zone. Linnen et al. (1992) reported similar planar but also
905 embayment textures in magmatic-hydrothermal cassiterite of the Nong Sua pegmatites,
906 Thailand. The embayment textures are therefore interpreted to be caused by etching-resorption
907 processes induced by fluctuations between saturation and undersaturation of cassiterite at
908 aqueous liquid-saturated melt conditions. The fact that saline L1b type fluids occur as primary
909 fluid inclusions in both quartz and Cst1 from the wall zone strongly indicates that Cst1 is
910 magmatic-hydrothermal and began to crystallise at conditions of aqueous fluid saturation. Also
911 the fracture mesh texture in the core zone, which developed globular crystal textures of quartz,
912 cassiterite (Cst2) and primary phosphates, points to fluid-saturated (i.e. L2 fluid) melt conditions
913 during core formation and Cst2 crystallisation. As such, both Cst1 and Cst2 texturally indicate
914 crystallisation from an at least locally water-saturated melt. The formation of quartz-mica-
915 cassiterite greisen pockets in felsic rocks is generally interpreted to be caused by late-stage,
916 closed-system fluid-rock reactions and have been studied for the GDS, and other Rwandese
917 pegmatite systems, by Dewaele et al. (2011) and Hulsbosch et al. (2016; and references
918 therein). Subsolidus, hydrothermal cassiterite precipitation is favoured by oxidation (with H_2
919 consumption), acid neutralisation and especially decreasing fluid chorinity (see equations 3 and
920 4 in Hulsbosch et al., 2016). These precipitation mechanisms can take place by reaction of the
921 hydrothermal fluid with aluminosilicate phases within the pegmatite dyke. Acid-consuming
922 reactions (i.e. hydrolysis) further balance the acidity that has been liberated during precipitation

of cassiterite by destabilisation of water-soluble, Sn-chloride complexes. More specifically for the GDS, acidity is likely consumed during interaction of the mineralising L3 fluid with feldspars in the wall and intermediate zone, and resulted in the observed decrease in chlorinity (see Figs 12 & 3) and the formation of muscovite-quartz greisen assemblages rich in cassiterite. For this reason, late-stage L3 fluids are genetically associated with the subsolidus, hydrothermal precipitation of Cst3.

At magmatic-hydrothermal conditions, Sn is generally assumed to dissolve in aqueous fluids as Sn(II,IV)-Cl complexes (Duc-Tin et al., 2007; Migdisov and Williams-Jones, 2005; Schmidt, 2018). Duc-Tin et al. (2007) determined fluid-solubilities of Sn in chlorine-bearing aqueous fluids at 700 °C, 1.4 kbar and at a log oxygen fugacity of ~NNO. They report that Sn solubilities increase with increasing chlorine concentration in the fluid, ranging from 100 to 800 ppm in NaCl-bearing fluids (5–35 wt.% NaCl) and from 0.8 to 11 wt.% in HCl-bearing fluids (0.5–4.4 m HCl). However, Sn concentrations in the fluid phase of the GDS (Fig. 12F) do not show any systematic variation with molality of Cl (mol kg^{-1}). Instead, within one fluid type (L1, L2 and L3) a complete range of Sn concentrations is observed. An explanation is that the Sn concentrations in the fluid are buffered by local cassiterite saturation. This is in line with the presence of embayment textures in cassiterite caused by fluctuations in cassiterite saturated and undersaturated conditions. Moreover, a comparison of the Sn fluid concentrations in the GDS with published Sn solubilities in HCl- and NaCl-bearing fluids (Fig. 13) demonstrates that all fluids in the GDS, i.e. L1, L2 and L3, have Sn fluid concentrations between the solubility limits of HCl- and NaCl-bearing fluids. The fluid exsolved from the GDS melt should have a very low HCl content because of 1) the magmatic stability of feldspar in the intermediate zone and wall zone, 2) the L1, L2 and L3 fluids are generally characterised by high NaCl salinities, and 3) the equilibrium exchange constant for hydrogen-sodium between a vapour+brine mixture and silicate is inversely proportional to the total chloride concentration (Williams et al., 1997). As a result, aqueous Sn solubilities in the GDS likely correspond to the lower values as determined in

experimental NaCl-containing fluids (Fig. 13) (Duc-Tin et al., 2007). Comparison of the Sn fluid concentrations with solubility data in NaCl-bearing aqueous fluids provide evidence that all fluids types in the GDS have Sn concentration above the aqueous solubility limits and that the drop in Sn fluid concentration could be explained by local multiphase cassiterite saturation events. Cassiterite melt-solubility data of Linnen et al. (1996) at 850°C, 2 kbar and at a log oxygen fugacity of NNO - 0.82 indicate that cassiterite precipitating directly from a peraluminous melt (ASI of 1.0 and 1.2) only occurs at very high levels of 2.2 to 3.2 wt.% Sn, respectively. In case of the GDS system, it is not expected that the solubility limit of cassiterite in the melt is exceeded because 1) the highest observed Sn fluid concentration is only 9400 ppm, and 2) Sn fractionates preferentially in the fluid phase with reported fluid-melt partition coefficients in the range of 1.5-6.7 for fluids with Cl molalities between 0.5-7.5 mol kg-1 (Zajacz et al., 2008). Consequently, this indicates that the primary cassiterite in the wall and core zones of the GDS (i.e. Cst1 and Cst2) precipitated from the exsolved aqueous fluid which was at the interface with the local melt phase.

In the GDS, Sn and Nb+Ta do, however, show a positive correlation with the phosphorus content of the fluid (Fig. 12G & H). Based on experimental data of Keppler (1994), the P fluid-melt partition coefficient of haplogranite-H_2O-P_2O_5 systems increases from ~0.02 to ~2 with decreasing temperature and increasing pressure and can be expected to be between >1 and 2 for the temperature and pressure conditions similar to those inferred for the GDS. This high fluid affinity of P can explain the very high, i.e. wt.% level, P concentrations measured in some of the fluid inclusions (Fig. 12G & H). However, the fluid inclusion P contents range over ~3 orders of magnitude. This variability is interpreted to be caused by buffering of the fluid P content by stabilisation of apatite in all internal zones of the GDS (see Fig. 3). Especially, the core zone is rich in P-minerals with the stabilisation of apatite and montebrasite. The effect of P-mineral buffering is apparent from the observations that the full range in P concentrations occurs even within one fluid type (e.g. L1; Fig. 12G & H). Moreover, the lowest P fluid contents are observed

in the L2 fluid inclusion in the core zone, where substantial fluid inclusions have P contents below the LA-ICP-MS detection limits (see Appendix C). As Sn, Nb and Ta are defined as “hard acids”, it can be expected that they form relatively strong complexes with P which is a “hard base”. Sn(II)-phosphate complexes are reported to be stable at 25°C (Cigala et al., 2012) and the observed positive correlation could arise from P-complexing. London (1987) and Fiege et al. (2018) pointed out that P in peraluminous systems acts as a flux, which substantially lowers the crystallisation temperature of the melt and in turn allows for extended enrichment of incompatible Sn, Nb and Ta in the melt and subsequently in the fluid due to protracted fractionation. Both complexation as well as fluxing of P can cause the observed correlation between P and the fluid metal content.

6. Conclusion

During crystallisation of the LCT-family, rare-element pegmatites of the Gatumba dyke system (GDS), five internal mineralogical zones developed as a border, wall, intermediate, quartz core and replacement zone. The replacement zones can be further subdivided in cleavelandite after microcline units in the intermediate zone and muscovite-quartz-cassiterite metasomatic greisen pockets in the intermediate and wall zones. During internal differentiation of the GDS, three spatially and physicochemically distinct Sn mineralisation phases formed. Cassiterite crystals are hosted in 1) Cst1: large microcline crystals of the intermediate zone, 2) Cst2: assemblage with quartz, F-poor montebrasite, and carbonated Mn-fluorapatite in the core zone, and 3) Cst3: quartz-muscovite greisen replacement units in the wall and intermediate zones.

The presence of saline, H_2O-NaCl-KCl-(CO_2,N_2) L1 fluid (~20 wt.% NaCl and ~3 wt% KCl) in primary inclusions in the magmatic mineral assemblages of the wall and intermediate zone demonstrates that the melt was already saturated at the onset of crystallisation. Isochore reconstruction of the L1 fluids enable determination of the crystallisation temperature and pressure of the GDS which ranges from 535-560 °C and 5.1-5.6 kbar. Primary L1 fluid

1001 inclusions are also present in disseminated Cst1 crystals in the wall zone. Textural relationships
1002 between the Cst1 and magmatic-stage quartz, albite-oligoclase and microcline demonstrate that
1003 Cst1 formed in the magmatic- hydrothermal stage. The presence of embayment textures in Cst1
1004 are, moreover, indicative for etching-resorption processes induced by fluctuations between
1005 saturation and undersaturation of cassiterite at L1 fluid-saturated melt conditions. Extensive
1006 microcline fractionation and subsequent metasomatic cleavandite after microcline replacement
1007 reactions in the intermediate zone induced a compositional transition of the L1 fluid chemistry
1008 towards a Li-enriched, Na-depleted H_2O-NaCl-LiCl-(CO_2,N_2) L2 fluid in the core zone minerals
1009 (6-12 wt.% NaCl,1-10 wt.% LiCl). The transition in fluid chemistry from a L1 to L2 composition is
1010 dominantly governed by cleavelandite replacement reactions. This, in turn, demonstrates that
1011 the formation of this replacement zone is intrinsically related to the crystallisation history of the
1012 intermediate zone and likely formed before the core zone assemblages. The core zone consists
1013 dominantly of a cogenetic assemblage of mutually overgrowing F-poor montebrasite with blue
1014 carbonate- and potentially borate-rich Mn-fluorapatite, coarse quartz, euhedral prismatic Cst2
1015 and accessory intercrystal albite. Primary L2 fluid inclusions are also present in Cst2 crystals in
1016 the core zone. Crystallisation of Cst3 in metasomatic greisen pockets in the wall zone and
1017 intermediate zone occurred in the late-stage, Cs-enriched H_2O-NaCl-(KCl, CO_2,N2) L3 fluid (~15
1018 wt.% NaCl) and distinctly after the cleavelandite replacement processes.
1019 Our petrochemical study demonstrates that the multiphase cassiterite in the GDS formed
1020 from a water-saturated melt system. Fast, disequilibrium growth of (near)-anhydrous mineral
1021 assemblages caused the formation of flux-rich and; at the least locally, water-saturated melt
1022 compositions at the crystallisation front of the crystals. The reported preferential melt-fluid
1023 partitioning of Sn towards the saline aqueous magmatic-hydrothermal fluid phase with low HCl
1024 concentrations and the reported low solubility (<800 ppm Sn) of Sn in such fluids (Duc-Tin et al.,
1025 2007; Williams et al., 1997; Zajacz et al., 2008), indicate that the primary cassiterite in the wall
1026 and core zones of the GDS (i.e. Cst1 and Cst2) likely formed from the exsolved aqueous fluid

which was at the interface with the local melt phase. Late-stage, secondary cassiterite (Cst3) precipitation in the greisen pockets is purely hydrothermal and driven by metasomatic hydrolytic fluid-rock reactions.

Acknowledgements

We would like to express our gratitude to Marie-Christine Boiron (Université de Lorraine, CNRS, CREGU) for access to the LA-ICP-MS lab and for fruitful discussions. The assistance of Fernando Prado Araujo (KU Leuven) with the microprobe analyses is much appreciated. We also thank Stijn Dewaele (UGhent – RMCA) for his participation in the field work, the loan of rocks of the RMCA collection and for shearing his expertise. We are grateful to Kris Piessens (Geological Survey of Belgium, RBIN) for access to the Raman spectrometer. Thanks also goes to Herman Nijs (KU Leuven) for preparing the high-quality thin and doubly polished sections. We are grateful to the two LITHOS reviewers for their constructive reviews, which helped us to improve the quality of this manuscript, and to Michael Roden for his editorial work. Research of Niels Hulsbosch is funded by a postdoctoral fellowship of the Research Foundation – Flanders (FWO). Philippe Muchez and Niels Hulsbosch acknowledge the financial support for this project by research grant C14/17/056 of the KU Leuven Research Fund.

Appendix

A. Host minerals FEG-EPMA and LA-ICP-MS analyses

Tables A.1, A.2 and A.3 report the major element composition of montebrasite, blue apatite and the three generations of cassiterite, respectively, as determined by FEG-EPMA analyses. Table A.4 reports, additionally, the trace element composition as determined by LA-ICP-MS of the specific minerals montebrasite and three generations of cassiterite, which host fluid inclusions. Specifically for cassiterite, FEG-EPMA analyses reports the composition of both light coloured (optically transparent) and dark coloured (optically opaque) zones in cassiterite whereas LA-ICP-MS analyses only document light coloured zones as these are hosting observable fluid inclusions.

1059 Table A.1. Major element composition of montebrasite.

Analysis	1440_Mon1	1440_Mon2	1440_Mon3	1440_Mon4	1440_Mon5	1440_Mon6	1440_Mon7	1440_Mon8	1440_Mon9	1440_Mon10	$\bar{x}$	σ
Li_2O (wt.%)*	10.22	10.22	10.22	10.22	10.23	10.22	10.22	10.23	10.22	10.22	10.22	0.003
CaO	0.02	0.01	0.02	0.02	0.01	0.01	0.01	0.01	0.02	0.01	0.01	0.005
P_2O_5	50.14	50.21	50.53	50.53	51.01	48.81	50.51	50.47	49.61	50.47	50.23	0.55
Al_2O_3	36.20	36.51	36.24	36.24	35.99	36.24	36.03	36.58	36.66	36.59	36.33	0.21
F	2.46	3.14	2.66	2.66	2.52	2.51	2.52	2.59	2.50	2.78	2.63	0.18
H_2O*	1.94	1.72	1.88	1.88	1.93	1.91	1.92	1.91	1.92	1.85	1.88	0.06
O=F	1.04	1.32	1.12	1.12	1.06	1.06	1.06	1.09	1.05	1.17	1.11	0.08
sum	99.95	100.49	100.43	100.43	100.63	98.64	100.15	100.69	99.87	100.74	100.20	

1060 *Formulae were calculated on the basis of 5 oxygens: Li = 1 - (Na + K) and OH = 1 - F.

1061 Table A.2. Major element composition of blue apatite.

Analysis	1440_Apa1	1440_Apa2	1440_Apa3	1440_Apa4	1440_Apa5	1440_Apa6	1440_Apa7	1440_Apa8	1440_Apa9	1440_Apa10	$\bar{x}$	σ
CaO (wt.%)	53.04	55.06	54.61	53.76	54.96	54.50	53.17	53.31	52.79	53.40	53.86	0.76
MnO	1.70	1.05	2.61	3.32	1.76	1.62	1.91	1.99	1.34	1.74	1.90	0.58
P_2O_5	41.76	42.26	40.19	40.77	39.80	40.67	39.94	39.98	40.49	41.27	40.71	0.74
B_2O_3	0.01	0.04	0.72	0.80	0.01	0.01	0.07	0.01	0.01	0.02	0.17	0.28
F	2.86	2.75	3.04	2.84	2.88	3.04	2.84	2.71	2.69	2.68	2.83	0.12
Cl	0.02	0.01	0.04	0.01	0.03	0.01	0.02	0.04	0.04	0.02	0.02	0.01
H_2O*	0.40	0.49	0.30	0.42	0.36	0.31	0.37	0.42	0.43	0.48	0.40	0.06
O=F,Cl	1.21	1.16	1.29	1.20	1.22	1.28	1.20	1.15	1.14	1.13	1.20	0.05
sum	98.58	100.48	100.22	100.72	98.58	98.87	97.12	97.31	96.65	98.47	98.70	
OH (apfu*)	0.454	0.544	0.341	0.475	0.416	0.350	0.428	0.493	0.504	0.547	0.455	0.065
F	1.542	1.453	1.649	1.521	1.576	1.647	1.567	1.495	1.484	1.448	1.538	0.065
Cl	0.004	0.003	0.011	0.003	0.008	0.003	0.005	0.012	0.012	0.004	0.007	0.003

1062 *Formulae were calculated on the basis of 25 oxygens: H_2O calculated on the basis of filling the C site

1063 Table A.3. Major element composition of cassiterite.

Analysis*	1037_cst1D_1	1037_cst1L_2	1037_cst1L_3	1037_cst1L_4	1037_cst1L_5	1037_cst1L_6	$\bar{x}$	σ
SnO_2 (wt.%)	100.11	99.75	100.04	99.60	99.12	99.95	99.76	0.34
Nb_2O_5	0.16	0.05	0.05	0.10	0.10	0.04	0.08	0.04
Ta_2O_5	0.26	0.11	0.11	0.01	0.01	0.11	0.10	0.08
WO_3	0.01	0.05	0.02	0.07	0.09	0.05	0.05	0.03
FeO	0.05	0.04	0.03	0.01	0.02	0.03	0.03	0.01
MnO	<213 ppm	<254 ppm	<312 ppm	<222 ppm	<297 ppm	<247 ppm		
MgO	0.01	0.39	0.39	0.42	0.44	0.39	0.34	0.15
TiO_2	0.10	0.07	0.10	0.05	0.06	0.07	0.08	0.02
SiO_2	0.01	0.02	0.18	0.26	0.24	0.01	0.12	0.11
Sum	100.71	100.48	100.91	100.51	100.08	100.65	100.56	

Analysis*	1440_cst2L_1	1440_cst2D_2	1440_cst2D_3	1440_cst2L_4	1440_cst2L_5	1440_cst2L_6	1440_cst2D_7	1440_cst2D_8	1440_cst2D_9	$\bar{x}$	σ
SnO_2 (wt.%)	99.46	96.55	99.08	98.60	98.32	98.77	97.57	98.09	98.29	98.30	0.77
Nb_2O_5	0.06	0.72	0.28	0.01	0.02	0.08	0.69	1.16	0.55	0.40	0.36
Ta_2O_5	0.01	0.92	0.32	0.01	0.01	0.01	0.90	1.42	0.68	0.47	0.47
WO_3	0.03	0.04	0.07	0.06	0.07	0.05	0.05	0.02	0.03	0.05	0.02
FeO	0.02	0.26	0.10	0.01	0.02	0.02	0.26	0.43	0.19	0.15	0.13
MnO	<214 ppm	<233 ppm	<278 ppm	<288 ppm	<213 ppm	<239 ppm	0.01	0.01	<198 ppm	0.01	0.00
MgO	0.31	0.36	0.42	0.39	0.39	0.37	0.35	0.37	0.37	0.37	0.03
TiO_2	0.06	0.06	0.06	0.05	0.06	0.04	0.06	0.10	0.06	0.06	0.02
SiO_2	0.21	0.18	0.24	0.21	0.01	0.22	0.20	0.05	0.23	0.17	0.07
Sum	100.15	99.09	100.57	99.33	98.92	99.54	100.08	101.64	100.40	99.98	

Analysis*	1023_cst3L_1	1023_cst3D_2	1023_cst3L_3	1023_cst3D_4	1023_cst3D_5	1023_cst3D_6	1023_cst3D_7	1023_cst3D_8	$\bar{x}$	σ
SnO_2 (wt.%)	99.13	98.29	99.58	93.64	94.97	96.28	95.97	95.45	96.66	1.87
Nb_2O_5	0.03	0.73	0.06	2.32	1.74	0.85	1.58	1.69	1.13	0.74
Ta_2O_5	0.28	0.42	0.38	1.41	0.89	0.67	0.85	1.12	0.75	0.35
WO_3	0.03	0.04	0.05	0.04	0.03	0.04	0.06	0.06	0.04	0.01
FeO	0.06	0.28	0.06	0.56	0.42	0.29	0.39	0.45	0.31	0.16
MnO	0.02	0.01	0.01	0.08	0.02	0.01	0.04	0.03	0.03	0.02
MgO	0.40	0.37	0.39	0.41	0.37	0.41	0.36	0.38	0.39	0.02
TiO_2	0.10	0.24	0.05	0.11	0.09	0.22	0.10	0.08	0.12	0.06
SiO_2	0.25	0.25	0.29	0.30	0.25	0.29	0.03	0.24	0.24	0.08
Sum	100.30	100.62	100.87	98.87	98.79	99.08	99.38	99.48	99.67	

*Cst1, 2 and 3 refer to the three cassiterite generations (see text). The "D" or "L" indicator refers to optically dark-coloured, opaque versus light-coloured, transparent cassiterite crystals.

1064

Table A.4. Trace element composition of montebrasite and cassiterite.

	Montebrasite (n=6)		Cassiterite 1 (n=5)*		Cassiterite 2 (n=4)*		Cassiterite 3 (n=5)*	
	$\bar{x}$ (ppm)	σ	$\bar{x}$ (ppm)	σ	$\bar{x}$ (ppm)	σ	$\bar{x}$ (ppm)	σ
Li	n.a.	n.a.	0.20	0.02	0.1	0.04	0.3	0.2
Na	25	18	2	1	2	1	6	5
Mg	11	2	0.3	0.2	0.3	0.2	0.20	0.06
K	5	2	0.8	0.3	0.9	0.1	1.6	0.7
Mn	1.2	0.7	11	7	10	7	30	21
Fe	384	8	920	330	890	740	1050	960
Rb	0.6	0.3	0.3	0.1	0.3	0.2	0.50	0.01
Sr	0.4	0.1	0.2	0.2	0.2	0.1	0.3	0.2
Nb	12	0.8	1870	820	1710	930	2400	2100
Sn	85	21	n.a.	n.a.	n.a.	n.a.	n.a.	n.a.
Cs	0.3	0.1	0.06	0.01	0.06	0.01	0.08	0.01
Ba	<0.01	n.a.	0.40	0.03	0.40	0.02	0.40	0.03
Ta	23	3	2300	1500	2300	1700	2800	1700
W	0.02	0.01	0.5	0.1	0.6	0.1	1.6	1.5

*Only transparent cassiterite zones where ablated as they contained observable fluid inclusions.

B. Microthermometry analyses

Table B. Results of the microthermometric analyses of individual fluid inclusions.

Sample	Inclusion	Zone	Host	Paragenesis	Type	Phases	T_{fm} (°C)	$T_{m,hh}$ (°C)	$T_{m,ice}$ (°C)	$T_{m,CO2}$ (°C)	$T_{m,clath}$ (°C)	T_{hCO2} (°C)	$T_{h,tot}$ (°C)	NaCl (wt.%)	KCl (wt.%)	LiCl (wt.%)	Cl (mol kg^{-1})
1	1702-3-H-B-12	WZ	Qz	Prim	L1a	S2LV	-22.6	-14.7	-22.6				252	22.1	4.3		4.36
2	1702-3-H-B-10	WZ	Qz	Prim	L1a	S2LV	-26.3		-22.6				260	21.0	4.4		4.18
3	1702-3-H-B-10A	WZ	Qz	Prim	L1a	S2LV	-26.3		-22.6				269	21.0	4.4		4.18
4	1702-3-H-B-15	WZ	Qz	Prim	L1a	S2LV	-24.6	-14.9	-22.6				254	22.1	4.3		4.35
5	1702-3-H-B-16	WZ	Qz	Prim	L1b	LV	-24.6	-14.6	-22.8				252	21.7	5.0		4.39
6	1702-3-H-B-14	WZ	Qz	Prim	L1a	S2LV	-28.8	-16.8	-22.9				246	21.2	5.4		4.36
7	1702-3-H-B-9	WZ	Qz	Prim	L1a	S2LV	-26.8		-22.4				255	21.4	3.7		4.15
8	1702-3-H-B-17	WZ	Qz	Prim	L1a	S2LV	-26.9	-22.4	-22.4				263	21.4	3.7		4.15
9	1702-3-H-B-2	WZ	Qz	Prim	L1a	S2LV	-27.2		-22.8				259	20.6	5.2		4.21
10	1702-3-H-B-3	WZ	Qz	Prim	L1a	S2LV			-22.9				274	20.4	5.6		4.23
11	1702-3-H-B-4	WZ	Qz	Prim	L1a	SLV	-25.3		-22.9				258	20.4	5.6		4.23
12	1702-3-H-B-20	WZ	Qz	Prim	L1a	SLV			-22.9				261	20.4	5.6		4.23
13	1702-3-H-B-18	WZ	Qz	Prim	L1a	SLV	-25.6	-8.8	-22.9				272	22.4	5.3		4.54
14	1702-3-H-B-19	WZ	Qz	Prim	L1a	SLV			-22.9				253	20.4	5.6		4.23
15	1702-3-H-B-8	WZ	Qz	Prim	L1a	SLV	-25.7	-8.7	-22.7				254	22.8	4.6		4.51
16	1702-3-H-B-21	WZ	Qz	Prim	L1a	SLV	-25.8	-7.8	-22.8				253	22.7	4.9		4.55
17	1702-3-H-A-11	WZ	Qz	(Pseudo)Sec	L1a	S2LV	-24.7	-9.9	-22.7				257	22.6	4.6		4.48
18	1702-3-H-A-25	WZ	Qz	(Pseudo)Sec	L1a	SLV	-25.6	-9.5	-22.4				261	23.2	3.5		4.44
19	1702-3-H-A-26	WZ	Qz	(Pseudo)Sec	L1a	S2LV	-25.6	-12.9	-22.4				263	22.7	3.6		4.37
20	1702-3-H-A-16	WZ	Qz	(Pseudo)Sec	L1a	S2LV	-27.2		-23.7				270	18.4	9.0		4.36
21	1702-3-H-A-19	WZ	Qz	(Pseudo)Sec	L1a	S2LV	-27.3	-9.5	-22.5				266	23.0	3.9		4.46
22	1702-3-H-A-20	WZ	Qz	(Pseudo)Sec	L1a	S2LV	-26.3	-9.5	-22.5				268	23.0	3.9		4.46
23	1702-3-H-A-20A	WZ	Qz	(Pseudo)Sec	L1a	SLV	-27.9	-9.5	-22.5				260	23.0	3.9		4.46
24	1702-3-H-A-14	WZ	Qz	(Pseudo)Sec	L1a	S2LV	-25.2	-3.1	-22.7				251	23.6	4.5		4.64
25	1702-3-H-A-15	WZ	Qz	(Pseudo)Sec	L1a	S2LV	-25.2	-5.7	-22.7				267	23.2	4.5		4.58
26	1702-3-H-A-24	WZ	Qz	(Pseudo)Sec	L1a	S2LV	-25.2	-5.7	-22.7				257	23.6	4.3		4.61
27	1702-3-H-A-22	WZ	Qz	(Pseudo)Sec	L1a	S2LV	-26.4	-5.6	-22.7				266	23.2	4.7		4.60
28	1702-3-H-A-10	WZ	Qz	(Pseudo)Sec	L1a	S2LV	-27.2	-5.7	-22.7				258	23.2	4.5		4.58
29	1702-3-H-A-27	WZ	Qz	(Pseudo)Sec	L1b	LV	-25.8	-15.8	-22.9				260	21.4	5.4		4.39
30	1702-3-H-A-28	WZ	Qz	(Pseudo)Sec	L1a	S2LV	-25.8		-22.9				260	20.4	5.6		4.23
31	1702-3-H2-C-10	WZ	Qz	Prim	L1a	SLV	-26.0	-22.9	-22.9				266	20.4	5.6		4.23
32	1702-3-H2-C-5	WZ	Qz	Prim	L1a	SLV	-28.1	-8.4	-22.2				348	23.7	2.9		4.44
33	1702-3-H2-C-7	WZ	Qz	Prim	L1a	SLV	-25.5	-10.1	-22.2				305	23.4	2.9		4.40
34	1702-3-H2-C-6	WZ	Qz	Prim	L1b	LV	-25.5	-6.2	-21.5				359	25.0	0.8		4.39
35	1702-3-I2-B-18	WZ	Qz	(Pseudo)Sec	L1b	LV	-26.7	-22.5	-21.7				320*	20.7	4.0		4.08
36	1702-3-I2-B-7	WZ	Qz	(Pseudo)Sec	L1a	SLV	-26.2	-22.9	-17.4				320*	17.2	4.7		3.57
37	1702-3-I2-B-20	WZ	Qz	(Pseudo)Sec	L1a	SLV	-26.2	-22.2	-22.2				320*	21.7	3.0		4.12
38	1702-3-I2-B-21	WZ	Qz	(Pseudo)Sec	L1a	SLV	-26.3	-22.3	-22.1				310*	21.4	3.4		4.11
39	1702-3-I2-B-4	WZ	Qz	(Pseudo)Sec	L1b	LV	-26.7	-22.6	-22.1				315*	20.7	4.4		4.13
40	1702-3-I2-B-22	WZ	Qz	(Pseudo)Sec	L1a	SLV	-26.2	-22.8	-22.8				320*	20.6	5.2		4.21
41	1702-3-I2-B-23	WZ	Qz	(Pseudo)Sec	L1b	LV	-26.2	-22.8	-22.8				314	20.6	5.2		4.21
42	1702-3-I2-A-3	WZ	Qz	Prim	L1a	S2LV	-27.1	-22.9	-22.5				255	20.7	4.8		4.18
43	1702-3-I2-A-4	WZ	Qz	Prim	L1a	S2LV	-27.1	-22.9	-22.5				266	20.7	4.8		4.18
44	1702-3-I2-A-5	WZ	Qz	Prim	L1a	SLV	-27.1	-21.5	-22.5				257	21.3	4.1		4.19
45	1702-3-I2-A-7	WZ	Qz	Prim	L1a	SLV	-27.1	-21.7	-22.5				263	21.3	4.1		4.18
46	1702-3-I2-A-12	WZ	Qz	Prim	L1a	SLV	-27.2	-4.1	-22.8				255	23.3	4.8		4.63
47	1702-3-I2-D-1	WZ	Qz	Prim	L1a	S2LV	-27.9	-13.6	-22.9				265	21.7	5.4		4.43
48	1702-3-I2-D-2	WZ	Qz	Prim	L1a	S2LV	-26.3	-21.7	-22.9				255	20.5	4.6		4.13
49	1702-3-I2-D-3	WZ	Qz	Prim	L1a	S2LV	-26.4	-14.6	-22.9				260	21.4	5.5		4.39
50	1702-3-I2-D-4	WZ	Qz	Prim	L1a	S2LV	-26.3	-13.9	-22.9				262	21.0	5.3		4.30
51	1702-3-I2-D-5	WZ	Qz	Prim	L1a	S2LV	-27.5	-16.8	-22.8				260	21.0	5.3		4.31
52	1702-3-I2-D-6	WZ	Qz	Prim	L1a	S2LV	-26.9	-15.4	-22.8				260	21.2	5.5		4.36
53	1702-3-I2-D-7	WZ	Qz	Prim	L1a	S2LV	-27.8	-17.1	-22.9				263	20.9	5.5		4.32
54	1037-2-Cst-1	WZ	Cst	Prim	L1b	LV	-26.3	-16.3	-22.7				360	21.4	5.4		4.39
55	1037-2-Cst-2	WZ	Cst	Prim	L1b	LV	-27.0	-16.8	-22.7				360	21.2	5.4		4.34
56	1037-2-Cst-3	WZ	Cst	Prim	L1b	LV	-26.4	-16.5	-22.7				365	21.1	5.2		4.30
57	1037-2-Cst-4	WZ	Cst	Prim	L1b	LV	-26.4	-16.4	-22.7				365	21.3	5.6		4.40

58	1037-2-Cst-5	WZ	Cst	Prim	L1b	LV	-27.1	-15.0	-22.7			365	21.3	5.4	4.37
59	1037-2-Cst-6	WZ	Cst	Prim	L1b	LV	-26.9	-16.9	-22.7			365	21.7	5.1	4.40
60	1037-2-Cst-7	WZ	Cst	Prim	L1b	LV	-26.8	-16.7	-22.7			360	21.2	5.4	4.35
61	1037-2-Cst-8	WZ	Cst	Prim	L1b	LV	-26.8	-16.2	-22.7			365	21.6	5.4	4.42
62	1037-2-Cst-9	WZ	Cst	Prim	L1b	LV	-26.8	-16.9	-22.7			365	21.4	5.3	4.37
63	1449-2-1-A-1	IZ (+Cleav RZ)	Qz	(Pseudo)Sec	L1b	LV	-25.1	-17.8	-22.4		3.4	253	22.0	3.7	4.25
64	1449-2-1-A-2	IZ (+Cleav RZ)	Qz	(Pseudo)Sec	L1b	LV	-23.3	-16.6	-21.9		3.2	249	23.0	2.0	4.20
65	1449-2-1-A-3	IZ (+Cleav RZ)	Qz	(Pseudo)Sec	L1b	LV	-25.2	-14.8	-22.4		3.9	251	22.4	3.6	4.32
66	1449-2-1-A-4	IZ (+Cleav RZ)	Qz	(Pseudo)Sec	L1b	LV	-25.8	-14.8	-22.2			258	22.8	3.0	4.29
67	1449-2-1-A-5	IZ (+Cleav RZ)	Qz	(Pseudo)Sec	L1a	SLV	-24.6	-12.8	-22.3		4.2	255	19.4	0.7	3.42
68	1449-2-1-C-1	IZ (+Cleav RZ)	Qz	(Pseudo)Sec	L1a	SLV	-23.4	-21.5	-16.6			312	20.3	0.8	3.58
69	1449-2-1-C-2	IZ (+Cleav RZ)	Qz	(Pseudo)Sec	L1b	LV	-26.0	-21.5	-17.9			319	20.3	0.7	3.58
70	1449-2-1-C-3	IZ (+Cleav RZ)	Qz	(Pseudo)Sec	L1a	SLV	-24.4	-21.2	-16.8			319	20.0	0.0	3.43
71	1449-2-1-C-4	IZ (+Cleav RZ)	Qz	(Pseudo)Sec	L1a	SLV	-26.9	-20.8	-18.2			325	21.1	0.0	3.62
72	1449-2-1-C-5	IZ (+Cleav RZ)	Qz	(Pseudo)Sec	L1a	SLV	-26.0	-21.0	-17.9			315	20.9	0.0	3.57
73	1449-2-1-C-6	IZ (+Cleav RZ)	Qz	(Pseudo)Sec	L1b	LV	-24.1	-20.8	-18.2			320	21.1	0.0	3.62
74	1449-2-1-C-7	IZ (+Cleav RZ)	Qz	(Pseudo)Sec	L1b	LV	-27.0	-20.8	-18.5			322	21.3	0.0	3.65
75	1449-2-1-C-8	IZ (+Cleav RZ)	Qz	(Pseudo)Sec	L1b	LV	-26.4	-20.8	-18.0			318	20.9	0.0	3.58
76	1449-2-1-C-9	IZ (+Cleav RZ)	Qz	(Pseudo)Sec	L1a	SLV	-23.7	-19.7	-22.9			320	20.9	5.3	4.29
77	1449-2-1-C-10	IZ (+Cleav RZ)	Qz	(Pseudo)Sec	L1b	LV	-26.4	-9.3	-22.7			325	22.8	4.4	4.49
78	1449-2-1-B-1	IZ (+Cleav RZ)	Qz	(Pseudo)Sec	L1b	LV	-25.6	-11.1	-20.3			375	24.6	0.0	4.22
79	1449-2-1-B-2	IZ (+Cleav RZ)	Qz	(Pseudo)Sec	L1b	LV	-26.6	-22.7	-18.1			375	18.2	4.1	3.66
80	1449-2-1-B-3	IZ (+Cleav RZ)	Qz	(Pseudo)Sec	L1b	LV	-26.3	-20.7	-13.8			375	17.6	0.0	3.02
81	1449-2-1-B-4	IZ (+Cleav RZ)	Qz	(Pseudo)Sec	L1b	LV	-26.3	-20.7	-13.8			370	17.6	0.0	3.02
82	1449-2-1-B-5	IZ (+Cleav RZ)	Qz	(Pseudo)Sec	L1b	LV	-26.4	-20.5	-13.8		-2.3	375	17.6	0.0	3.02
83	1449-2-1-D-1	IZ (+Cleav RZ)	Qz	Prim	L1b	LV	-25.9	-20.3	-20.3			381*	23.3	0.0	3.99
84	1449-2-1-D-2	IZ (+Cleav RZ)	Qz	Prim	L1b	LV	-25.9	-4.1	-20.3			391*	25.7	0.0	4.40
85	1449-2-1-D-3	IZ (+Cleav RZ)	Qz	Prim	L1b	LV	-25.9	-4.6	-20.3			371	25.6	0.0	4.38
86	1449-2-1-D-4	IZ (+Cleav RZ)	Qz	Prim	L1b	LV	-25.9	-4.5	-20.3			384*	25.6	0.0	4.39
87	1449-2-1-D-5	IZ (+Cleav RZ)	Qz	Prim	L1b	LV	-25.9	-4.7	-20.3			399*	25.6	0.0	4.38
88	1449-2-1-D-6	IZ (+Cleav RZ)	Qz	Prim	L1b	LV	-25.9	-4.6	-20.3			387	25.6	0.0	4.38
89	1449-2-1-D-7	IZ (+Cleav RZ)	Qz	Prim	L1b	LV	-25.2	-2.3	-19.7			390*	25.9	0.0	4.44
90	1449-2-1-D-8	IZ (+Cleav RZ)	Qz	Prim	L1b	LV	-26.9	-5.6	-22.7			395*	23.3	4.4	4.58
91	1449-2-1-D-9	IZ (+Cleav RZ)	Qz	Prim	L1b	LV	-27.1	-22.7	-21.5		-2.9	395*	20.2	4.5	4.06
92	1449-2-1-D-10	IZ (+Cleav RZ)	Qz	Prim	L1b	LV	-25.5	-20.7	-18.3		-4.7	401*	21.2	0.0	3.63
93	1449-2-1-D-11	IZ (+Cleav RZ)	Qz	Prim	L1b	LV	-28.1	-22.7	-20.7		2.6	389	19.8	4.4	3.97
94	1449-2-1-D-12	IZ (+Cleav RZ)	Qz	Prim	L1b	LV	-27.3	-21.3	-17.3			379*	20.2	0.2	3.50
95	1449-2-1-D-13	IZ (+Cleav RZ)	Qz	Prim	L1b	LV	-27.7	-21.3	-17.3			385*	20.2	0.2	3.50
96	1449-2-1-G-1	IZ (+Cleav RZ)	Qz	Prim	L1b	LV	-26.7	-21.3	-17.3			384	20.2	0.2	3.50
97	1449-2-1-G-2	IZ (+Cleav RZ)	Qz	Prim	L1b	LV	-26.7	-21.3	-17.3			384	20.2	0.2	3.50
98	1449-2-3-A-1	IZ (+Cleav RZ)	Qz	Prim	L1b	LV	-24.9	-5.7	-20.9			289*	25.4	0.0	4.36
99	1449-2-3-C-1	IZ (+Cleav RZ)	Qz	Prim	L1b	LV	-24.9	-19.9	-17.5		0.9	321*	20.5	0.0	3.52
100	1449-2-3-C-2	IZ (+Cleav RZ)	Qz	Prim	L1b	LV	-27.1	-22.4	-17.6		1.1	302*	18.5	3.1	3.57
101	1449-2-3-C-3	IZ (+Cleav RZ)	Qz	Prim	L1b	LV	-25.8	-22.4	-16.9		1.1	307*	18.0	3.0	3.48
102	1449-2-3-C-4	IZ (+Cleav RZ)	Qz	Prim	L1a	SLV	-25.8	-22.3	-17.2			328*	18.4	2.8	3.52
103	1449-2-3-C-5	IZ (+Cleav RZ)	Qz	Prim	L1b	LV	-24.4	-22.0	-16.8		0.9	350*	18.7	2.0	3.46
104	1449-2-3-C-6	IZ (+Cleav RZ)	Qz	Prim	L1b	LV	-24.4	-16.8	-21.8			338*	23.1	1.7	4.17
105	1449-2-3-D-1	IZ (+Cleav RZ)	Qz	Prim	L1a	SLV	-25.5	-20.7	-16.8		-1.3	323*	20.0	0.0	3.43
106	1449-2-3-D-2	IZ (+Cleav RZ)	Qz	Prim	L1a	SLV	-25.5	-20.7	-16.8		1.3	358*	20.0	0.0	3.43
107	1449-2-3-D-3	IZ (+Cleav RZ)	Qz	Prim	L1b	LV	-25.5	-20.7	-16.8		1.7	291*	20.0	0.0	3.43
108	1449-2-3-D-4	IZ (+Cleav RZ)	Qz	Prim	L1b	LV	-23.8	-22.0	-17.1		-3.7	305*	18.9	2.0	3.49
109	1449-2-3-D-5	IZ (+Cleav RZ)	Qz	Prim	L1a	SLV	-23.8	-22.0	-18.3		-2.5	340*	19.8	2.1	3.66
110	1449-2-3-D-6	IZ (+Cleav RZ)	Qz	Prim	L1b	LV	-26.3	-22.7	-18.4		-2.8	346*	18.4	4.1	3.70
111	1449-2-3-D-7	IZ (+Cleav RZ)	Qz	Prim	L1b	LV	-26.3	-22.7	-17.4		-1.9	339*	17.7	4.0	3.56
112	1449-2-3-B-1	IZ (+Cleav RZ)	Qz	Prim	L1a	SLV	-28.7	-22.7	-15.2			386	16.2	3.6	3.26
113	1449-2-3-B-2	IZ (+Cleav RZ)	Qz	Prim	L1a	SLV	-27.7	-22.6	-17.9			386	18.2	3.7	3.62
114	1449-2-3-B-3	IZ (+Cleav RZ)	Qz	Prim	L1b	LV	-26.6	-22.5	-20.7			381	20.2	3.8	3.96
115	1449-2-3-B-4	IZ (+Cleav RZ)	Qz	Prim	L1b	LV	-26.0	-22.7	-17.4		-1.2	380	17.7	4.0	3.56

116	1440-1-1-Cast1	CZ	Cst	Prim	L2a	LV	-73.5	-30.7	-13.8				293	5.5	7.4	2.68
117	1440-1-1-Cast2	CZ	Cst	Prim	L2a	LV	-68.8	-28.7	-16.2				295	7.1	7.1	2.89
118	1440-1-1-Cast3	CZ	Cst	Prim	L2a	LV	-70.9	-28.7	-16.2				294	7.1	7.1	2.89
119	1440-1-1-Cast4	CZ	Cst	Prim	L2a	LV	-70.9	-28.7	-16.2				299	7.1	7.1	2.89
120	1440-1-1-Cast5	CZ	Cst	Prim	L2a	LV	-70.9	-29.7	-13.8				282	6.0	7.0	2.69
121	1440-1-1-Cast6	CZ	Cst	Prim	L2a	LV	-70.9	-28.6	-16.5				295	7.8	7.2	3.03
122	1440-1-1-Cast7	CZ	Cst	Prim	L2a	LV	-67.6	-28.6	-14.5				293	7.1	6.6	2.78
123	1440-1-1-Cast8	CZ	Cst	Prim	L2a	LV	-73.5	-33.3	-13.5				299	4.2	7.9	2.58
124	1440-1-1-Cast9	CZ	Cst	Prim	L2a	LV	-68.8	-32.2	-16.3				282	4.8	9.0	2.94
125	1440-1-1-Cast10	CZ	Cst	Prim	L2a	LV	-69.6	-30.1	-16.8				298	6.6	8.1	3.05
126	1440-1-1-Cast11	CZ	Cst	Prim	L2a	LV	-70.1	-30.2	-15.4				294	6.1	7.7	2.87
127	1440-1-1-Cast12	CZ	Cst	Prim	L2a	LV	-70.4	-31.0	-13.3				293	5.2	7.3	2.60
128	1440-1-1-Cast13	CZ	Cst	Prim	L2a	LV	-71.5	-29.2	-15.6				286	6.7	7.3	2.88
129	1440-1-1-Cast14	CZ	Cst	Prim	L2a	LV	-67.6	-30.1	-15.5				304	6.2	7.6	2.86
130	1440-1-1-Cast15	CZ	Cst	Prim	L2a	LV	-70.5	-32.1	-13.8				298	4.8	7.8	2.66
131	1440-1-1-Cast16	CZ	Cst	Prim	L2a	LV	-70.6	-32.5	-15.6				287	4.9	8.4	2.83
132	1440-1-1-Cast17	CZ	Cst	Prim	L2a	LV	-70.6	-33.7	-14.5				297	4.2	8.4	2.70
133	1440-1-1-Cast18	CZ	Cst	Prim	L2a	LV	-71.6	-31.9	-13.4				292	4.7	7.6	2.58
134	1440-1-2-A-2-1	CZ	Amb-Mon	Prim	L2a	SLV	-70.8	-33.3	-17.7				299	5.0	9.3	3.05
135	1440-1-2-A-2-2	CZ	Amb-Mon	Prim	L2a	SLV	-67.7	-36.9	-22.4				290	4.1	11.9	3.50
136	1440-1-2-A-2-3	CZ	Amb-Mon	Prim	L2a	LV	-72.9	-31.5	-18.9				294	6.2	9.3	3.25
137	1440-1-2-A-3-1	CZ	Amb-Mon	Prim	L2a	LV	-72.5	-32.4	-20.8				288	5.9	10.2	3.42
138	1440-1-2-A-3-2	CZ	Amb-Mon	Prim	L2a	LV	-66.9	-32.3	-18.1				284	5.5	9.2	3.12
139	1440-1-2-A-3-3	CZ	Amb-Mon	Prim	L2a	LV	-72.3	-35.7	-19.9				293	4.2	10.9	3.29
140	1440-1-2-A-3-4	CZ	Amb-Mon	Prim	L2a	LV	-70.3	-36.6	-21.0				285	4.1	11.3	3.37
141	1440-1-2-A-3-5	CZ	Amb-Mon	Prim	L2a	LV	-68.5	-36.1	-22.5				289	4.4	11.7	3.51
142	1440-1-2-A-3-6	CZ	Amb-Mon	Prim	L2a	SLV	-72.5	-29.5	-19.5				294	7.6	8.6	3.33
143	1440-1-2-A-3-7	CZ	Amb-Mon	Prim	L2a	LV	-68.1	-33.2	-22.1				293	5.7	10.7	3.50
144	1440-1-2-A-3-8	CZ	Amb-Mon	Prim	L2a	LV	-69.0	-29.1	-22.3				286	8.4	9.2	3.62
145	1440-1-2-A-3-9	CZ	Amb-Mon	Prim	L2a	LV	-70.3	-31.3	-21.0				292	6.7	9.7	3.44
146	1440-1-2-A-3-10	CZ	Amb-Mon	Prim	L2a	LV	-71.3	-29.4	-21.9				292	8.1	9.2	3.56
147	1440-1-2-A-4-1	CZ	Amb-Mon	Prim	L2a	LV	-70.9	-30.5	-18.5				296	6.6	8.7	3.19
148	1440-1-2-A-4-2	CZ	Amb-Mon	Prim	L2a	LV	-72.4	-31.7	-18.2				296	5.8	9.1	3.13
149	1440-1-2-A-4-3	CZ	Amb-Mon	Prim	L2a	LV	-71.3	-34.5	-19.4				293	4.7	10.4	3.25
150	1440-1-2-A-4-4	CZ	Amb-Mon	Prim	L2a	LV	-67.9	-33.7	-18.0				286	4.8	9.6	3.10
151	1440-1-2-A-4-5	CZ	Amb-Mon	Prim	L2a	LV	-64.4	-32.8	-18.6				296	5.4	9.5	3.17
152	1440-1-2-A-4-6	CZ	Amb-Mon	Prim	L2a	SLV	-71.4	-30.6	-21.0				292	7.2	9.4	3.45
153	1440-1-2-A-4-7	CZ	Amb-Mon	Prim	L2a	LV	-68.7	-34.5	-19.0				291	4.6	10.2	3.20
154	1440-1-2-A-4-8	CZ	Amb-Mon	Prim	L2a	LV	-67.9	-35.3	-21.4				286	4.6	11.2	3.43
155	1440-1-2-A-4-9	CZ	Amb-Mon	Prim	L2a	LV	-69.5	-35.2	-20.1				285	4.4	10.8	3.29
156	1440-2-2-2-1	CZ	Qz	Prim	L2b	LV	-56.0	-22.7	-17.3	-56.6	2.8	19.9	344	12.3	1.4	2.43
157	1440-2-2-2-2	CZ	Qz	Prim	L2b	SLV	-58.8	-20.7	-19.7	-57.6	2.8	19.1	346			
158	1440-2-2-2-3	CZ	Qz	Prim	L2b	LV	-59.3	-22.7	-17.3	-57.2	3.7	17.7	346	10.9	1.3	2.16
159	1440-2-2-2-4	CZ	Qz	Prim	L2b	LV	-60.1	-22.9	-16.8	-58.1	2.4	19.1	346	12.8	1.5	2.53
160	1440-2-2-2-5	CZ	Qz	Prim	L2b	LV	-58.8	-22.9	-17.9	-57.5	3.0	18.0	345	11.9	1.4	2.35
161	1440-2-2-2-6	CZ	Qz	Prim	L2b	LV	-59.9	-22.9	-19.2	-57.5	2.6	19.3	346	12.5	1.4	2.48
162	1440-2-2-2-7	CZ	Qz	Prim	L2b	LV	-59.8	-21.6	-17.9	-57.4	2.5	19.0	343	12.6	0.3	2.21
163	1440-2-2-2-8	CZ	Qz	Prim	L2b	LV	-59.1	-22.3	-16.9	-57.5	2.6	19.0	344	12.4	1.4	2.46
164	1440-2-2-2-9	CZ	Qz	Prim	L2b	LV	-59.3	-22.9	-16.1	-57.6	2.7	16.2	346	12.4	1.4	2.46
165	1440-2-2-2-10	CZ	Qz	Prim	L2b	LV	-59.7	-21.1	-17.5	-57.4	2.5	17.7	346			0.00
166	1440-2-2-2-11	CZ	Qz	Prim	L2b	LV	-59.2	-22.9	-17.8	-57.6	2.6	17.0	345	12.4	1.4	2.46
167	1440-2-2-2-12	CZ	Qz	Prim	L2b	LV	-59.5	-22.9	-16.8	-57.7	2.8	19.8	344	12.3	1.4	2.43
168	1440-2-2-2-13	CZ	Qz	Prim	L2b	LV	-59.4	-21.7	-16.7	-57.5	2.6	19.3	346	12.4	0.2	2.17
169	1440-2-2-2-14	CZ	Qz	Prim	L2b	LV	-59.9	-21.8	-16.9	-57.6	2.6	19.1	342	12.5	0.2	2.18
170	1440-2-2-2-15	CZ	Qz	Prim	L2b	LV	-59.4	-22.7	-17.6	-57.6	2.6	19.1	346	12.4	1.4	2.47
171	1440-2-2-2-16	CZ	Qz	Prim	L2b	LV	-59.3	-22.9	-19.1	-57.6	2.8	19.1	345	12.3	1.4	2.43
172	1440-2-2-2-17	CZ	Qz	Prim	L2b	SLV	-59.4	-22.9	-17.1	-57.6	2.6	19.3	345	12.4	0.2	2.17
173	1440-2-2-2-18	CZ	Qz	Prim	L2b	LV	-59.5	-21.9	-19.7	-57.6	2.6	20.0	345	12.4	0.6	2.26
174	1440-2-2-3-b-1	CZ	Qz	Prim	L2b	LV	-59.4	-21.6	-15.3	-57.9	2.3	19.7	344			
175	1440-2-2-3-b-2	CZ	Qz	Prim	L2b	LV	-60.0	-21.6	-17.5	-57.8	2.4	17.1	346			

176	1440-2-2-3-b-3	CZ	Qz	Prim	L2b	LV	-59.9	-22.2	-18.0	-57.5	2.3	18.3	346	12.4		0.8	2.31
177	1440-2-2-3-b-4	CZ	Qz	Prim	L2b	LV	-59.3	-22.3	-17.6	-57.7	2.2	18.7	345	12.4		0.8	2.31
178	1440-2-2-3-b-5	CZ	Qz	Prim	L2b	LV	-59.6	-22.1	-18.4	-57.6	2.6	19.4	344	12.4		0.9	2.32
179	1440-2-2-3-b-6	CZ	Qz	Prim	L2b	LV	-59.4	-21.9	-17.4	-57.3	2.6	18.8	346	12.4		0.2	2.17
180	1440-2-2-3-b-7	CZ	Qz	Prim	L2b	LV	-60.4	-22.9	-17.2	-57.6	3.0	19.7	342	12.4		1.4	2.45
181	1440-2-2-3-b-8	CZ	Qz	Prim	L2b	LV	-59.5	-20.7	-18.7	-57.9	3.4	19.6	346				
182	1440-2-2-3-b-9	CZ	Qz	Prim	L2b	LV	-59.5	-22.9	-18.1	-57.6	3.0	19.1	345	12.4		1.4	2.45
183	1023-gr-1-1	Greis RZ	Qz	Prim	L3a	LV	-34.6	-28.2	-15.6	-56.6	0.5	12.8	305	15.0	0.0		2.58
184	1023-gr-1-2	Greis RZ	Qz	Prim	L3a	LV	-30.2		-16.2	-56.6	0.4	13.0	291	15.2	0.0		2.60
185	1023-gr-1-3	Greis RZ	Qz	Prim	L3a	LV	-31.3		-17.0	-56.6	0.3	14.0	279	15.3	0.0		2.62
186	1023-gr-1-4	Greis RZ	Qz	Prim	L3a	LV	-34.2		-17.8	-56.6	0.2	13.7	257	15.4	0.0		2.63
187	1023-gr-1-5	Greis RZ	Qz	Prim	L3a	LV	-32.1		-19.5	-56.6	0.2	13.7	303	15.4	0.0		2.64
188	1023-gr-1-6	Greis RZ	Qz	Prim	L3a	LV	-33.6		-19.7	-56.6	0.3	13.6	287	15.3	0.0		2.62
189	1023-gr-1-7	Greis RZ	Qz	Prim	L3a	LV	-33.6	-26.4	-17.8	-56.6	0.5	14.0	295	15.1	0.0		2.58
190	1023-gr-1-8	Greis RZ	Qz	Prim	L3a	LV	-32.6		-15.9	-56.6	0.4	12.6	296	15.1	0.0		2.59
191	1023-gr-1-9	Greis RZ	Qz	Prim	L3a	LV	-32.7		-18.5	-56.6	0.3	12.7	270	15.3	0.0		2.62
192	1023-gr-1-10	Greis RZ	Qz	Prim	L3a	LV	-37.7		-17.0	-56.6	0.4	13.5	290	15.2	0.0		2.60
193	1023-gr-1-11	Greis RZ	Qz	Prim	L3a	LV	-34.7		-17.7	-56.6	0.2	13.7	270	15.3	0.0		2.63
194	1023-gr-1-12	Greis RZ	Qz	Prim	L3a	LV	-30.8		-18.7	-56.6	0.4	13.0	302	15.1	0.0		2.59
195	1023-gr-1-13	Greis RZ	Qz	Prim	L3a	L2V	-29.8		-19.1	-57.3	0.6	13.6	282	14.9	0.0		2.55
196	1023-gr-2-14	Greis RZ	Qz	Prim	L3a	L2V	-33.7		-16.0	-57.2	0.4	13.8	284	15.1	0.0		2.59
197	1023-gr-2-15	Greis RZ	Qz	Prim	L3a	L2V	-31.9		-15.4	-57.2	0.2	13.2	281	15.3	0.0		2.63
198	1023-gr-2-16	Greis RZ	Qz	Prim	L3a	L2V	-31.1		-19.5	-57.2	0.4	14.1	272	15.1	0.0		2.59
199	1023-gr-2-17	Greis RZ	Qz	Prim	L3a	L2V	-34.7	-25.4	-17.3	-57.2	0.5	13.8	284	15.0	0.0		2.57
200	1023-gr-2-18	Greis RZ	Qz	Prim	L3a	L2V	-31.7	-26.4	-17.6	-57.3	0.4	13.4	284	15.2	0.0		2.60
201	1023-gr-2-19	Greis RZ	Qz	Prim	L3a	LV	-31.7		-18.2	-57.1	0.4	13.3	272	15.1	0.0		2.59
202	1023-gr-2-20	Greis RZ	Qz	Prim	L3a	LV	-31.7		-16.3	-57.1	0.5	13.4	270	15.0	0.0		2.58
203	1023-gr-2-21	Greis RZ	Qz	Prim	L3a	LV	-32.0		-19.8	-57.2	0.3	13.4	289	15.2	0.0		2.61
204	1023-gr-2-22	Greis RZ	Qz	Prim	L3a	LV	-32.7		-17.3	-57.2	0.3	14.0	274	15.3	0.0		2.62
205	1023-gr-2-23	Greis RZ	Qz	Prim	L3a	LV	-33.1		-17.0	-57.3	0.3	13.6	283	15.3	0.0		2.62
206	1023-gr-2-24	Greis RZ	Qz	Prim	L3a	LV	-31.7		-17.8	-57.3	0.3	13.3	274	15.2	0.0		2.61
207	1023-gr-2-25	Greis RZ	Qz	Prim	L3a	LV	-31.4		-17.4	-57.8	0.6	13.7	291	14.9	0.0		2.55
208	1023-gr-2-26	Greis RZ	Qz	Prim	L3a	LV	-31.4		-20.1	-57.6	0.4	13.5	278	15.1	0.0		2.59
209	1023-gr-2-27	Greis RZ	Qz	Prim	L3a	LV	-32.9		-18.1	-57.5	0.4	13.8	272	15.1	0.0		2.59
210	1023-gr-2-28	Greis RZ	Qz	Prim	L3a	LV	-32.8		-17.9	-57.8	0.5	13.3	299	15.1	0.0		2.58
211	1023-gr-3-1	Greis RZ	Cst	Prim	L3b	LV	-22.4		-11.1		-3.1		279	15.0	0.0		2.58
212	1023-gr-3-2	Greis RZ	Cst	Prim	L3b	LV	-22.3		-10.0				278	14.0	0.0		2.39
213	1023-gr-3-3	Greis RZ	Cst	Prim	L3b	LV	-22.2		-10.6				306	14.5	0.0		2.49
214	1023-gr-3-4	Greis RZ	Cst	Prim	L3b	LV	-22.4		-10.4				305	14.3	0.0		2.46
215	1023-gr-3-5	Greis RZ	Cst	Prim	L3b	LV	-22.0		-11.0				294	15.0	0.0		2.57
216	1023-gr-3-6	Greis RZ	Cst	Prim	L3b	LV	-22.3		-10.4		-4.7		267	14.4	0.0		2.46
217	1023-gr-4-7	Greis RZ	Cst	Prim	L3b	LV	-22.7		-9.9				273	13.8	0.0		2.37
218	1023-gr-4-8	Greis RZ	Cst	Prim	L3b	LV	-21.6		-10.6				261	14.6	0.0		2.49
219	1023-gr-4-9	Greis RZ	Cst	Prim	L3b	LV	-22.7		-10.3				296	14.2	0.0		2.43
220	1023-gr-4-10	Greis RZ	Cst	Prim	L3b	LV	-20.7		-10.0				349	14.0	0.0		2.39
221	1023-gr-4-11	Greis RZ	Cst	Prim	L3b	LV	-20.2		-10.4				294	14.4	0.0		2.46
222	1023-gr-4-12	Greis RZ	Cst	Prim	L3b	LV	-21.8		-9.8				303	13.7	0.0		2.34
223	1023-gr-4-13	Greis RZ	Cst	Prim	L3b	LV	-21.9		-10.4				280	14.4	0.0		2.46
224	1023-gr-4-14	Greis RZ	Cst	Prim	L3b	LV	-24.3		-10.2				279	14.1	0.0		2.42
225	1023-gr-4-15	Greis RZ	Cst	Prim	L3b	LV	-20.4		-10.5		-3.8		275	14.5	0.0		2.48
226	1023-gr-5-16	Greis RZ	Cst	Prim	L3b	LV	-19.5		-10.2				284	14.1	0.0		2.42
227	1023-gr-5-17	Greis RZ	Cst	Prim	L3b	LV	-22.8		-9.8				289	13.7	0.0		2.34
228	1023-gr-5-18	Greis RZ	Cst	Prim	L3b	LV	-20.9		-10.1				287	14.1	0.0		2.41
229	1023-gr-5-19	Greis RZ	Cst	Prim	L3b	LV	-22.5		-10.3		-3.1		254	14.3	0.0		2.44
230	1023-gr-5-20	Greis RZ	Cst	Prim	L3b	LV	-21.2		-10.8		-2.4		286	14.8	0.0		2.53
231	1023-gr-5-21	Greis RZ	Cst	Prim	L3b	LV	-22.4		-10.4		-2.1		284	14.4	0.0		2.46

WZ: wall zone, IZ: intermediate zone, CZ: core zone, RZ: replacement zone, cleav: cleavelandite, greis: greisen.

1075 Cst: cassiterite; Mon: montebrasite; Qz: quartz L: liquid; S: solid; V: vapour

C. Fluid inclusion LA-ICP-MS analyses

Table C. Results of the LA-ICP-MS analyses of individual fluid inclusions (elemental concentrations in ppm).

Sample	Name	Spotsize (µm)	Li	Na	Mg	P	K	Mn	Fe	Rb	Sr	Nb	Sn	Cs	Ba	Ta	W
1	1702-3-H-B-12	40	443	71755	365	520	22478	313	1052	1691	52	1.1	14	272	84	1.8	7.1
3	1702-3-H-B-10A	30	4261	36256	51178	23167	61347	859	<7217	1467	243	26	252	146	501	54	<4.2
4	1702-3-H-B-15	30	717	70382	152	1184	23249	7423	10814	1502	63	3.8	104	166	160	1.4	0.7
5	1702-3-H-B-16	40	645	82206	2214	1434	13696	246	<329	1197	51	0.9	32	259	53	1.4	0.3
6	1702-3-H-B-14	30	1526	68317	25900	5204	16206	1200	3020	2187	86	2.1	51	169	148	5.2	5.8
7	1702-3-H-B-9	30	5917	42074	6018	18184	37610	2518	<5886	620	391	26	199	195	1953	41	9.4
11	1702-3-H-B-4	30	3830	46305	2368	5032	35076	489	4479	1713	100	63	108	100	307	252	832
16	1702-3-H-B-21	30	17228	23727	7782	11317	14468	1722	3202	392	367	6.6	164	45	3271	16	2921
17	1702-3-H-A-11	30	520	65072	372	2564	40664	17365	10784	1977	162	13	175	189	412	2.1	8.0
22	1702-3-H-A-20	30	2558	57115	16478	9939	43158	2699	13268	1053	471	28	119	123	780	25	57.4
23	1702-3-H-A-20A	30	555	81495	<46	<5190	12936	3504	<3201	1107	62	<1.2	<46	180	46	<0.5	<2.5
25	1702-3-H-A-15	30	1932	35995	7377	7737	62837	40935	21908	2708	377	36	399	142	943	21	12.1
26	1702-3-H-A-24	30	288	75540	20	<1244	5880	4397	<799	459	649	<0.2	12.1	115	222	<0.1	<0.4
28	1702-3-H-A-10	30	762	81966	1818	1186	11080	217	3256	801	579	0.5	8.1	275	411	11.7	0.9
29	1702-3-H-A-27	30	3233	44334	10779	17692	48725	262	6582	1486	218	309	493	89	329	40	24
30	1702-3-H-A-28	30	507	78364	<11	<1283	6675	1551	<864.583	459	21	<0.3	<10	103	14	<0.1	<0.6
32	1702-3-H2-C-5	30	1243	84599	1206	7621	5555	6147	2257	790	169	5	78	96	320	1.7	368
33	1702-3-H2-C-7	30	379	84848	2048	4970	10029	1575	<2200	624	283	55	47	252	149	9.9	260
35	1702-3-I2-B-18	30	2802	67914	7352	2866	6905	147	835	584	163	9	19	110	35	8.4	<0.4
36	1702-3-I2-B-7	40	388	74543	71	360	9056	14	53	954	46	0.3	3.8	130	15	0.4	105
37	1702-3-I2-B-20	30	851	73937	6214	2557	7562	<30	<1032	797	38	<0.3	22	96	13	0.3	<0.6
38	1702-3-I2-B-21	30	211	74499	4	425	10265	787	357	692	36	0.1	<3	82	27	0.0	<0.1
39	1702-3-I2-B-4	30	446	74571	31	161	8818	120	104	678	50	0.2	1.3	93	11	0.4	0.5
40	1702-3-I2-B-22	30	1174	67117	15434	3377	17229	46	1085	1016	64	6.8	36	140	54	10	12
41	1702-3-I2-B-23	30	1585	70904	3333	1803	8589	1099	1047	776	141	4.3	13	115	28	3.8	2.3
42	1702-3-I2-A-3	30	1826	65834	59426	34567	20026	352	13850	205	2917	80	182	<11	1761	60	<8
43	1702-3-I2-A-4	30	1017	72953	553	2926	8396	84	1320	482	504	6.5	<16	261	46	7.6	0.6
44	1702-3-I2-A-5	30	1672	50912	49851	33170	46311	503	20989	390	1296	72	299	49	391	36	11
45	1702-3-I2-A-7	30	4351	42230	88265	51065	45138	7817	<10125	1523	230	46	1087	707	636	189	54
46	1702-3-I2-A-12	30	3854	57514	15223	22433	36138	2290	10952	192	270	50	291	<6	204	208	<4
47	1702-3-I2-D-1	30	1198	94477	107	<170	3830	9	<116	741	34	<0.03	1.4	503	19	<0.1	1.1
48	1702-3-I2-D-2	30	1435	93015	50	<285	4755	360	<196	1001	20	<0.06	<2.3	861	6	<0.1	1.8
49	1702-3-I2-D-3	30	2149	66848	8727	2433	28185	4814	11221	3339	109	29	40	621	53	0.2	6.1
50	1702-3-I2-D-4	40	986	75765	<6	<834	6709	75	<479	1219	13	<0.2	<6	334	<1.0	<0.1	0.6
51	1702-3-I2-D-5	30	1248	81177	2798	313	10181	216	199	1119	42	<0.05	12.0	581	25	0.0	3.4
52	1702-3-I2-D-6	30	3552	62964	526	<126	7470	848	386	1272	18	<0.03	<1.0	911	16	0.0	22
53	1702-3-I2-D-7	30	2419	68011	351	196	5425	4	102	1054	18	0.0	1.7	731	22	0.1	15
55	1037-2-Cst-2	40	1329	68968	2381	<253	30279	<LODmix	<LODmix	722	13	<LODmix	<LODmix	259	167	<LODmix	<LODmix
56	1037-2-Cst-3	40	1108	63971	<1254	<63	13493	<LODmix	<LODmix	962	91	<LODmix	<LODmix	324	114	<LODmix	<LODmix
57	1037-2-Cst-4	40	1445	71955	2448	<254	11254	<LODmix	<LODmix	679	340	<LODmix	<LODmix	229	48	<LODmix	<LODmix
58	1037-2-Cst-5	40	1534	74592	1403	<98	15744	<LODmix	<LODmix	563	<230	<LODmix	<LODmix	354	143	<LODmix	<LODmix
59	1037-2-Cst-6	40	1308	56580	26792	<125	14523	<LODmix	<LODmix	1634	124	<LODmix	<LODmix	449	361	<LODmix	<LODmix
60	1037-2-Cst-7	40	2118	60552	8523	<47	35128	<LODmix	<LODmix	813	65	<LODmix	<LODmix	345	89	<LODmix	<LODmix
61	1037-2-Cst-8	40	2943	52921	7423	<88	33541	<LODmix	<LODmix	1408	120	<LODmix	<LODmix	480	140	<LODmix	<LODmix
68	1449-2-1-C-1	40	1604	71561	<7	<995	4991	100	<630	543	25	<0.2	<10	355	6	<0.08	<0.5
69	1449-2-1-C-2	40	1878	57349	2137	4708	27933	108	15070	60	227	<1.1	48	32	294	<0.3	12
76	1449-2-1-C-9	40	<81	66822	4884	7936	25976	134	<4100	28	196	5.6	2883	<4.6	661	5.3	23
79	1449-2-1-B-2	40	1979	26689	4746	283	63797	185	5950	3159	1	7.6	67	183	5	5.7	7.5
116	1440-1-1-Cast1	40	12098	21440	<1	<58	<11	<LODmix	<LODmix	3025	<0.1	<LODmix	<LODmix	<0.2	<2	<LODmix	<LODmix
120	1440-1-1-Cast5	40	11528	23590	<16	<1558	4328	<LODmix	<LODmix	2376	<0.9867	<LODmix	<LODmix	1204	<23	<LODmix	<LODmix
121	1440-1-1-Cast6	40	12098	21440	<3	<70	43270	<LODmix	<LODmix	545	<0.0748	<LODmix	<LODmix	2412	<2.1	<LODmix	<LODmix
122	1440-1-1-Cast7	40	12098	21440	<3	<585	76385	<LODmix	<LODmix	3030	80	<LODmix	<LODmix	3605	<5.3	<LODmix	<LODmix
135	1440-1-2-A-2-2	40	19417	16224	1650	<LODmix	5202	316	9749	1084	172	103	1246	1627	54	<0.2	1.3
136	1440-1-2-A-2-3	40	15197	24294	2905	<LODmix	3336	1077	7656	308	127	189	2132	867	277	49	14
148	1440-1-2-A-4-2	40	14829	22895	1969	<LODmix	2482	294	3662	25	499	116	1986	87	1006	<0.7	4.2
150	1440-1-2-A-4-4	40	15786	19068	2143	<LODmix	6041	176	2749	9	45	23	1321	16	112	380	3.6
152	1440-1-2-A-4-6	40	14077	29864	1643	<LODmix	15479	87	3020	93	29	88	236	89	275	131	17
156	1440-2-2-2-1	30	3993	34254	143	<148	913	11	1238	317	3	<0.02	<1.9	496	2	0.1	0.4
157	1440-2-2-2-2	40	2674	37575	106	<46	2608	11	845	553	5	<0.02	<0.44	443	1	0.3	1.2
158	1440-2-2-2-3	40	1899	35196	87	<54	2160	3	642	383	4	0.0	0.6	337	0	0.2	0.7
159	1440-2-2-2-4	40	6243	28621	227	<126	1159	12	1730	513	2	<0.03	2.0	660	1	0.3	0.3
160	1440-2-2-2-5	40	4029	32203	208	<72	1544	14	1440	362	2	0.1	1.1	593	1	0.8	0.4
161	1440-2-2-2-6	40	6460	28005	244	169	1037	14	1787	448	2	<0.04	3.1	588	1	0.3	0.7
174	1440-2-2-3-b-1	40	2653	37845	80	36	2872	12	633	598	5	0.1	0.6	583	1	0.1	1.2
175	1440-2-2-3-b-2	40	3979	34390	146	<110	1330	10	1208	403	4	0.1	1.6	713	5	0.2	0.4
176	1440-2-2-3-b-3	40	4821	31270	168	<83	1830	20	1373	504	2	0.1	<0.7	757	1	0.1	0.4
177	1440-2-2-3-b-4	40	4882	31774	152	63	716	81	1400	357	15	0.3	1.9	696	6	0.3	3.5
178	1440-2-2-3-b-5	40	3470	34459	126	<92	3882	26	1008	833	6	0.0	<0.8	720	2	0.1	0.4
179	1440-2-2-3-b-6	40	5185	29838	173	<210	2158	29	1631	581	3	<0.04	<2.1	833	3	0.1	0.5
180	1440-2-2-3-b-7	40	4270	33659	111	<57	912	31	882	552	12	0.0	0.9	559	4	0.3	0.1
184	1023-gr-1-2	30	1656	27779	4274	10735	44894	402	15338	500	158	455	332	8	211	477	7.2
185	1023-gr-1-3	30	1704	46065	940	1401	14324	237	1976	427	40	55	3668	122	42	126	0.6
186	1023-gr-1-4	30	1863	39418	1040	8163	24680	1739	4757	753	39	124	9397	483	72	148	3.0
187	1023-gr-1-5	30	2957	22473	2344	8280	47547	1546	10073	1287	249	317	266	73	184	379	5.9
211	1023-gr-3-1	30	1906	57078	297	<576	105	<LODmix	<LODmix	38	<33	<LODmix	<LODmix	270	1483	<LODmix	<LODmix
212	1023-gr-3-2	30	343	57078	3197	<1817	105	<LODmix	<LODmix	42	19	<LODmix	<LODmix	796	4752	<LODmix	<LODmix
213	1023-gr-3-3	30	184	57078	<30	<325	105	<LODmix	<LODmix	356	440	<LODmix	<LODmix	3027	13772	<LODmix	<LODmix
214	1023-gr-3-4	30	124	57078	<22	<2452	<410	<LODmix	<LODmix	195	154	<LODmix	<LODmix	1110	1446	<LODmix	<LODmix
217	1023-gr-4-7	30	578	57078	3711	<3631	<609	<LODmix	<LODmix	140	345	<LODmix	<LODmix	441	14598	<LODmix	<LODmix
218	1023-gr-4-8	30	31	57078	774	<6279	105	<LODmix	<LODmix	99	32	<LODmix	<LODmix	366	20160	<LODmix	<LODmix
226	1023-gr-5-16	30	3105	57078	13235	<9245	105	<LODmix	<LODmix	724	162	<LODmix	<LODmix	4580	24997	<LODmix	<LODmix
227	1023-gr-5-17	30	674	57078	11084	<2000	105	<LODmix	<LODmix	7	55	<LODmix	<LODmix	79	543	<LODmix	<LODmix

<: below specified detection limit

<LODmix: below specified detection limit of host-inclusion mixture

Tables

Table 1. Summary of microthermometric analyses of fluid inclusions.

Type	Phases	System	n	Zone	Host	Size (µm)*	Fill rate (%)*	Solids	T_{fm}* (°C)	$T_{m,hh}$* (°C)	$T_{m,ice}$* (°C)	$T_{m,CO2}$* (°C)	$T_{m,clath}$* (°C)	$Th_{,CO2}$* (°C)	$T_{h,tot}$* (°C)	N_2 *(mol%)	NaCl wt.%**	LiCl wt.%**	KCl wt.%**	Salinities
L1a	$S_{(2)}LV$	H_2O-NaCl-KCl-(CO_2, N_2)	59	WZ + IZ	Qz	10;60;23	5;32;16	paragonite, siderite, rhodocrosite, kutnohorite	-28.7;-23.4; -26.1	-22.9;-4.1; -20.3	-22.9;-15.2; -20.0	/	3.2;4.2;3.7 (n=4)	/	249;359;264	5;19;13	21.5 ± 1.6	/	3.6 ± 1.4	[3]
L1b	LV	H_2O-NaCl-KCl-(CO_2,N_2)	56	WZ + IZ	Qz + Cst1	6;48;25	6;48;18	/	-28.1;-23.3; -25.9	-22.8;-2.3; -17.1	-22.9;-13.8; -19.4	/	-4.7;2.6;-0.9 (n=16)	/	315;389;356	3;17;12	19.7 ± 1.8	/	2.0 ± 1.7	[3]
L2a	(S)LV	H_2O-NaCl-LiCl	40	CZ	Mon + Cst2	6;130;25	4;55;16	Li-mica	-79.5;-64.4; -70.1	-36.6;-28.6; -31.9	-22.5;-13.3; -17.8	/	/	/	289;304;301	/	5.5 ± 1.3	9.8 ± 1.1	/	[1]
L2b	$(S)L_2V$	H_2O-NaCl-LiCl-CO_2-N_2	27	CZ	Qz	12;54;22	17;27;22	Li-mica	-60.4;-56.0; -59.4	-22.9;-20.7; -22.2	-19.7;-15.3; -17.6	-58.1;-56.6; -57.6	2.2;3.7;2.7	16.2;20.0; 18.8 (to V)	282;304;292	5;14;7	12.3 ± 0.3	1.0 ± 0.5	/	[1] [2]
L3a	$L_{(2)}V$	H_2O-NaCl-(KCl)-CO_2-N_2	28	RZ greisen	Qz	9;31;15	12;15;13	/	-37.7;-29.8; -32.6	/	-20.1;-15.4; -17.7	-57.8;-56.6; -57.0	0.2;0.6;0.4	12.6;14.1; 13.5 (to V)	257;305;283	12;22;18	15.2 ± 0.1	/	<0.02	[2] [3]
L3b	LV	H_2O-NaCl-(KCl)-(CO_2,N_2)	21	RZ greisen	Cst3	11;50;24	8;15;10	/	-24.3;-19.5; -21.9	/	-11.1;-9.8; -10.3		-4.7;-2.1;-3.2 (n=6)	/	254;349;289	8;25;11	14.3 ± 0.4	/	<0.02	[3]

Values correspond to: *minimum; maximum; average **average ± standard deviation
[1] Dubois et al. (2010); [2] Bakker (1997): [3] Bodnar et al. (1989)
Cst: cassiterite; Mon: montebrasite; Qz: quartz L: liquid; S: solid; V: vapour

Figures

Figure 1. Geological maps. (A) Simplified geological map of the Karagwe-Ankole Belt with the location of the major Sn-Nb-Ta pegmatites, Sn quartz veins and W quartz veins in Rwanda (partly after Hulsbosch et al. 2019). (B) Geological map and cross-sections of the LCT-family, rare-element Gatumba dyke system (GDS) pegmatites and country rocks (partly after RMCA archive data of Minétain and Somirwa).

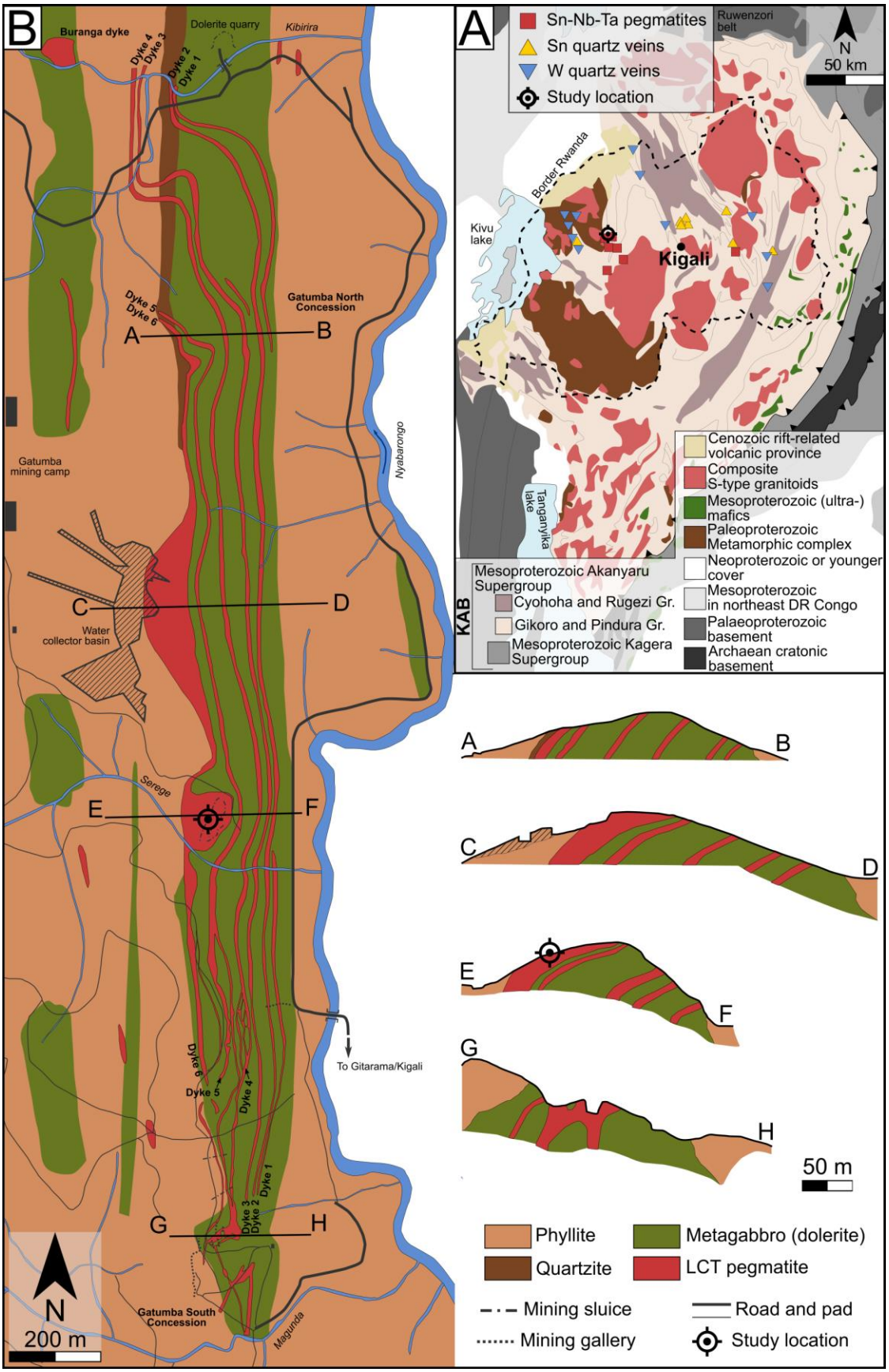
B
Buranga dyke
Dolerite quarry
Kibirira
Dyke 4
Dyke 3
Dyke 2
Dyke 1
Dyke 5
Dyke 6
Gatumba North Concession
A
B
Gatumba mining camp
Nyabarongo
C
D
Water collector basin
Serege
E
F
To Gitarama/Kigali
Dyke 6
Dyke 5
Dyke 4
Dyke 3
Dyke 2
Dyke 1
G
H
N
200 m
Gatumba South Concession
Magunda
A
Sn-Nb-Ta pegmatites
Sn quartz veins
W quartz veins
Study location
Ruwenzori belt
N
50 km
Border Rwanda
Kivu lake
Kigali
Tanganyika lake
KAB
Mesoproterozoic Akanyaru Supergroup
Cyohoha and Rugezi Gr.
Gikoro and Pindura Gr.
Mesoproterozoic Kagera Supergroup
Cenozoic rift-related volcanic province
Composite S-type granitoids
Mesoproterozoic (ultra-) mafics
Paleoproterozoic Metamorphic complex
Neoproterozoic or younger cover
Mesoproterozoic in northeast DR Congo
Palaeoproterozoic basement
Archaean cratonic basement
A
B
C
D
E
F
G
H
50 m
Phyllite
Metagabbro (dolerite)
Quartzite
LCT pegmatite
Mining sluice
Road and pad
Mining gallery
Study location

1091

Figure 2. Overview of field and sample photographs of dyke 6 of the GDS at the study location in the Serege valley. See section 4.1. for more details (A) Overview picture showing the pegmatite in the metagabbro country rock. Dyke width at metagabbro contact is 19 m. (B) Intrusive contact of dyke 6 with the metagabbro country rock and the development of the border and wall zone. (C) Formation of the border and wall zone with aplitic banding rich in tourmaline and apatite. (D) Intrusive contact of dyke 6 with the metagabbro country rock and the development of the border and wall zone. Both zones shown are microcline-rich and unaffected by albitisation or the formation of cleavelandite. Disseminated cassiterite phase Cst1 is hosted in the wall zone. (E) Microphotograph showing contacts between primary, disseminated cassiterite Cst1 and quartz, albite-oligoclase or mica which are generally defined by crystal faces. However, locally Cst1 seems to have been resorbed with the formation of embayment textures. (F) Spodumene, Li-mica and quartz rich unit in the intermediate zone. Microcline is completely altered to secondary cleavelandite. (G) Euhedral, unidirectional solidification texture between quartz and microcline. Microcline is partly affected by albitisation. (H) Primary columbite-tantalite mineralisation in the intermediate zone. The zone is intensely affected by albitisation forming secondary cleavelandite. (H) Large sample showing the transition towards and development of the core zone rich in phosphates, quartz and primary cassiterite Cst2 phase (red arrows). The latter is spatially associated with quartz. (J) and (K) showing examples of muscovite-quartz greisen pockets in the wall and intermediate zone and the development of secondary cassiterite Cst3 mineralisation.

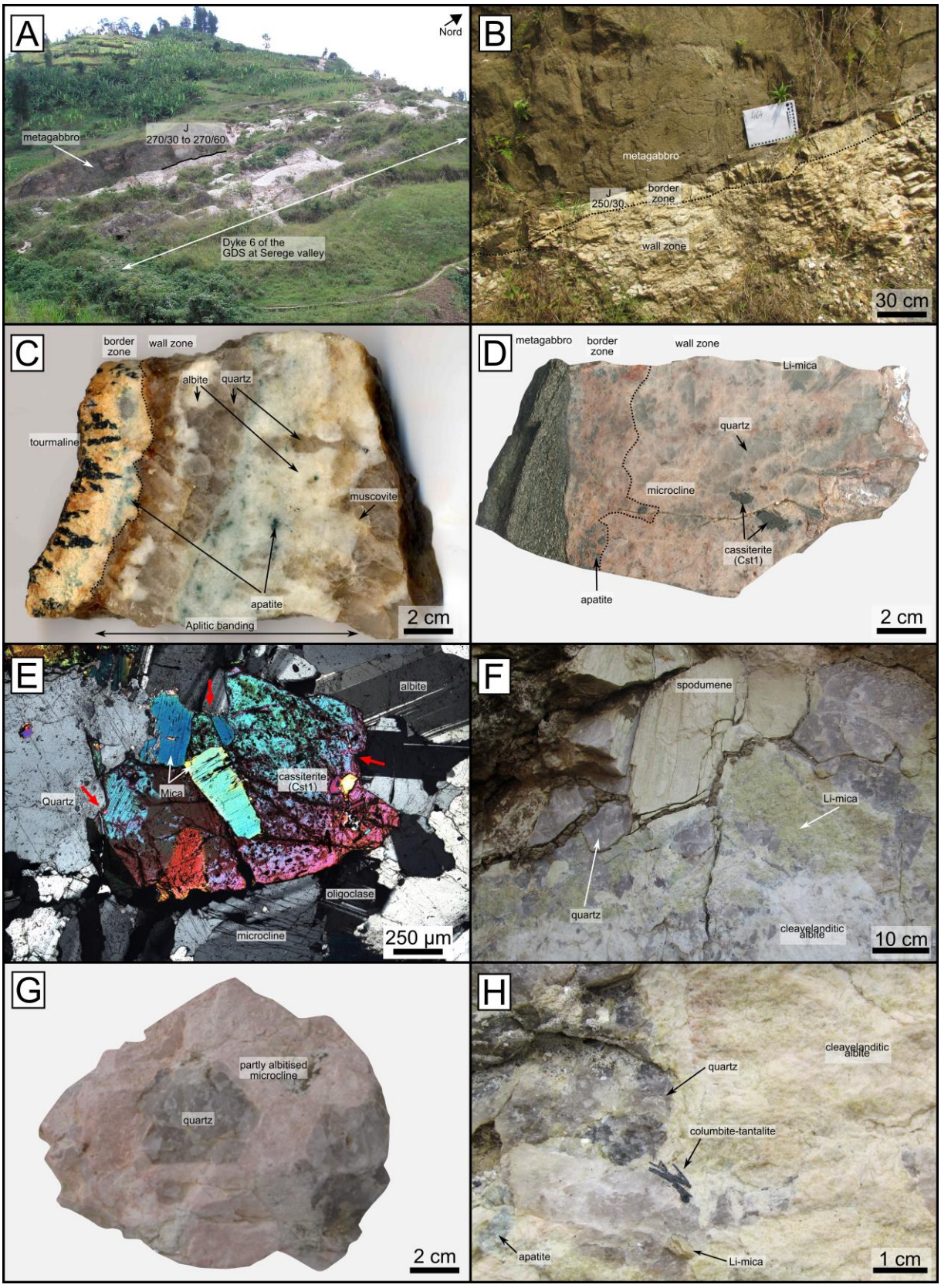
A
Nord
metagabbro
J
270/30 to 270/60
Dyke 6 of the
GDS at Serege valley
B
metagabbro
J
250/30
border
zone
wall zone
30 cm
C
border
zone
wall zone
albite
quartz
tourmaline
muscovite
apatite
Aplitic banding
2 cm
D
metagabbro
border
zone
wall zone
Li-mica
quartz
microcline
cassiterite
(Cst1)
apatite
2 cm
E
albite
Mica
cassiterite
(Cst1)
Quartz
oligoclase
microcline
250 µm
F
spodumene
Li-mica
quartz
cleavelanditic
albite
10 cm
G
partly albitised
microcline
quartz
2 cm
H
cleavelanditic
albite
quartz
columbite-tantalite
apatite
Li-mica
1 cm

1113

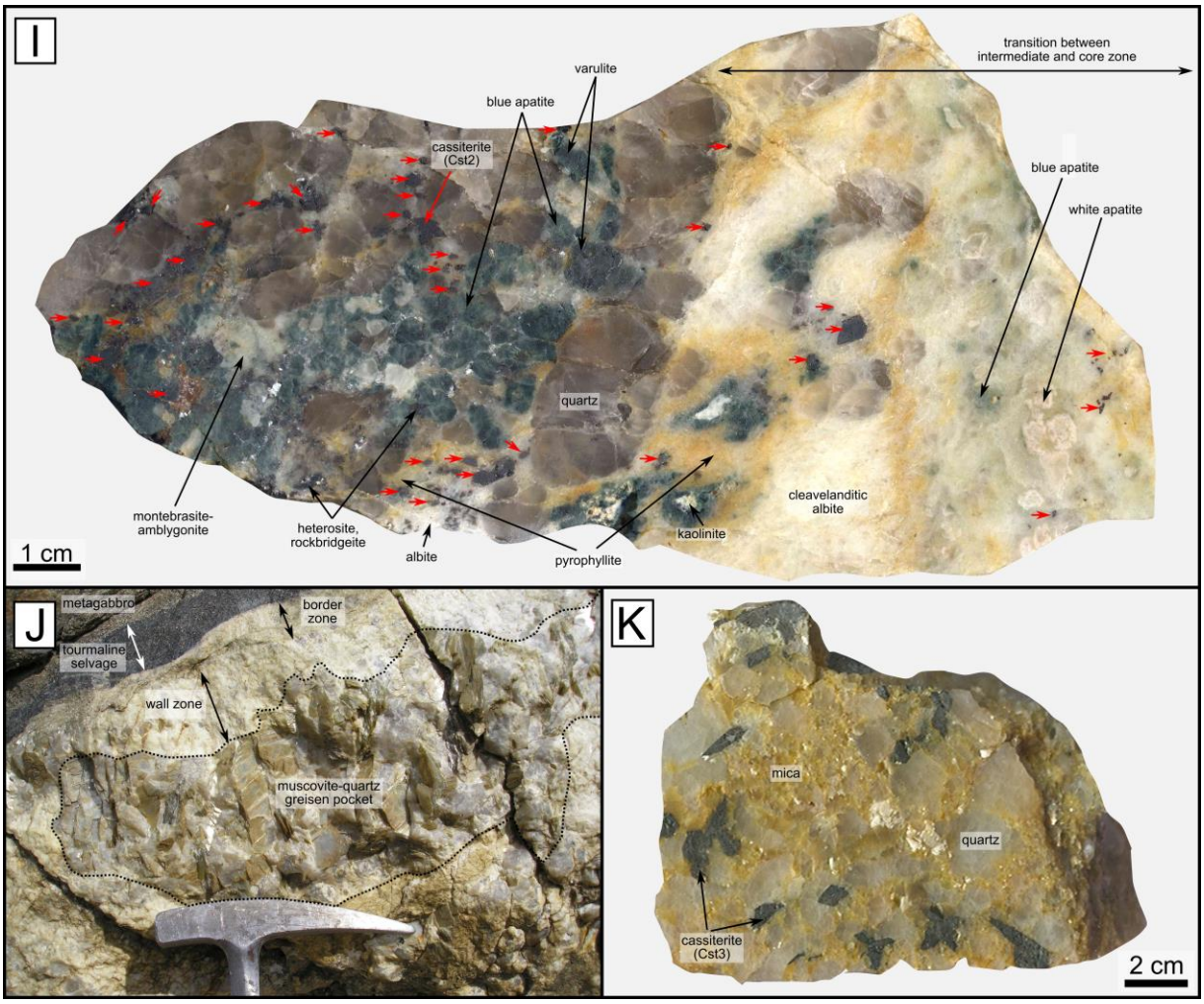
I
transition between intermediate and core zone
varulite
blue apatite
cassiterite (Cst2)
blue apatite
white apatite
quartz
montebrasite-amblygonite
heterosite, rockbridgeite
albite
pyrophyllite
kaolinite
cleavelanditic albite
1 cm
J
metagabbro
border zone
tourmaline selvage
wall zone
muscovite-quartz greisen pocket
K
mica
quartz
cassiterite (Cst3)
2 cm

1114

Figure 3. Schematic overview of the internal anatomy and mineralogy of the GDS with the development of border (BZ), wall (WZ), intermediate (IZ), core (CZ) and replacement (RZ) zones. The replacement zones consist of cleavelandite after microcline units and greisen pockets.

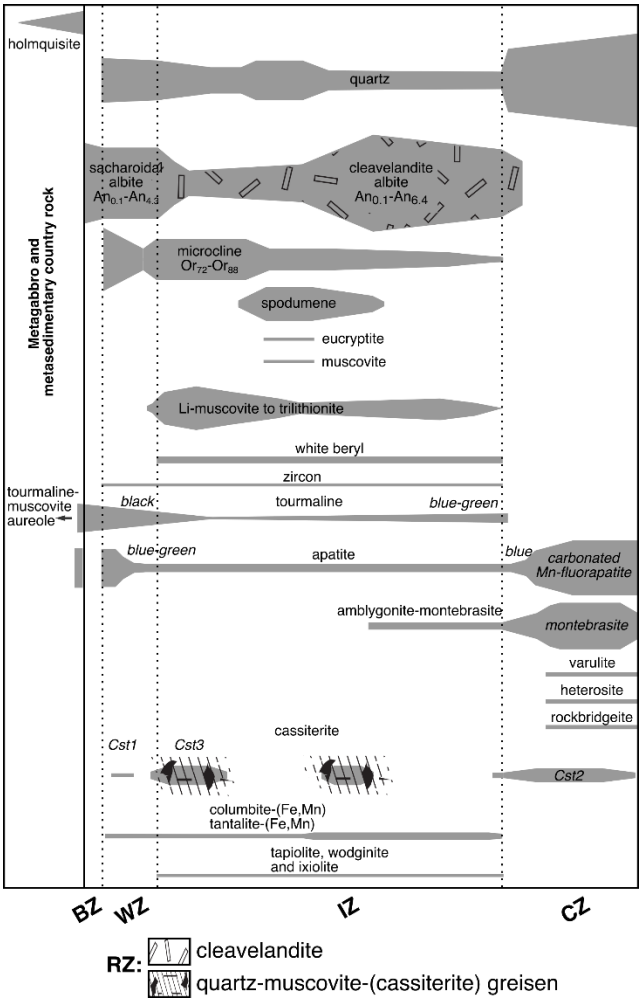

Figure 4. Representative Raman spectra of phosphate minerals. See text for discussion on peak assignments. (A) Spectrum of montebrasite in the core zone with indication of the indicative peaks (P1-P10) according to Rondeau et al. (2006). (B) Variation in position of the width of the 3360 cm^{-1} peak as a function of the fluorine content of montebrasite-amblygonite. A set of representative spectra of white and blue apatite in the core zone. The spectrum of blue apatite is complicated by additional peaks induced by the substitutions of carbonate, borate and manganese.

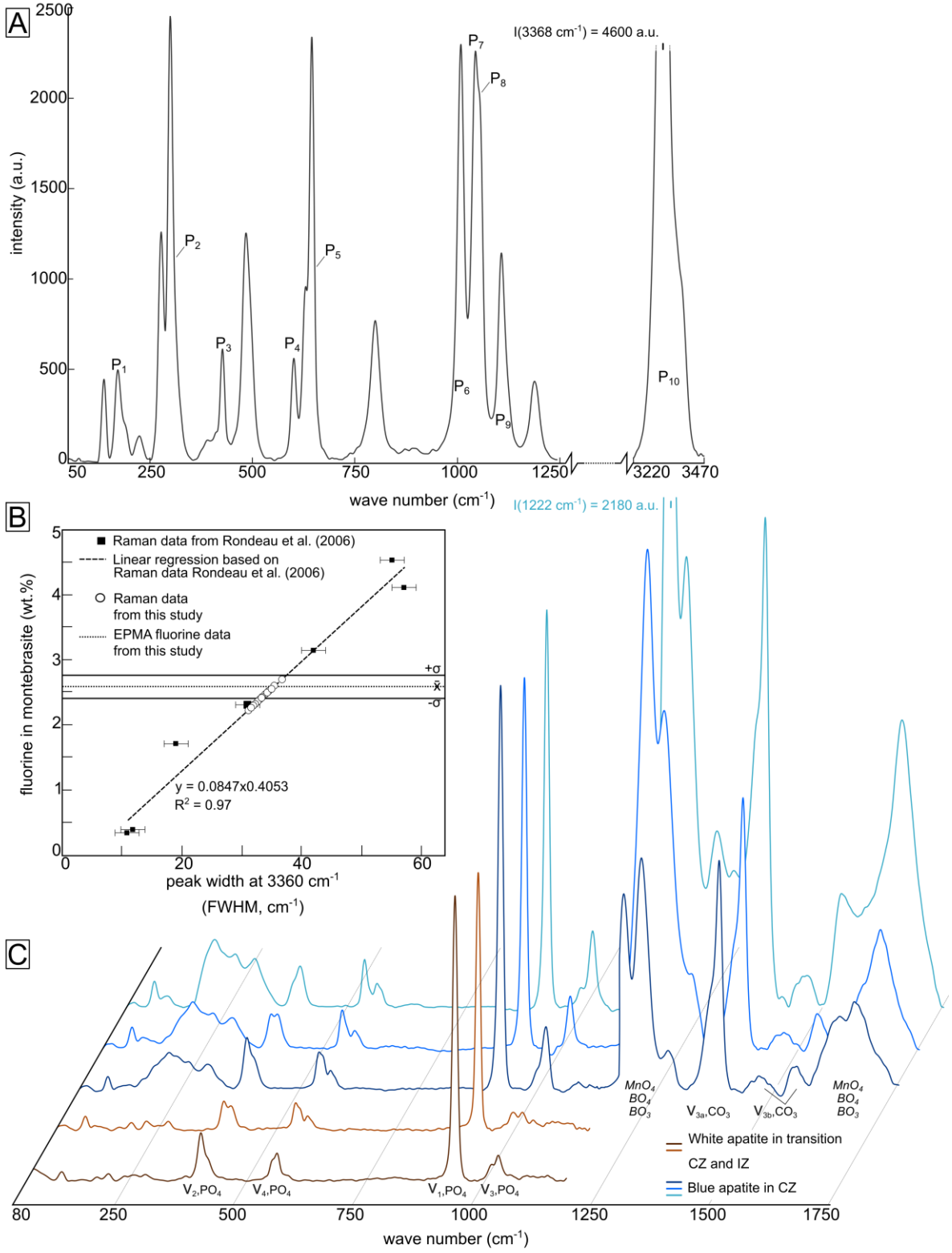
A
intensity (a.u.)
wave number (cm-1)
I(3368 cm-1) = 4600 a.u.
P1
P2
P3
P4
P5
P6
P7
P8
P9
P10
B
fluorine in montebrasite (wt.%)
peak width at 3360 cm-1
(FWHM, cm-1)
Raman data from Rondeau et al. (2006)
Linear regression based on Raman data Rondeau et al. (2006)
Raman data from this study
EPMA fluorine data from this study
+σ
x̄
-σ
y = 0.0847x0.4053
R2 = 0.97
I(1222 cm-1) = 2180 a.u.
C
V2,PO4
V4,PO4
V1,PO4
V3,PO4
MnO4 BO4 BO3
V3a,CO3
V3b,CO3
MnO4 BO4 BO3
White apatite in transition CZ and IZ
Blue apatite in CZ
wave number (cm-1)

1127

Figure 5. Representative Raman spectra of the three cassiterite phases. See text for discussion on peak assignments. (A) Spectra of primary, disseminated cassiterite, hosted in microcline, in the wall zone (Cst1, WZ) and of primary cassiterite, in assemblage with quartz and phosphates, in the core zone (Cst2, CZ). (B) Spectra of secondary cassiterite in quartz-muscovite greisen pockets in the wall and intermediate zone (Cst3). Cst3 hosts columbite-(Mn) inclusions and lamellae along growth zones for which one spectrum is depicted in combination with the reflected light microphotograph.

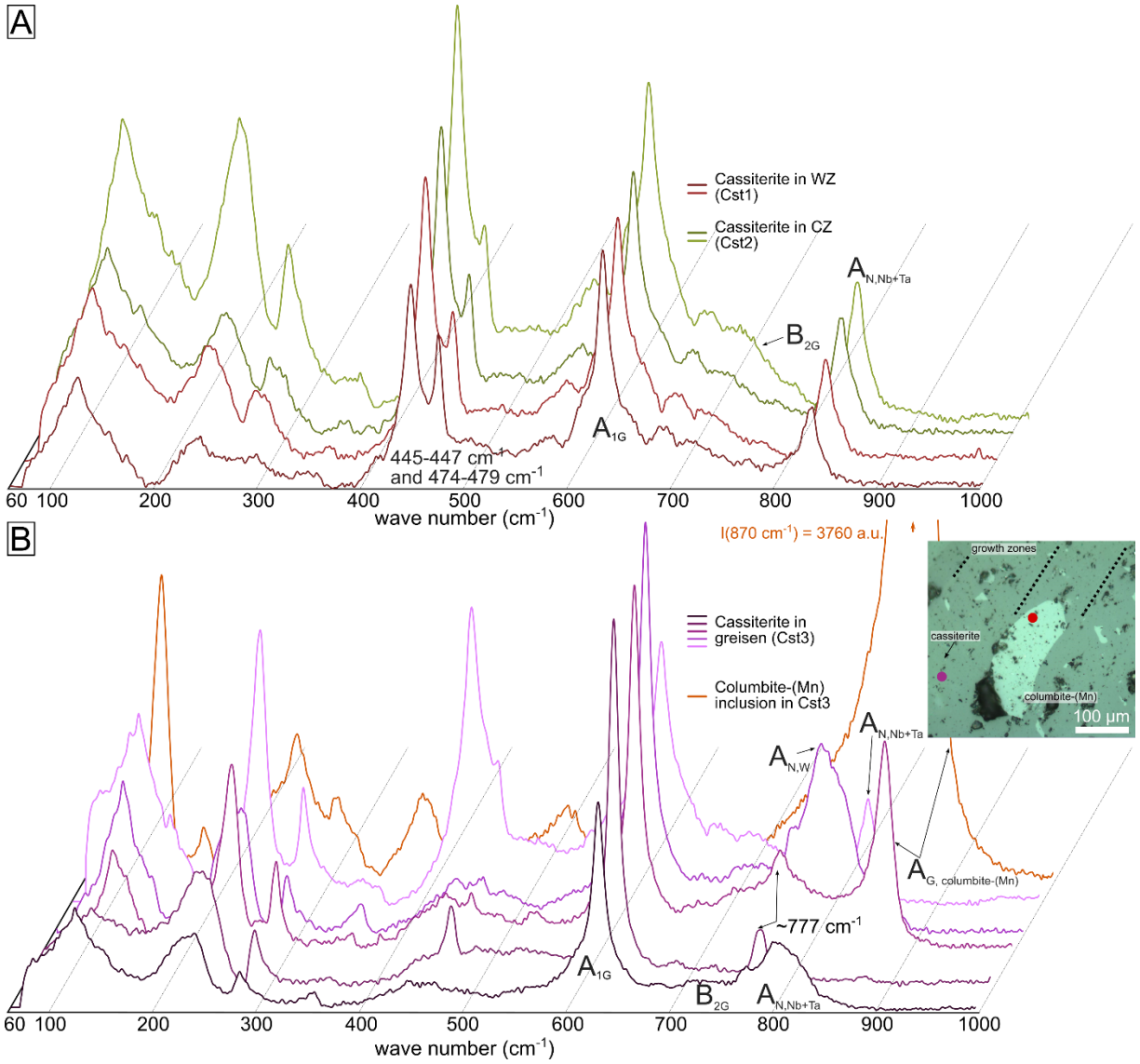

Figure 6. Ternary diagrams of compositional variability (A) in halogen-site occupancy (in atoms per atomic formula unit, apfu) in blue apatite from the core zone compared with igneous apatite in granitic pegmatites from Piccoli and Candela (2002), (B) in W-(Fe,Mn)-(Nb,Ta) coupled substitutions for the three generations of cassiterite (in at.%) and (C) in Ti-(Fe,Mn)-(Nb,Ta) coupled substitutions for the three generations of cassiterite (in at.%). Tie lines from Bennett et al. (2019). Both optically transparent and optically opaque zones in the three cassiterite generations have been analyses.

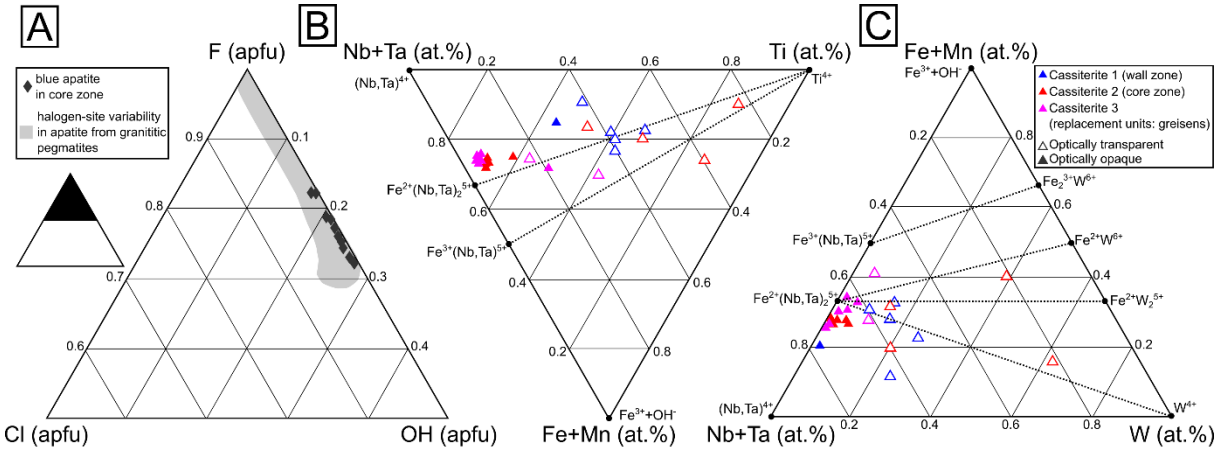

blue apatite *cassiterite*

Figure 7. Microthermometric results. (A) and (B), phase diagrams of the H_2O-NaCl-KCl system according to Sterner et al. (1988) and of the H_2O-NaCl-LiCl system according to Dubois et al. (2010), respectively, reporting the microthermometric data of the L1-, L2- and L3-type fluid inclusions. (C) to (F) Stripplots, which include, boxplots of first melting, hydrohalite melting, ice melting and total homogenisation temperatures of the L1-, L2- and L3-type fluid inclusions.

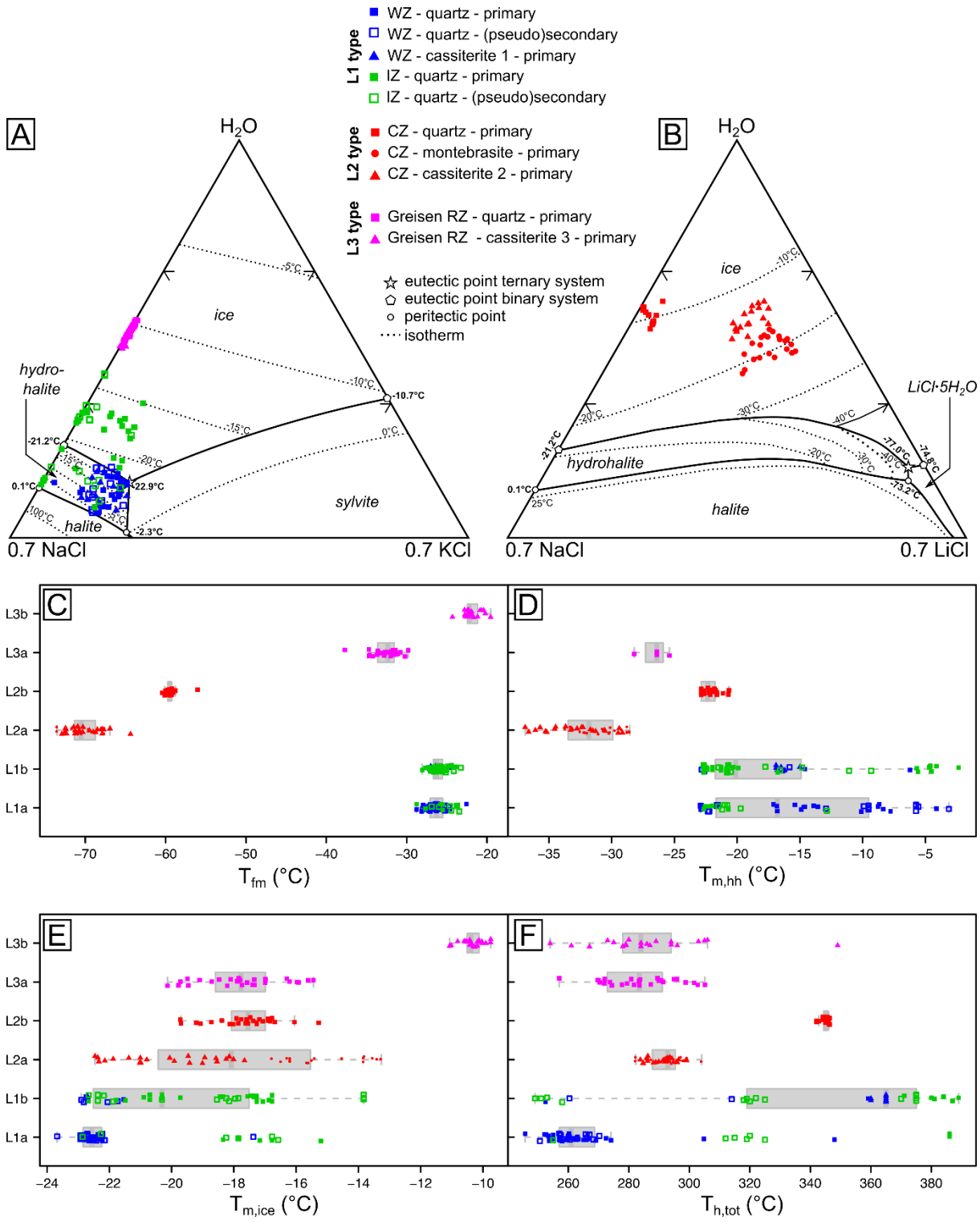
L1 type
WZ - quartz - primary
WZ - quartz - (pseudo)secondary
WZ - cassiterite 1 - primary
IZ - quartz - primary
IZ - quartz - (pseudo)secondary
L2 type
CZ - quartz - primary
CZ - montebrasite - primary
CZ - cassiterite 2 - primary
L3 type
Greisen RZ - quartz - primary
Greisen RZ - cassiterite 3 - primary
eutectic point ternary system
eutectic point binary system
peritectic point
isotherm
A
H2O
ice
hydro-halite
sylvite
halite
-21.2°C
-10.7°C
-22.9°C
-2.3°C
0.1°C
0.7 NaCl
0.7 KCl
B
H2O
ice
hydrohalite
halite
LiCl·5H2O
-21.2°C
0.1°C
25°C
0.7 NaCl
0.7 LiCl
C
L3b
L3a
L2b
L2a
L1b
L1a
Tfm (°C)
D
Tm,hh (°C)
E
Tm,ice (°C)
F
Th,tot (°C)

1149

Figure 8. Representative microphotographs showing the fluid inclusion petrography. All micrographs are taken at 20 °C unless stated otherwise. (A) Primary L1a-subtype inclusion in quartz from the wall zone (1702-3-H-B-12) with accidentally trapped rhodochrosite and paragonite minerals. (B) Complete solidification of the same inclusion as in Figure A at -170 °C and the distinct formation of ice and hydrohalite. (C) Transmitted light microphotograph of cassiterite phase Cst1 in the wall zone with the formation of colour zoning and primary L1b-subtype fluid inclusions along these growth zones. (D) Close-up of one of the L1b-subtype inclusion of Figure C (1037-2-Cst-3). (E) Three primary L1b-subtype inclusions in quartz from the intermediate zone (1449-2-1-D-3/4/5). (F) L2a sub-type inclusions in montebrasite from the core zone with a rare accidentally trapped Li-mica mineral (1440-1-2-A-2-1). (G) L2a sub-type inclusions in cassiterite phase Cst2 in the core zone (1440-1-1-Cast1). (H) Primary fluid inclusion assemblage of L2b-subtype inclusions in quartz from the core zone. (I) Close-up of one of the L2b-subtype inclusion of Figure H (1440-2-2-2-1). (J) Fluid inclusion assemblage of L3a-subtype inclusions in quartz from the greisen replacement zone. (K) Transmitted light microphotograph of cassiterite phase Cst3 in the greisen replacement zone with the presence of primary L3b-subtype fluid inclusions and opaque Mn-columbite mineral inclusions along the growth zones with colour variations. (L) Close-up of one of the L3b-subtype inclusion of Figure H (1023-gr-3-6). The hazy image is caused by cassiterite birefringence.

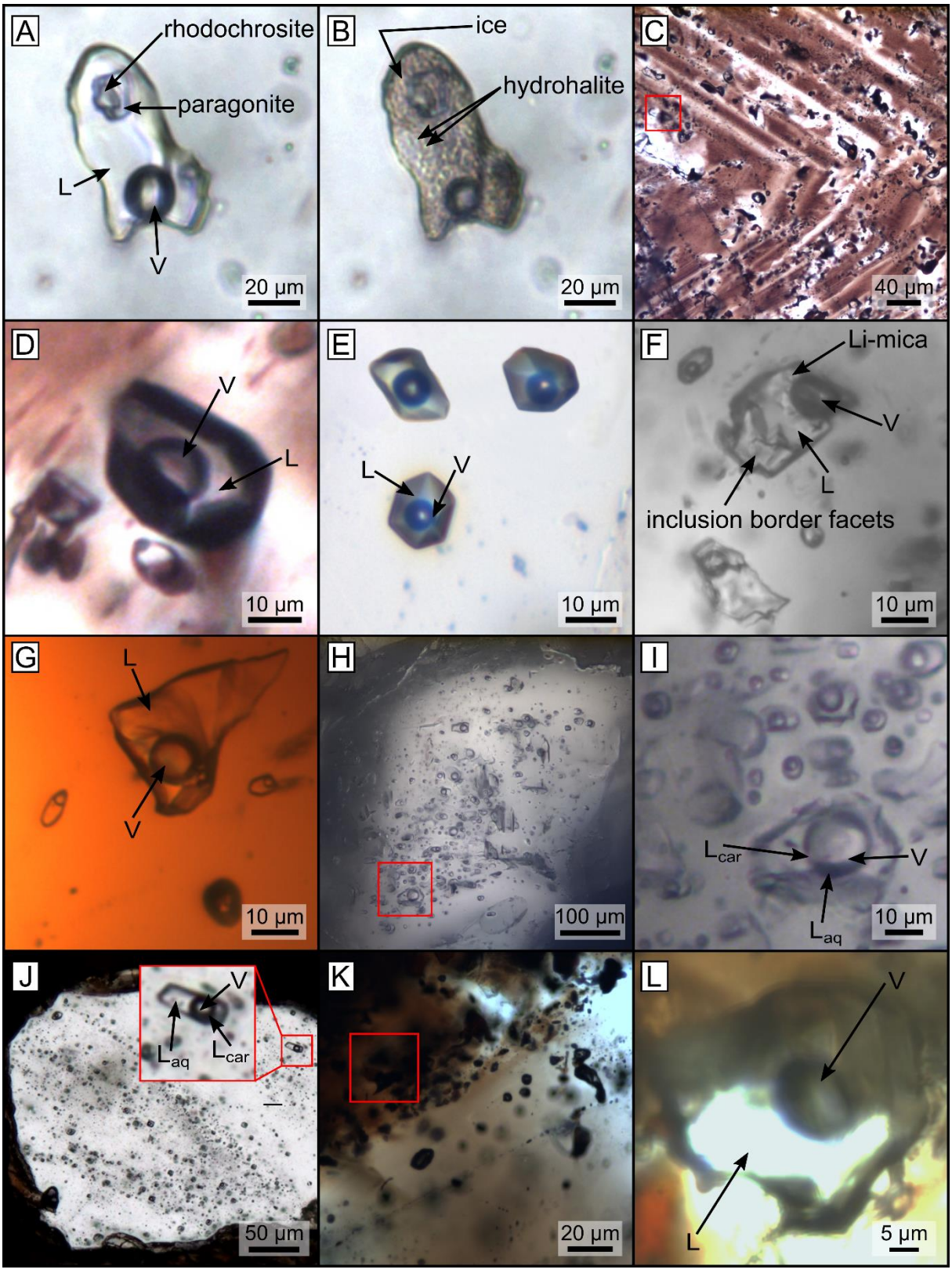
A
rhodochrosite
paragonite
L
V
20 μm
B
ice
hydrohalite
20 μm
C
40 μm
D
V
L
10 μm
E
L
V
10 μm
F
Li-mica
V
L
inclusion border facets
10 μm
G
L
V
10 μm
H
100 μm
I
L_{car}
V
L_{aq}
10 μm
J
V
L_{aq}
L_{car}
50 μm
K
20 μm
L
V
L
5 μm

1169

Figure 9. Calculated isochores for the L1b fluids with an H_2O-NaCl-KCl composition in quartz (n=31) in the wall and intermediate zones. Crystallisation conditions for the GDS have been constrained by correlating the isochores with solidi of volatile-rich (H_2O, Li, B, P) leucogranitic melts (Pichavant, 1984; Pichavant et al., 1987) and regional metamorphic temperatures of the country rocks near the GDS based on garnet-biotite geothermometry (Van Daele et al., 2018). The stability fields of the lithium aluminosilicates and the reported range of crystallisation conditions of rare-element (RE) pegmatites from London (2008) have been added to the plot. The temperature and pressure range of crystallisation of the GDS is between 535-560 °C and 5.1-5.6 kbar.

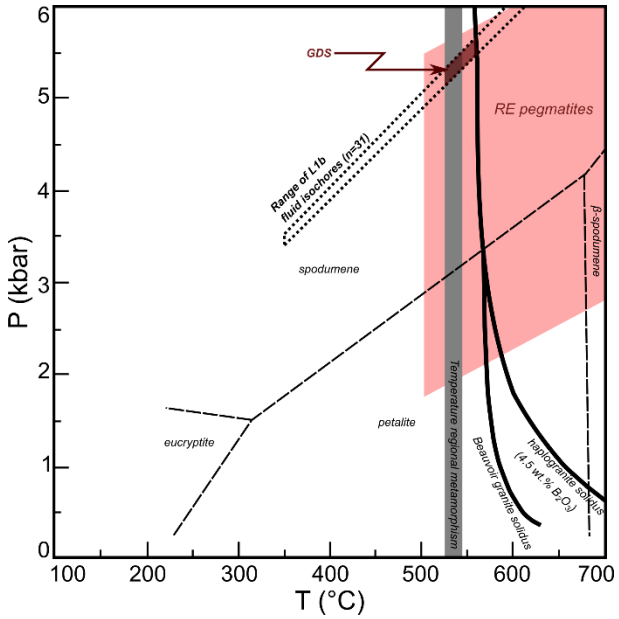

Figure 10. Representative LA-ICP-MS spectra of ablations in the three different host minerals. Ablation of (A) a pseudosecondary L1b-subtype inclusion in quartz from the wall zone (1702-3-I2-B-4), (B) a primary L2a-subtype inclusion in montebrasite from the core zone (1440-1-2-A-2-3) and (C) a primary L2a-subtype inclusion in cassiterite from the core zone, i.e. Cst2 (1440-1-1-Cast1). The grey bar indicates the opening of the inclusion.

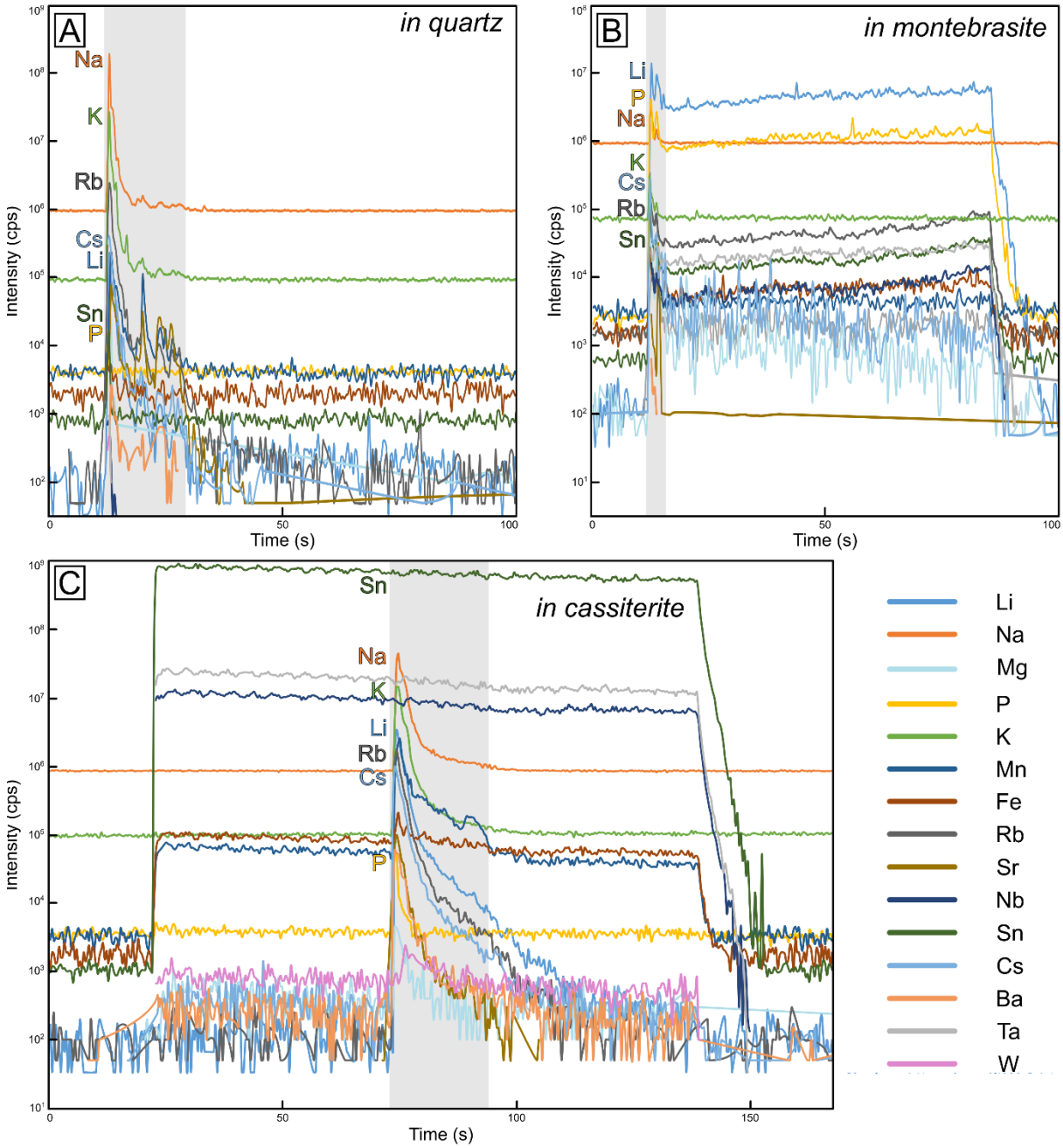

Figure 11. Stripplots, including boxplots, of the elemental concentrations (in ppm) in the fluid phase based on LA-ICP-MS microanalyses of all fluid inclusion types and parageneses. (A) Li, (B) Na, (C) K, (D) Rb, (E) Cs, (F) Li Cs^{-1}, (G) K Rb^{-1}, (H) K Cs^{-1}, (I) Mg, (J) Ba, (K) Sr, (L) Fe, (M) Mn, (N) P, (O) Nb, (P) Sn, (Q), Ta and (R) W.

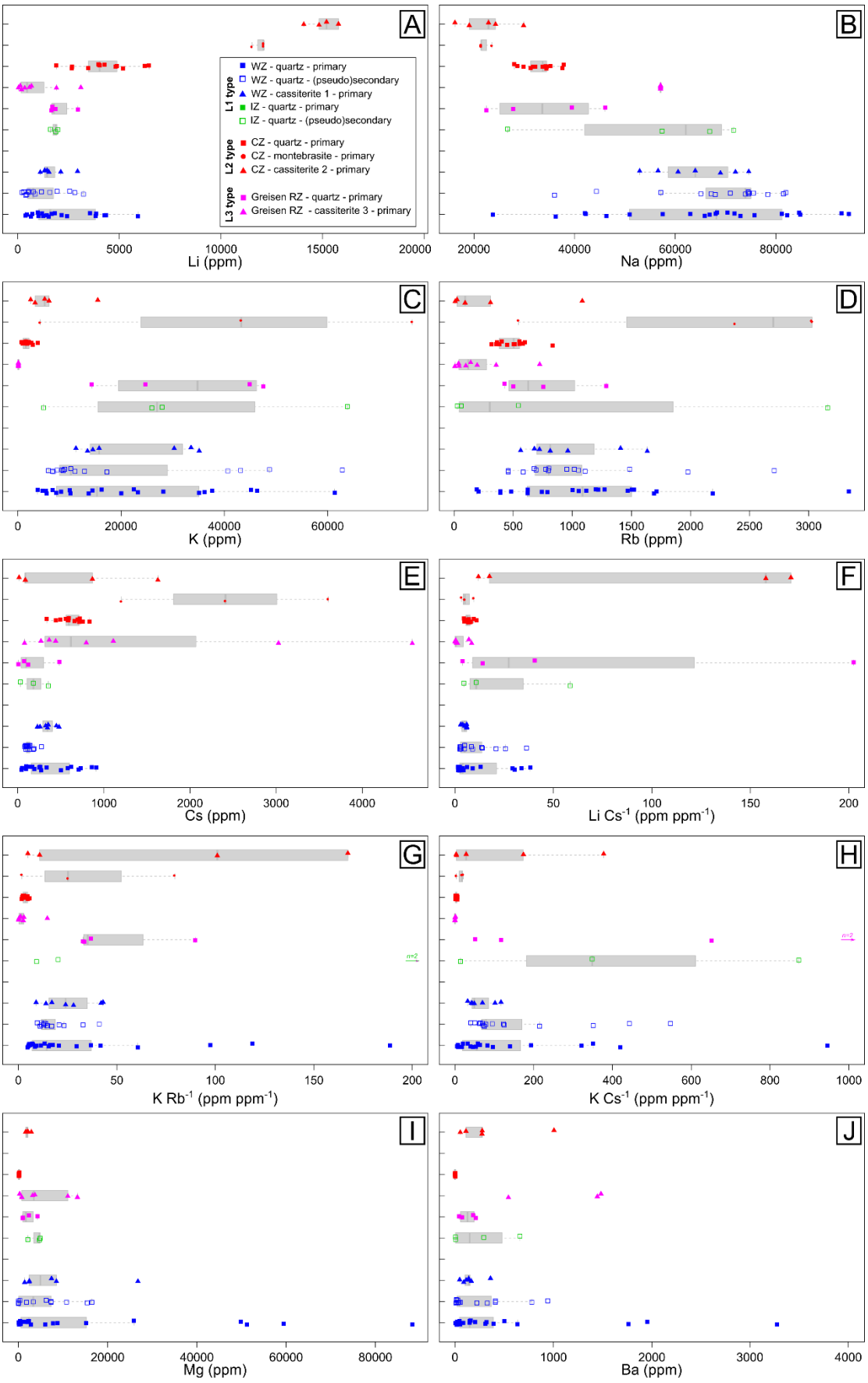
A
B
C
D
E
F
G
H
I
J
L1 type
WZ - quartz - primary
WZ - quartz - (pseudo)secondary
WZ - cassiterite 1 - primary
IZ - quartz - primary
IZ - quartz - (pseudo)secondary
L2 type
CZ - quartz - primary
CZ - montebrasite - primary
CZ - cassiterite 2 - primary
L3 type
Greisen RZ - quartz - primary
Greisen RZ - cassiterite 3 - primary
Li (ppm)
Na (ppm)
K (ppm)
Rb (ppm)
Cs (ppm)
Li Cs-1 (ppm ppm-1)
K Rb-1 (ppm ppm-1)
K Cs-1 (ppm ppm-1)
Mg (ppm)
Ba (ppm)

1190

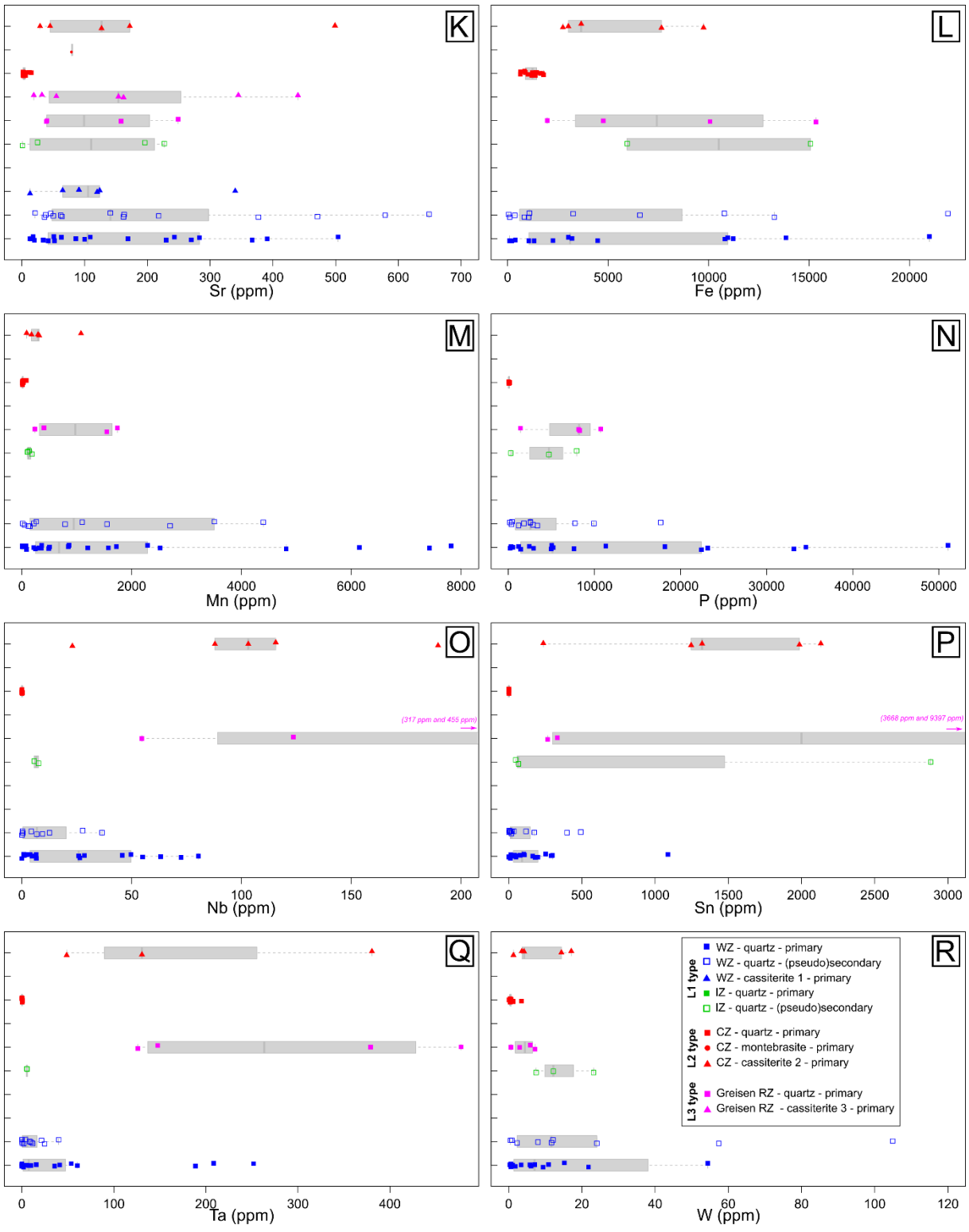
K
Sr (ppm)
L
Fe (ppm)
M
Mn (ppm)
N
P (ppm)
O
(317 ppm and 455 ppm)
Nb (ppm)
P
(3668 ppm and 9397 ppm)
Sn (ppm)
Q
Ta (ppm)
R
W (ppm)
L1 type
WZ - quartz - primary
WZ - quartz - (pseudo)secondary
WZ - cassiterite 1 - primary
IZ - quartz - primary
IZ - quartz - (pseudo)secondary
L2 type
CZ - quartz - primary
CZ - montebrasite - primary
CZ - cassiterite 2 - primary
L3 type
Greisen RZ - quartz - primary
Greisen RZ - cassiterite 3 - primary

1191

Figure 12. Scatter plots of relationships between specific sets of elements in the fluid phase based on LA-ICP-MS microanalyses of all fluid inclusion types and parageneses. (A) to (F) shows the concentration (in ppm) of Li, Na, K, Rb, Cs and Sn, respectively, as a function of the molality of Cl (mol kg^{-1}) in the fluid phase, as derived from microthermometric data. (G) and (H) show log-log plots of the concentration (in ppm) of Sn and Nb+Ta as a function of the P concentration (ppm). (I) Plot showing the molar concentration (mmol kg^{-1}) of Na versus K. The reaction vectors involving microcline albitisation and feldspar muscovitisation are also provided.

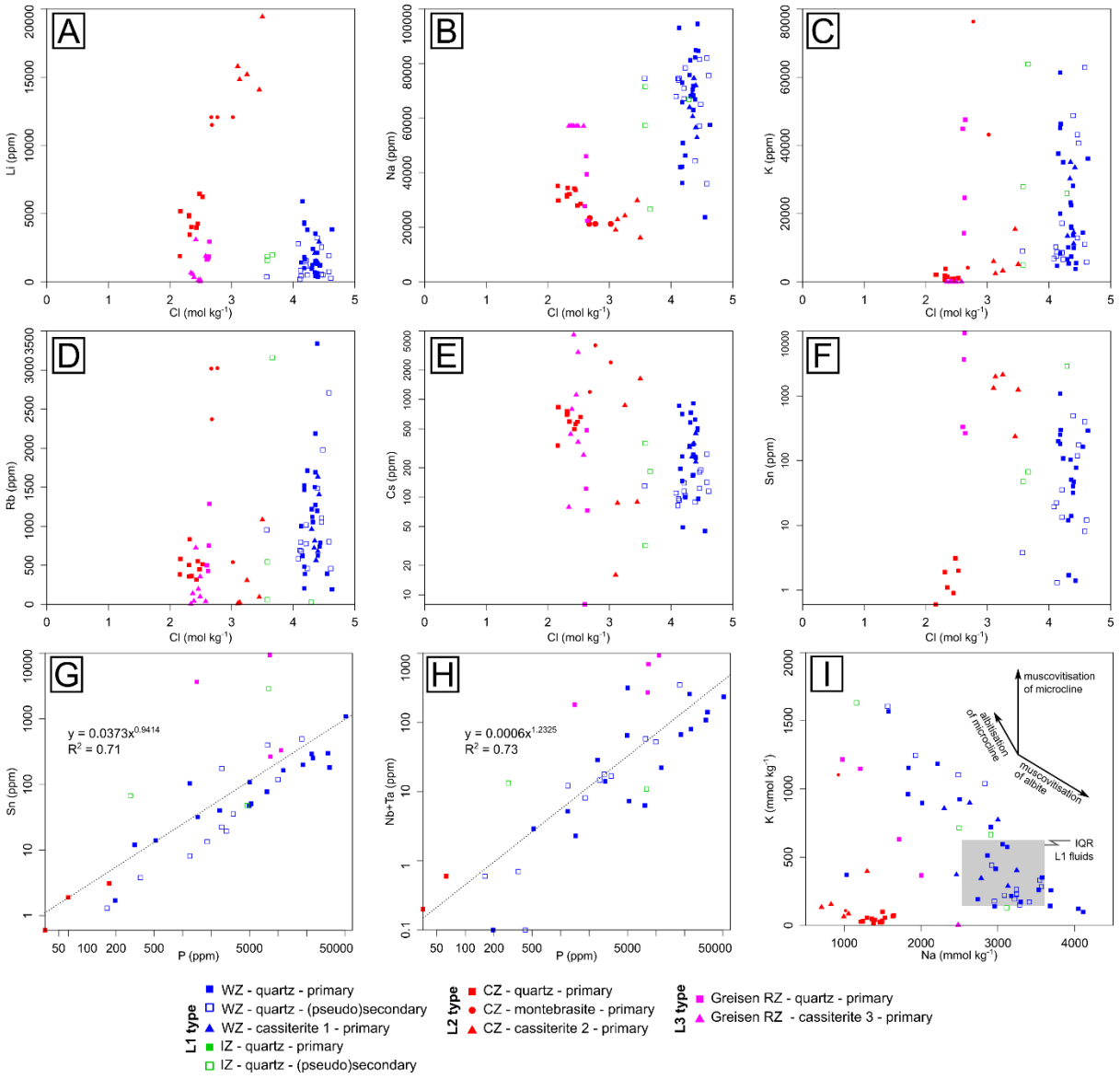

Figure 13. Scatter plot showing the Sn concentration (in mol kg^{-1}) as a function of the molality of Cl (mol kg^{-1}) in the fluid phase. The plot permits comparison of Sn concentration in the fluid inclusions of the GDS with experimental Sn solubilities from Kovalenko et al. (1986), Wilson and Eugster (1990) and Duc-Tin et al. (2007). The experimental Sn solubilites are for HCl- and NaCl-bearing fluids buffered near NNO (nickel-nickel oxide).

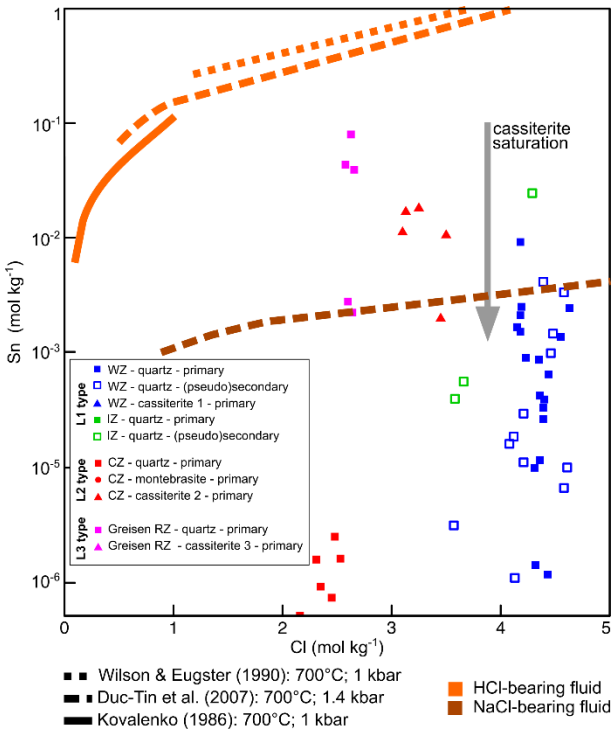

References

Ackerman, L., Zachariáš, J., Pudilová, M., 2006. P–T and fluid evolution of barren and lithium pegmatites from Vlastějovice, Bohemian Massif, Czech Republic. International Journal of Earth Sciences 96, 623-638.

Allan, M.M., Yardley, B.W.D., Forbes, L.J., Shmulovich, K.I., Banks, D.A., Shepherd, T.J., 2005. Validation of LA-ICP-MS fluid inclusion analysis with synthetic fluid inclusions. American Mineralogist 90, 1767-1775.

Anderko, A., Pitzer, K.S., 1993. Phase Equilibria and Volumetric Properties of the System NaCl-H2O above 573 K - Equation of State Representation. Geochimica et Cosmochimica Acta 57, 4885-4897.

Anthony, J. W., Bideaux, R.A., Bladh, K.W., Nichols M. C, 2000, Handbook of Mineralogy. IV. Arsenates, Phosphates, Vanadates. Mineral Data Publishing, 689 pp.

Audétat, A., Gunther, D., Heinrich, C.A., 2000. Causes for large-scale metal zonation around mineralized plutons: Fluid inclusion LA-ICP-MS evidence from the Mole Granite, Australia. Economic Geology and the Bulletin of the Society of Economic Geologists 95, 1563-1581.

Bakker, R.J., 1997. Clathrates: Computer programs to calculate fluid inclusion V-X properties using clathrate melting temperatures. Computers & Geosciences 23, 1-18.

Bakker, R.J., 2003. Package FLUIDS 1. Computer programs for analysis of fluid inclusion data and for modelling bulk fluid properties. Chemical Geology 194, 3-23.

Bennett, J.M., Kemp, A.I.S., Hagemann, S.G., Fiorentini, M.L., Roberts, M.P., 2019. Cassiterite as a record of Sn mineral system processes, Proceedings of the 15th SGA Biennial Meeting, Glasgow, Scotland, pp. 134-137.

Bhalla, P., Holtz, F., Linnen, R.L., Behrens, H., 2005. Solubility of cassiterite in evolved granitic melts: effect of T, fO2, and additional volatiles. Lithos 80, 387-400.

Bodnar, R.J., Sterner, S.M., Hall, D.L., 1989. SALTY: a FORTRAN program to calculate compositions of fluid inclusions in the system NaCl-KCl-H2O. Computers & Geosciences 15, 19-41.

Černý, P., Ercit, T.S., 2005. The classification of granitic pegmatites. The Canadian Mineralogist 43, 2005-2026.

Cigala, R.M., Crea, F., De Stefano, C., Lando, G., Milea, D., Sammartano, S., 2012. The inorganic speciation of tin(II) in aqueous solution. Geochimica et Cosmochimica Acta 87, 1-20.

Dewaele, S., Henjes-Kunst, F., Melcher, F., Sitnikova, M., Burgess, R., Gerdes, A., Fernandez, M.A., Clercq, F.D., Muchez, P., Lehmann, B., 2011. Late Neoproterozoic overprinting of the cassiterite and columbite-tantalite bearing pegmatites of the Gatumba area, Rwanda (Central Africa). Journal of African Earth Sciences 61, 10-26.

Dewaele, S., De Clercq, F., Hulsbosch, N., Piessens, K., Boyce, A., Burgess, R., Muchez, P., 2016. Genesis of the vein-type tungsten mineralization at Nyakabingo (Rwanda) in the Karagwe–Ankole belt, Central Africa. Mineralium Deposita 51, 283-307.

Diamond, L.W., 2001. Review of the systematics of CO2-H2O fluid inclusions. Lithos 55, 69-99.

Dubois, M., Monnin, C., Castelain, T., Coquinot, Y., Gouy, S., Gauthier, A., Goffe, B., 2010. Investigation of the H2O-NaCl-LiCl System: A Synthetic Fluid Inclusion Study and Thermodynamic Modeling from-50 degrees to+100 degrees C and up to 12 mol/kg. Economic Geology 105, 329-338.

Duc-Tin, Q., Audétat, A., Keppler, H., 2007. Solubility of tin in (Cl, F)-bearing aqueous fluids at 700°C, 140MPa: A LA-ICP-MS study on synthetic fluid inclusions. Geochimica et Cosmochimica Acta 71, 3323-3335.

Fiege, A., Simon, A., Linsler, S.A., Bartels, A., Linnen, R.L., 2018. Experimental constraints on the effect of phosphorous and boron on Nb and Ta ore formation. Ore Geology Reviews 94, 383-395.

Fransolet, A.M., Abraham, K., 1983. Une association triplite-montebrasite-griphite dans la pegmatite de Buranga, Rwanda. Annales de la Société Géologique de Belgique 106, 299-309.

Guillong, M., L., M.D., Allan, M.M., Heinrich, C.A., Yardley, B.W.D., 2008. Appendix A6: SILLS: A MATLAB-based program for the reduction of laser ablation ICP-MS data of homogeneous materials and inclusions, in: Sylvester, P. (Ed.), Laser Ablation ICP-MS in the Earth Sciences: Current Practices and Outstanding Issues. Mineralogical Association of Canada, Short Course, Vancouver, B. C.

Heinrich, C.A., 1990. The chemistry of hydrothermal tin(-tungsten) ore deposition. Economic Geology 85, 457-481.

Holtz, F., Johannes, W., Tamic, N., Behrens, H., 2001. Maximum and minimum water contents of granitic melts generated in the crust: a reevaluation and implications. Lithos 56, 1-14.

Hughes, J.M., Ertl, A., Bernhardt, H.J., Rossman, G.R., Rakovan, J., 2004. Mn-rich fluorapatite from Austria: Crystal structure, chemical analysis, and spectroscopic investigations. American Mineralogist 89, 629-632.

Hulsbosch, N., Hertogen, J., Dewaele, S., André, L., Muchez, P., 2014. Alkali metal and rare earth element evolution of rock-forming minerals from the Gatumba area pegmatites (Rwanda): Quantitative assessment of crystal-melt fractionation in the regional zonation of pegmatite groups. Geochimica et Cosmochimica Acta 132, 349-374.

Hulsbosch, N., 2016. Chemical fractionation in granite-related ore systems: evidence from Nb-Ta-Sn pegmatite-type and Sn-W quartz vein-type mineralisation in the Karagwe-Ankole Belt (Rwanda) Department of earth and environmental sciences - geology division. University of Leuven - KU Leuven, Leuven, p. 218.

Hulsbosch, N., 2019. Nb-Ta-Sn-W distribution in granite-related ore systems: fractionation mechanisms and examples from the Karagwe-Ankole Belt of Central Africa, in: Decrée, S., Robb, L. (Eds.), Ore Deposits Origin Exploration and Exploitation. Wiley, pp. 75-107.

Hulsbosch, N., Boiron, M.-C., Dewaele, S., Muchez, P., 2016. Fluid fractionation of tungsten during granite–pegmatite differentiation and the metal source of peribatholitic W quartz veins: Evidence from the Karagwe-Ankole Belt (Rwanda). Geochimica et Cosmochimica Acta 175, 299-318.

Hulsbosch, N., Van Daele, J., Reinders, N., Dewaele, S., Jacques, D., Muchez, P., 2017. Structural control on the emplacement of contemporaneous Sn-Ta-Nb mineralized LCT pegmatites and Sn bearing quartz veins: Insights from the Musha and Ntunga deposits of the Karagwe-Ankole Belt, Rwanda. Journal of African Earth Sciences 134, 24-32.

Hulsbosch, N., Boiron, M.-C., Dewaele, S., Muchez, P., 2016. Fluid fractionation of tungsten during granite–pegmatite differentiation and the metal source of peribatholitic W quartz veins: Evidence from the Karagwe-Ankole Belt (Rwanda). Geochimica et Cosmochimica Acta 175, 299-318.

Hulsbosch, N., Boiron, M.-C., Thomas, R., Van Daele, J., Dewaele, S., Muchez, P., 2019. Evaluation of the petrogenetic significance of melt inclusions in pegmatitic schorl-dravite from graphic tourmaline-quartz assemblages: Application of LA-ICP-QMS analyses and volume ratio calculations. Geochimica et Cosmochimica Acta 244, 308-335.

Iveson, A.A., Webster, J.D., Rowe, M.C., Neill, O.K., 2019. Fluid-melt trace-element partitioning behaviour between evolved melts and aqueous fluids: Experimental constraints on the magmatic-hydrothermal transport of metals. Chemical Geology 516, 18-41.

Jahns, R.H., Burnham, C.W., 1969. Experimental studies of pegmatite genesis; I, A model for the derivation and crystallization of granitic pegmatites. Economic Geology 64, 843-864.

1305 Keppler, H., 1994. Partitioning of phosphorus between melt and fluid in the system
1306 haplogranite-H2O-P2O5. Chemical Geology 117, 345-353.
1307 Kontak, D.J., 2006. Nature and origin of an LCT-type pegmatite with late-stage sodium
1308 enrichment, Yarmouth County, Nova Scotia: I. Geological setting and petrology. The
1309 Canadian Mineralogist 44, 563-598.
1310 Kontak, D.J., Ansdell, K., Dostal, J., Halter, W., Martin, R., Williams-Jones, A.E., 2001. The
1311 nature and origin of pegmatites in a fluorine-rich leucogranite, East Kemptville Tin Deposit,
1312 Nova Scotia, Canada. Transactions of the Royal Society of Edinburgh-Earth Sciences 92,
1313 173-200.
1314 Korges, M., Weis, P., Lueders, V., Laurent, O., 2018. Depressurization and boiling of a single
1315 magmatic fluid as a mechanism for tin-tungsten deposit formation. Geology 46, 75-78.
1316 Kovalenko, N.I., Ryzhenko, B., Barsukov, V.L., Klintsova, A.P., Velyukhanova, T.K., Volynets,
1317 M.P., Kitayeva, L.P., 1986. The solubility of cassiterite in HCl and HCl + NaCl (KCl)
1318 solutions at 500°C and 1000 atm under fixed redox conditions. Geochemistry International
1319 23, 1-16.
1320 Lehmann, B., 1990. Magmatic Enrichment of Tin, Metallogeny of tin. Springer, Berlin-
1321 Heidelberg-New York, pp. 45-85.
1322 Lehmann, B., Halder, S., Ruzindana Munana, J., de la Paix Ngizimana, J., Biryabarema, M.,
1323 2014. The geochemical signature of rare-metal pegmatites in Central Africa: Magmatic
1324 rocks in the Gatumba tin–tantalum mining district, Rwanda. Journal of Geochemical
1325 Exploration 144, Part C, 528-538.
1326 Linnen, R.L., Williams-Jones, A.E., Martin, R.F., 1992. Evidence of magmatic cassiterite
1327 mineralization at the Nong Sua aplite-pegmatite complex, Thailand. The Canadian
1328 Mineralogist 30, 739-761.

1329 Linnen, R.L., Pichavant, M., Holtz, F., 1996. The combined effects of f(O2) and melt
1330 composition on SnO2 solubility and tin diffusivity in haplogranitic melts. Geochimica et
1331 Cosmochimica Acta 60, 4965-4976.
1332 Linnen, R.L., Samson, I.M., Williams-Jones, A.E., Chakhmouradian, A.R., 2014. Geochemistry
1333 of the Rare-Earth Element, Nb, Ta, Hf, and Zr Deposits. 543-568.
1334 London, D., 1987. Internal differentiation of rare-element pegmatites: Effects of boron,
1335 phosphorus, and fluorine. Geochimica et Cosmochimica Acta 51, 403-420.
1336 London, D., 2008. Pegmatites. Mineralogical Association of Canada. 347 pp.
1337 London, D., 2014. A petrologic assessment of internal zonation in granitic pegmatites. Lithos
1338 184–187, 74-104.
1339 London, D., 2018. Ore-forming processes within granitic pegmatites. Ore Geology Reviews
1340 101, 349-383.
1341 London, D., Morgan, G.B., 2017. Experimental Crystallization of the Macusani Obsidian, with
1342 Applications to Lithium-rich Granitic Pegmatites. Journal of Petrology 58, 1005-1030.
1343 London, D., Vi, G.B.M., Wolf, M.B., 2001. Amblygonite-montebrasite solid solutions as
1344 monitors of fluorine in evolved granitic and pegmatitic melts. American Mineralogist 86,
1345 225-233.
1346 Longerich, H.P., Jackson, S.E., Günther, D., 1996. Laser ablation inductively coupled plasma
1347 mass spectrometric transient signal data acquisition and analyte concentration calculation
1348 Journal of Analytical Atomic Spectrometry 11, 899-904.
1349 Maneta, V., Anderson, A.J., 2018. Monitoring the crystallization of water-saturated granitic
1350 melts in real time using the hydrothermal diamond anvil cell. Contributions to Mineralogy
1351 and Petrology 173, 83.
1352 Melcher, F., Graupner, T., Gäbler, H.-E., Sitnikova, M., Henjes-Kunst, F., Oberthür, T.,
1353 Gerdes, A., Dewaele, S., 2015. Tantalum–(niobium–tin) mineralisation in African

1354 pegmatites and rare metal granites: Constraints from Ta–Nb oxide mineralogy,
1355 geochemistry and U–Pb geochronology. Ore Geology Reviews 64, 667-719.
1356 Migdisov, A.A., Williams-Jones, A.E., 2005. An experimental study of cassiterite solubility in
1357 HCl-bearing water vapour at temperatures up to 350 °C. Implications for tin ore formation.
1358 Chemical Geology 217, 29-40.
1359 Nabelek, P.I., Whittington, A.G., Sirbescu, M.-L.C., 2009. The role of H2O in rapid
1360 emplacement and crystallization of granite pegmatites: resolving the paradox of large
1361 crystals in highly undercooled melts. Contributions to Mineralogy and Petrology 160, 313-
1362 325.
1363 Piccoli, P., Candela, P., 2002. Apatite in Igneous Systems, in: Kohn, M.J., Rakovan, J.,
1364 Hughes, J.M. (Eds.), Phosphates: geochemical, geobiological and materials importance.
1365 Mineralogical Society of America, Washington DC, pp. 255-292.
1366 Pichavant, M., 1984. The effect of boron on liquidus phase relationships in the system Qz–Ab–
1367 Or–H2O at 1 kbar. Eos Transactions American Geophysical Union 65, 298.
1368 Pichavant, M., Boher, M., Stenger, J.F., Aissa, M., Charoy, B., 1987. Relations de phase des
1369 granites de Beauvoir à 1 et 3 kbar en conditions de saturation en H2O. Géologie de la
1370 France 2-3, 77-86.
1371 Pohl, W.L., Biryabarema, M., Lehmann, B., 2013. Early Neoproterozoic rare metal (Sn, Ta, W)
1372 and gold metallogeny of the Central Africa Region: a review. Applied Earth Science 122,
1373 66-82.
1374 Rondeau, B., Fritsch, E., LeFevre, P., Guiraud, M., Fransolet, A.M., Lulzac, Y., 2006. A
1375 Raman investigation of the amblygonite-montebrasite series. Canadian Mineralogist 44,
1376 1109-1117.
1377 Schmidt, C., 2018. Formation of hydrothermal tin deposits: Raman spectroscopic evidence for
1378 an important role of aqueous Sn(IV) species. Geochimica et Cosmochimica Acta 220,
1379 499-511.

1380 Shearer, C.K., Papike, J.J., 1988. Pegmatite-wallrock interaction; holmquistite-bearing
1381 amphibolite, Edison Pegmatite, Black Hills, South Dakota. American Mineralogist 73, 324-
1382 337.
1383 Siegel, K., Wagner, T., Trumbull, R.B., Jonsson, E., Matalin, G., Wälle, M., Heinrich, C.A.,
1384 2016. Stable isotope (B, H, O) and mineral-chemistry constraints on the magmatic to
1385 hydrothermal evolution of the Varuträsk rare-element pegmatite (Northern Sweden).
1386 Chemical Geology 421, 1-16.
1387 Sirbescu MLC, Zielinski NJ, Wilke M, Schmidt C, 2016. What does it take to make a
1388 pegmatite? Direct observations of crystal nucleation and growth. Second Eugene E Foord
1389 pegmatite symposium, July 15–19, Golden, Colorado, pp 104–106.
1390 Sirbescu, M.L.C., Schmidt, C., Veksler, I.V., Whittington, A.G., Wilke, M., 2017. Experimental
1391 Crystallization of Undercooled Felsic Liquids: Generation of Pegmatitic Texture. Journal of
1392 Petrology 58, 539-568.
1393 Štemprok, M., 1990. Solubility of tin, tungsten and molybdenum oxides in felsic magmas.
1394 Mineralium Deposita 25, 205-212.
1395 Sterner, S.M., Hall, D.L., Bodnar, R.J., 1988. Synthetic fluid inclusions. V. Solubility relations in
1396 the system NaCl-KCl-H20 under vapor-saturated conditions*. Geochimica et
1397 Cosmochimica Acta 52, 989-1005.
1398 Tack, L., Wingate, M.T.D., De Waele, B., Meert, J., Belousova, E., Griffin, B., Tahon, A.,
1399 Fernandez-Alonso, M., 2010. The 1375 Ma “Kibaran event” in Central Africa: Prominent
1400 emplacement of bimodal magmatism under extensional regime. Precambrian Research
1401 180, 63-84.
1402 Tacker, R.C., 2008. Carbonate in igneous and metamorphic fluorapatite: Two type A and two
1403 type B substitutions. American Mineralogist 93, 168-176.

Ternane, R., Cohen-Adad, M.T., Panczer, G., Goutaurdier, N., Kbir-Ariguib, N., Trabelsi-Ayedi, M., Florian, P., Massiot, D., 2003. Introduction of boron in hydroxyapatite: synthesis and structural characterization. Journal of Alloys and Compounds 333, 62-71.

Thomas, R., Webster, J.D., 2000. Strong tin enrichment in a pegmatite-forming melt. Mineralium Deposita 35, 570-582.

Van Daele, J., Hulsbosch, N., Mondelaers, A., Dewaele, S., Muchez, P., 2018. Pressure-temperature evolution in the Western Domain of the Karagwe-Ankole Belt, Central-Africa, during the Mesoproterozoic, GB2018 6th International Geologica Belgica Meeting 2018, Leuven, Belgium.

Varlamoff, N., 1972. Central and West African Rare-Metal Granitic Pegmatites,. Related Aplites, Quartz Veins and Mineral Deposits. Mineralium Deposita 7, 202-216.

Veksler, I.V., Thomas, R., Schmidt, C., 2002. Experimental evidence of three coexisting immiscible fluids in synthetic granitic pegmatite. American Mineralogist 87, 775-779.

Wang, R., Wu, J., Dubessy, J., Monchoux, P., 1993. Raman spectroscopy of Nb, Ta-Rich cassiterite in Beauvoir and Montebras granites, France. Chinese Journal of Geochemistry 12, 353-390.

Webster, J.D., Thomas, R., Rhede, D., Forster, H.J., Seltmann, R., 1997. Melt inclusions in quartz from an evolved peraluminous pegmatite: Geochemical evidence for strong tin enrichment in fluorine-rich and phosphorus-rich residual liquids. Geochimica et Cosmochimica Acta 61, 2589-2604.

Wille, G., Lerouge, C., Schmidt, U., 2018. A multimodal microcharacterisation of trace-element zonation and crystallographic orientation in natural cassiterite by combining cathodoluminescence, EBSD, EPMA and contribution of confocal Raman-in-SEM imaging. Journal of Microscopy 270, 309-317.

1429 Williams, T.J., Candela, P.A., Piccoli, P.M., 1997. Hydrogen-alkali exchange between silicate
1430 melts and two-phase aqueous mixtures: an experimental investigation. Contributions to
1431 Mineralogy and Petrology 128, 114-126.
1432 Wilson, G.A., Eugster, H.P., 1990. Cassiterite solubility and tin speciation in supercritical
1433 chloride solutions, in: Spencer, R.J., Chou, I.M. (Eds.), Geochemical Society Special
1434 Publication, pp. 179-195.
1435 Yardley, B., Bodnar, R.J., 2014. Fluids in the Continental Crust. Geochemical Perspectives 3,
1436 1-127.
1437 Zajacz, Z., Halter, W.E., Pettke, T., Guillong, M., 2008. Determination of fluid/melt partition
1438 coefficients by LA-ICPMS analysis of co-existing fluid and silicate melt inclusions: Controls
1439 on element partitioning. Geochimica et Cosmochimica Acta 72, 2169-2197.

1440